

# Engineering Spasers: Models, Designs, and Applications



**Chanaka Suranjith Rupasinghe**

Department of Electrical and Computer Systems Engineering  
Monash University

A thesis submitted for the degree of Doctor of Philosophy at Monash University  
in 2015

Supervisor: *Professor Malin Premaratne*

Associate supervisor: *Dr. Weiren Zhu*



## Copyright notice

©Chanaka S. Rupasinghe (2015). Except as provided in the Copyright Act 1968, this thesis may not be reproduced in any form without the written permission of the author.

I certify that I have made all reasonable efforts to secure copyright permissions for third-party content included in this thesis and have not knowingly added copyright content to my work without the owner's permission.

## Abstract

The spaser nanolaser, which is the nanoplasmonic counterpart of the laser, enables the generation and amplification of coherent surface plasmons (SPs) by means of stimulated emission. Spaser opens up a new era of devices which overcome the speed barriers of electronics and miniaturizing barriers of optics. This research is mainly focused on engineering spaser devices, particularly the guidelines for design optimization, new designs with improved characteristics, and potential applications. First, a general quantum mechanical model is developed considering the degeneracy of localized SP modes supported by a resonator. Density matrix analysis of this system helps to derive an expression for SP generation rate and identify the tunable parameters for design optimization. The developed model is then applied to optimize a simple spaser design, in which a metal nanosphere is resonantly coupled to a quantum dot, by altering their material and geometrical parameters. Next, alternative spaser materials are considered. Although not commonly used in spaser designs, graphene possesses much better plasmonic properties compared to gold or silver, and carbon nanotubes (CNTs) display excellent photoluminescence properties. Therefore, a new all-carbon spaser design is proposed where a square shaped graphene nanoflake (GNF) resonator powered by a CNT gain element offering the advantages of tunability, robustness, flexibility, and thermal stability. This design also is analyzed employing the general model to determine the different material and geometric parameters of GNF and CNT influencing the spaser operation. Based on these results, clear spaser design guidelines such as identifying the crucial tuning parameters, fabricating the resonator, choosing the appropriate gain medium and pumping mechanism, and relative placement of the components are also sought. Finally, some new applications of spaser nanolasers are proposed and a spaser powered cancer therapy is discussed in detail. In this setup, a large number of tiny nanolasers penetrate tumors to thermally ablate malignant cancer cells. Hence, this research as a whole contributes towards engineering the spaser and catalyzing the process of its practical use and commercialization.

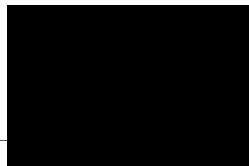
# Declaration

In accordance with Monash University Doctorate Regulation 17.2 Doctor of Philosophy and Research Masters Regulations, the following declarations are made:

I hereby declare that this thesis contains no material which has been accepted for the award of any other degree or diploma at any university or equivalent institution and that, to the best of my knowledge and belief, this thesis contains no material previously published or written by another person, except where due reference is made in the text of the thesis.

The core theme of the thesis is Engineering Spasers: Models, Designs, and Applications. The ideas, development and writing up of all the work in the thesis were the principal responsibility of myself, the candidate, working within the Department of Electrical and Computer Systems Engineering under the supervision of Prof. Malin Premaratne and Dr. Weiren Zhu.

**Signed:**

A solid black rectangular box redacting the signature of the candidate.

Chanaka S. Rupasinghe

**Date:** August 27, 2015

# Related Publications and Patents

## Publications

### Journal papers

[J1] Chanaka Rupasinghe, Ivan D Rukhlenko, and Malin Premaratne. Design optimization of spasers considering the degeneracy of excited plasmon modes. *Optics Express*, 21(13):15335-15349, 2013. (Impact factor-3.525, Rank- 6/83-Q1)

[J2] Chanaka Rupasinghe, Ivan D Rukhlenko, and Malin Premaratne. Spaser made of graphene and carbon nanotubes. *ACS Aano*, 8(3):2431-2438, 2014. (Impact factor-12.033, Rank- 9/148 Q1)

### Conference papers

[C1] Chanaka Rupasinghe, Weiren Zhu, and Malin Premaratne. Spaser powered photothermal cancer therapy using graphene and carbon nanotubes. In *Photonics Conference (IPC), 2014 IEEE*, 16-17. IEEE, 2014.

## Patents

[P1] Chanaka Rupasinghe, Ivan D Rukhlenko, and Malin Premaratne. Carbon based surface plasmon source and applications thereof. *AusPat* 2015200886, 2015 (Pending)

## Acknowledgements

I would like to thank my supervisor Prof. Malin Premaratne for the continuous guidance and encouragement, associate supervisors Dr. Wieren Zhu and Dr. Ivan D. Rukhlenko for their editorial assistance in publications, and colleagues at Advanced Computing and Simulation Laboratory for sharing their views on my work. I am also grateful to the Monash University Institute of Graduate Research, Department of Electrical and Computer Systems Engineering, and the Faculty of Engineering, for providing all the facilities including scholarships, infrastructure, and educational content, required to complete this research comfortably. Finally, I thank the authors of all the publications cited in this thesis, without whose contributions the work presented here could not have been completed.

---

# Contents

<b>Abstract</b>	<b>4</b>
<b>Declaration</b>	<b>5</b>
<b>Related Publications and Patents</b>	<b>6</b>
<b>Acknowledgements</b>	<b>7</b>
<b>List of Tables</b>	<b>12</b>
<b>List of Figures</b>	<b>13</b>
<b>1 Introduction</b>	<b>17</b>
1.1 Research Aims and Thesis Scope . . . . .	18
1.2 Surface Plasmon Amplification by Stimulated Emission of Radiation	20
1.2.1 Surface Plasmons . . . . .	20
1.2.2 Stimulated Emission . . . . .	21
1.2.2.1 Stimulated Emission of Photons and Laser . . . . .	21
1.2.2.2 Stimulated Emission of SPs . . . . .	22
1.2.3 Spaser . . . . .	22
1.2.3.1 Micro and Nanolasers . . . . .	23
1.3 Brief History of Spaser . . . . .	24
1.3.1 Theoretical Work . . . . .	24
1.3.1.1 Proposed Spaser Geometries . . . . .	24

1.3.1.2	Resonator–Gain Medium Interactions . . . . .	26
1.3.2	Experimental Efforts . . . . .	27
1.4	Research In Summary . . . . .	28
<b>2</b>	<b>General Quantum Mechanical Model for Spaser</b>	<b>31</b>
2.1	Resonator–Gain Medium Model . . . . .	31
2.1.0.1	SP Quantization . . . . .	32
2.2	Proposed General Model . . . . .	33
2.2.1	Plasmonic Subsystem . . . . .	33
2.2.1.1	Degeneracy of SP Eigenmodes . . . . .	33
2.2.1.2	SP States . . . . .	34
2.2.2	Electronic Subsystem . . . . .	35
2.2.3	Spaser as an $n$ -State System . . . . .	35
2.3	Spaser Kinetics . . . . .	37
2.3.1	Hamiltonian of the Spaser . . . . .	37
2.3.2	Plasmon Generation Rate . . . . .	39
2.3.2.1	Parameters for Design Optimization . . . . .	40
<b>3</b>	<b>Metal Nanosphere–Quantum Dot Spaser</b>	<b>42</b>
3.1	Spaser Design . . . . .	42
3.2	SP Modes of the Nanosphere . . . . .	44
3.2.1	SP Energies . . . . .	45
3.3	QD Gain Element . . . . .	46
3.4	Applying the General Model for a Dipole Mode Spaser and Design Optimization . . . . .	48
3.4.1	Spaser Mode Energy . . . . .	49
3.4.2	Quantum States of the Spaser . . . . .	49
3.4.3	SP Generation Rate . . . . .	51
3.4.3.1	Optimum $R_1$ and $R_2$ . . . . .	52
3.4.3.2	QD Placement and Size . . . . .	54

3.4.4	Threshold Gain . . . . .	55
<b>4</b>	<b>Spaser Materials and Potential of Carbon</b>	<b>58</b>
4.1	Commonly Used Spaser Materials . . . . .	59
4.1.1	Noble Metals . . . . .	59
4.1.2	Quantum Dots/Wells . . . . .	59
4.1.3	Florescent Dyes and Rare Earth Ions . . . . .	60
4.2	Carbon Allotropes . . . . .	60
4.3	Surface Plasmons in Graphene . . . . .	61
4.3.1	Graphene Plasmonic Resonators . . . . .	62
4.3.1.1	SP Modes of a Square Shaped GNF . . . . .	62
4.4	Carbon Nanotubes . . . . .	65
4.4.1	Density of States of CNTs . . . . .	65
4.4.2	Semiconducting CNTs for Spaser Gain Medium . . . . .	67
<b>5</b>	<b>Graphene–Carbon Nanotube Spaser</b>	<b>69</b>
5.1	Spaser design . . . . .	69
5.2	Implementation of the General Model . . . . .	71
5.2.1	Plasmonic Subsystem . . . . .	71
5.2.2	Electronic Subsystem . . . . .	72
5.2.3	States of the Spaser . . . . .	73
5.3	Design Optimization . . . . .	75
5.3.1	Spaser Mode Energy . . . . .	75
5.3.2	SP Generation Rate . . . . .	75
5.3.3	Threshold Gain and Quality Factor . . . . .	79
5.4	Advantage of the Design . . . . .	83
<b>6</b>	<b>Guidelines for Spaser Design and Optimization</b>	<b>85</b>
6.1	Designing Spaser Components . . . . .	85
6.1.1	Plasmonic Resonator . . . . .	85

6.1.2	Gain Medium . . . . .	86
6.1.3	Pumping Mechanism . . . . .	88
6.2	Operational Characteristics and Optimization Parameters . . . . .	89
6.2.1	SP Generation Rate . . . . .	89
6.2.2	Threshold Gain . . . . .	91
6.2.3	Resonator Quality Factor . . . . .	91
6.2.4	Direction of Symmetry Breaking . . . . .	92
<b>7</b>	<b>Applications of Spasers</b>	<b>93</b>
7.1	SP Sources in Nanoplasmonic Devices . . . . .	93
7.1.1	Logic Circuits and Processors . . . . .	95
7.2	Qbits in Quantum Computers . . . . .	95
7.2.1	Cavity QED Approach . . . . .	96
7.3	In Biomedical Applications . . . . .	97
7.4	Spaser Powered Photothermal Cancer Therapy . . . . .	97
7.4.1	Spaser Operation Near Cancer Cells . . . . .	99
7.4.2	Efficiency of the Therapy . . . . .	102
<b>8</b>	<b>Conclusions and Suggestions for Future Work</b>	<b>109</b>
8.1	Conclusions . . . . .	109
8.2	Suggestions for Future Work . . . . .	111
	<b>Abbreviations</b>	<b>113</b>
	<b>Bibliography</b>	<b>114</b>
	<b>Appendix: Numerical Methods</b>	<b>133</b>

# List of Tables

6.1	Tunability of spaser mode energies for some resonator types [1–6]	. 87
6.2	Characteristics of different gain media [7–15]	. . . . . 88

# List of Figures

1.1	Basic operation of a spaser; gain medium excites SP modes in the resonator by stimulated emission of SPs . . . . .	23
1.2	First structure proposed for a spaser and a plot of its electric field [16, 17]. . . . .	25
1.3	Structure of the first experimentally demonstrated spaser and a microscope image of an ensemble of them [18]. . . . .	28
2.1	Interactions and energy transfers in a spaser . . . . .	32
2.2	SP states of the plasmonic subsystem . . . . .	34
2.3	Exciton states of the electronic subsystem . . . . .	35
2.4	The composite spaser system formed by taking the product states of the gain medium and the degenerate SP states of the spaser mode	36
3.1	Spaser model under consideration: $R_1$ is the nanosphere radius, $R_2$ is the radius of the dielectric shell's outer boundary. A QD is located at the position $\mathbf{r}_0$ with respect to the nanosphere's center. The parameters $\varepsilon_1, \varepsilon_2$ and $\varepsilon_3$ denote the permittivities of the nanosphere, dielectric shell, and ambient, respectively. . . . .	43
3.2	Energy of the spaser mode as a function of the nanosphere radius $R_1$ and the shell thickness $t_{shell} = R_2 - R_1$ . . . . .	50
3.3	Product states of the dipole spaser. . . . .	51

3.4	Normalized SP generation rate is plotted with respect to nanosphere radius $R_1$ and shell thickness $t_{shell}$ when the QD's location is fixed to the middle of the dielectric shell. The drawn curve corresponds to the spaser mode energy 2.385 eV. . . . .	53
3.5	Plot of SP generation rate with respect to the QD's location $r_0$ for different $R_1$ , $R_2$ pairs. . . . .	55
3.6	The normalized SP generation rate is plotted with respect to the QD radius and the shell thickness when the nanosphere radius is fixed to 10 nm and the QD's location is fixed to the middle of the dielectric shell. . . . .	56
3.7	Threshold gain required by pumping with respect to nanosphere radius and shell thickness. . . . .	57
4.1	A square shaped $W$ wide GNF cut from a graphene sheet . . . . .	63
4.2	(a) Normalized electric field distributions of the five lowest-energy modes supported by a square GNF of width $W$ . The mode energies are plotted as functions of (b) Fermi energy for $W = 50$ nm and (c) GNF width for $E_F = 0.4$ eV (the color legend applies to both the plots). . . . .	64
4.3	Formation of a CNT by rolling a graphene sheet . . . . .	66
4.4	Density of states for (10,7), (7,6), and (10,9) carbon nanotubes . . . . .	67
5.1	Schematic of the proposed spaser made of an optically pumped carbon nanotube located above a square graphene nanoflake resonator. . . . .	70
5.2	Plasmonic subsystem of the carbon spaser representing the all SP states with the respective electric field distribution of the each state plotted for the first five modes. . . . .	71
5.3	(a) The excitons having $E_{11}$ and $E_{22}$ energy difference between electron and hole bands marked on the DOS plot of a semiconducting CNT and (b) relevant exciton states of the electronic subsystem. . . . .	72

5.4	Product states of the spaser where the (a) non-degenerate $l = 1$ and (b) doubly degenerate $l = 2$ SP mode is the spaser mode respectively	74
5.5	Spaser mode energy is plotted with respect to (a) Fermi level when $W = 50$ nm and (b) GNF width when $E_F = 0.4$ eV, and (c) the spaser mode and pump energies for CNTs with different chirality $(n, m)$	76
5.6	Configuration of the spaser design	78
5.7	Normalized plasmon generation rates (a) $\mathcal{R}_1$ and (b) $\mathcal{R}_2$ in the $\vartheta$ - $W/L$ domain and (c) $\mathcal{R}_l$ vs $H$ for five lowest-energy spaser modes; $L = 1.1W = 35$ nm, $\theta = \pi/4$ for $l = \{1, 3\}$ and $\theta = 0$ for $l = \{2, 4, 5\}$	80
5.8	(a) $\mathcal{R}_1$ as a function of spaser mode energy for five CNTs, $\theta = \pi/4$ , and $L = 1.1W = 35$ nm and (b) absorption and emission cross sections at resonance for different nanotubes of unit lengths.	81
5.9	(a) Threshold gain vs spaser mode energy for different Fermi energies; (b) quality factor of the first five SP modes vs $E_F$ for $W = 30$ nm.	82
7.1	Speed and critical device dimensions of different technologies [19]	93
7.2	Use of spasers in a nanoplasmonic circuit	94
7.3	Utilization of square GNF's doubly degenerate SP mode $l = 1$ in a spaser to implement $ 0\rangle$ and $ 1\rangle$ qbits	96
7.4	Delivered GNFs and CNTs surround the tumor cells due to targeting mechanisms and becomes a self-assembled cluster of nanolasers	99
7.5	(a) Electric field generated on the GNF resonator, (b) a typical density of states plot of a semiconducting CNT where two lowest energy excitons $E_{11}$ and $E_{22}$ are marked, (c) GNF's resonant wavelengths depending on the width $W$ and Fermi level $E_F$ , and (d) the dependence of the $\lambda_{11}$ and $\lambda_{22}$ wavelengths (corresponding energies $E_{11}$ and $E_{22}$ ) on the chirality $(n, m)$ of CNTs	101

7.6	(a) The temperature after 10s of NIR laser irradiation and (b) time taken to reach $60^{\circ}$ C for different pump power values and number of nanoparticles reached the tumor site . . . . .	106
7.7	The temperature rise with respect to irradiation time (a) for different pump powers when $N_g = 10^{12}$ and (b) for different nanoparticle numbers when pump power is $0.1 \text{ W/cm}^2$ . . . . .	108
A.1	(a) The mesh degenerated for the finite element analysis of a 50 nm wide GNF and (b) the generated electric field plot . . . . .	137

# Chapter 1

## Introduction

The emerging era of nanoplasmonics is expected to improve the speed and efficiency of optical devices by facilitating miniaturization beyond the limitations of conventional optoelectronics [20–23]. It became clearer that, as the technology matures during the last 50 years, the utility and advantages of ‘electronics’ can be surpassed in certain instances by using ‘photons’ [24]. However, the used dimensions in photonic circuits are of the order of micrometers, because the fundamental diffraction limit has intervened to constrain the miniaturization below the subwavelength scale [24, 25]. These barriers are overcome in nanoplasmonic circuits as the signal carriers are in a hybrid particle state between electrons and photons which are known as ‘surface plasmons’ (SPs) [24, 25]. Generally, SPs are excited at metal-dielectric interfaces and therefore endure with the intrinsic losses, severely limiting propagation length to a few wavelengths [25–27]. Therefore, energy must be transferred from an external source to SPs in order to sustain their existence [24]. The spaser (surface plasmon amplification by stimulated emission of radiation) nanolaser, which is the nanoplasmonic counterpart of a conventional laser, is the prime nanodevice that can generate SPs and amplify them [16, 28].

Bergman and Stockman proposed the theory of spaser claiming that a device consisting of a plasmonic resonator and an gain medium (or active medium) can produce coherent SPs by stimulated emission [28]. Spasing occurs due to

the nonradiative energy transfer from the gain medium to the resonator, exciting localized SP modes [17, 28]. A number of theoretical and experimental work based on spasers are available in literature, including proposals for different device designs [28–31], theoretical analyses on the spasing phenomena [16, 17, 32–38], and experimental demonstrations [18, 39–41].

Almost all these work is mainly focused on either physics of SP–matter interactions or proposing new spaser geometries. Hence, less attention has been drawn on engineering aspects of the spaser nanolaser, particularly the models for device optimization, proper design guidelines, and the specific applications where spasers could outperform other devices. Therefore the models, designs, and applications, presented in this thesis attempt to fill that void and discuss the spaser in the engineering domain.

## 1.1 Research Aims and Thesis Scope

### 1. To formulate a general quantum mechanical model to describe the spaser considering the degeneracy of SP modes

Although ample theoretical models are available for resonator–gain media interactions in spasers, it is seen that the output characteristics of a spaser depend much on its design, particularly the properties of its constituents and their relative placement [28–31, 33, 36]. In addition, it is important to study how the degeneracy of SP modes influence spaser kinetics. We address these issues by formulating a general quantum mechanical model describing spaser as  $n$ –state composite system which will be discussed comprehensively in Chapter 2.

### 2. To investigate the means of spaser design optimization

The developed general model can be used to study the influence of material and geometrical parameters on spaser operation. With this understanding, it is possible to optimize a particular spaser design to meet preferred operational char-

acteristics. These methods of optimization are described in Chapters 3 and 5 for different types of spaser designs.

### **3. To design new spaser nanolasers with improved characteristics**

The knowledge obtained through general models and design optimization can be utilised to design new spaser nanolasers for a given application. A couple of different spaser designs are presented in Chapters 3 and 5.

### **4. To study the possibilities of using graphene and carbon nanotubes (CNTs) in spaser designs**

Graphene and CNTs are well known for their unique electrical, optical, and mechanical properties. Over the last couple of decades, these two materials have been extensively researched for nanoelectronics devices. By knowing their important optical properties, we attempt to use them in spaser based nanoplasmonic devices. A carbon based spaser design is presented in Chapter 5 where we show that graphene and CNTs can optically interact.

### **5. To provide comprehensive design guidelines for engineering spaser based devices**

The developed models, designs, and optimizations methods, are useful to characterize the spaser and propose guidelines for designing spaser based devices. The guidelines discussed in Chapter 6 include choosing geometric parameters, plasmonic materials, suitable gain media, appropriate gain media placement, and pumping methods, according to the application requirements.

### **6. To propose new applications of spasers**

As our overall objective is to bring the spaser into the engineering domain, it is important to explore the potential applications. We discuss the possibility of using spaser in future computing devices and biomedical engineering. In particular,

a new cancer therapy based on spaser technology will be presented in detail in Chapter 8.

## 1.2 Surface Plasmon Amplification by Stimulated Emission of Radiation

### 1.2.1 Surface Plasmons

Surface plasmons can be simply described as the coherent oscillations of free electrons on a metal–dielectric interface [25]. A quanta of the electromagnetic field generated due to these electron oscillations could be represented by one SP [42]. Nature of these free electron oscillations depends on the geometry of the metal–dielectric interface. Electron oscillations can propagate if the interface is not confined and such waves are known as ‘surface plasmon polaritons (SPP)’ whereas they are called ‘localized surface plasmons (LSP)’ when the surface geometry constrains wave propagation [25]. The smallest dimension that a wave could be confined is a half of its wavelength, which is called the ‘diffraction limit’. The foremost advantage of SPs is their ability to be confined into nanoscale dimensions with much smaller wavelengths, in contrast to photons whose wavelengths are above 300 nm [24, 25].

SPPs are utilized as signal carriers in nanoplasmonics devices and they propagate along waveguide based circuit paths. Communications applications such as SPP based modulators and switches have already been tested [43–45]. As SPPs are nonradiative in nature, it is difficult to excite SPPs by just irradiating a metal–dielectric interface with photons. Therefore specific maneuvers such as coupling a prism or grating are utilized [25].

In contrast, LSPs are non-propagating oscillations of the free electrons in metal nanoparticles and can be excited by direct illumination of light. The electric field associated with the incident wave generates oscillations of nanoparticle’s free

electrons and the curved boundaries of nanoparticles exerts a restoring force to pull the escaping electrons. This causes a resonance for a given geometry, that generates a maximum electric field for a certain incident wave frequency, which is called ‘surface plasmon resonance (SPR)’ [25].

## 1.2.2 Stimulated Emission

Electrons in atoms are in different orbitals with discrete energy levels. Electrons in lower energy levels are capable of absorbing a photon and excite to a higher energy level. These transitions take place when the energy difference between two levels equals to the incident photon energy and this process is called ‘absorption’. Similarly, an electron in an excited state may relax to a lower energy level emitting a photon without any external influence and this process is known as ‘spontaneous emission’ [46].

Einstein predicted the existence of a third process called ‘stimulated emission’ [47]. He stated that the presence of a photon can also cause the reversed process of the absorption – an excited electron in a higher energy level relaxes to a lower energy level, emitting a photon identical to the incoming photon. Therefore it is said that the incoming photon stimulates the excited electrons to emit an identical photon. This prediction led to the successful demonstration of a maser (microwave amplification by stimulated emission of radiation) in and a laser (light amplification by stimulated emission of radiation) in 1957 [46, 48, 49].

### 1.2.2.1 Stimulated Emission of Photons and Laser

Laser is based on the phenomena of stimulated emission to amplify light. A typical laser is made of a gain medium containing excitable atoms, which is excited by a suitable energy pump, and an optical cavity that provides a feedback. When photons passing through the gain medium, they stimulate the excited electrons to decay and emit identical photons. If the pump source keeps exciting these

active medium, number of emitted photons is multiplied amplifying the output light beam [46, 49]. One of the commonly used optical cavity is a pair of mirrors placed at the two ends of the gain medium. Therefore light is reflected back and forth between the mirrors through the gain medium and amplified each time. Usually one mirror is kept partially reflective so that some percentage of light can escape the cavity, generating laser output. Because the resultant beam consists of identical photons emitted due to stimulated emission process, the laser output can be called a coherent source of light [46].

### 1.2.2.2 Stimulated Emission of SPs

The stimulated emission of photons had been an established phenomena with the availability of commercial laser devices when Bergman and Stockman predicted the possibility of stimulated emission of SPs in 2003 [28]. Similar to photons, SPs are bosons with spin 1 and electrically neutral [16]. Therefore, they claimed that SPs can undergo stimulated emission similar to photons do in lasers [16]. Seidel *et al.* experimentally proved this theoretical concept in 2005 using an attenuated-total-reflection setup [41]. They have detected stimulated emission of SPs at the interface between a silver film and an optically pumped dye solution acting as the gain medium. The results showed that experimental observations were in excellent with theoretical predictions.

### 1.2.3 Spaser

Analogues to the generation of coherent light by stimulated emission of photons in lasers, it is possible to design a device functioning as a coherent SP source by stimulated emission of SPs, which has been termed as ‘spaser’ [32]. As shown in Fig.1.1, a typical spaser consists of a plasmonic resonator (similar to the laser cavity) which supports SP modes, and a gain medium which supplies energy to amplify them. Usually a metallic nanoparticle is used for the plasmonic resonator

as they have enough free electrons to allow localized SP oscillations. During the spaser operation, gain medium continuously gets excited when it receives sufficient energy from an external pump source. These excited electrons are stimulated by the resonant SP modes of the resonator to relax and transfer energy to the same SP modes, very much resembling the feedback provided by the resonant cavity in lasers. By this process, one SP mode could be built up to a large number SPs which will result in a massive field concentration within an ultra-small volume of a nanoparticle [18, 28, 32].

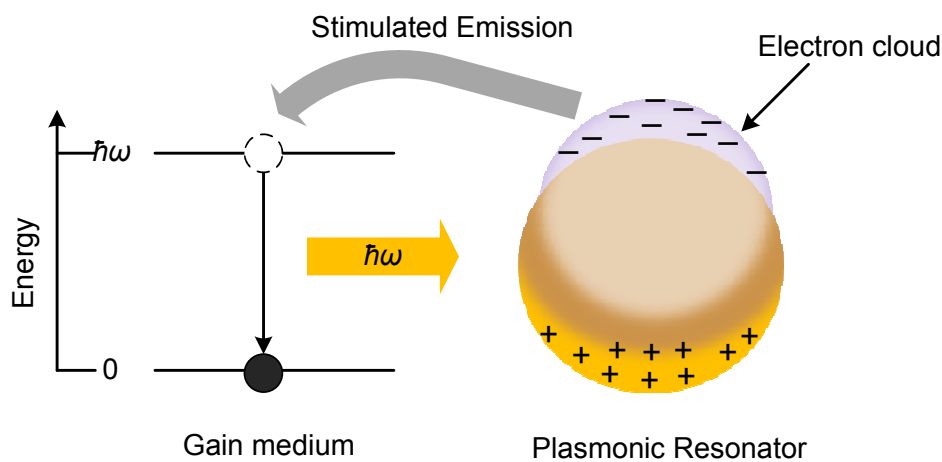


**Figure 1.1:** Basic operation of a spaser; gain medium excites SP modes in the resonator by stimulated emission of SPs

### 1.2.3.1 Micro and Nanolasers

Since miniaturization of a laser cavity is restricted by the diffraction limit, which is half a wavelength, making a real nanoscale laser is impossible. This is because the light wavelengths are above 300 nm and the nanoscale is below 100 nm [25, 50]. Therefore, it is only possible to have ‘microlasers’ where stimulated emission of photons takes place [51, 52].

However there is no such constrain for the plasmonic resonator of a spaser. Lo-

calization dimensions of SPs are only limited by the non-locality radius,  $l_{nl} = v_F/\omega$  (where  $v_F$  is Fermi velocity and  $\omega$  is the SP angular frequency), which is about 1 nm for noble metals, where effects such as Landau damping arise [42]. Therefore nanoscale device dimensions are readily achievable for spasers and any device called ‘nanolaser’ should employ the mechanism of stimulated emission of SPs. In other words all nanolasers are essentially spasers, thus sometimes spasers are called ‘nanolasers’ or ‘spaser nanolasers’ [17]. But converse may not be true, because a spaser can be of microscale as well. There are ample literature of plasmonic micro-resonators (or micro-cavities) being demonstrated [53, 54]. It is possible to use them with suitable gain medium to construct microscale spasers.

## 1.3 Brief History of Spaser

Since 2003, there has been tremendous progress in the research on spasers. While some theoretical studies attempt to introduce different spaser configurations and analyze the resonator-active medium interactions, several noteworthy experimental efforts focus on realizing spasers in practice. Here we highlight some remarkable contributions.

### 1.3.1 Theoretical Work

#### 1.3.1.1 Proposed Spaser Geometries

Several structures have been proposed for spasers. First of them is made of a V-shaped metallic nanoparticle that act as the plasmonic resonator attached to semiconductor quantum dots (QD) providing the gain as illustrated in Fig. 1.2 [28]. This theoretical contribution also proposed the plasmonic field quantization and analyzed the gain provided by QDs.

Influenced by the concept of metamaterials, another study proposed a spaser geometry where a two-dimensional array of split-ring shape plasmonic resonators

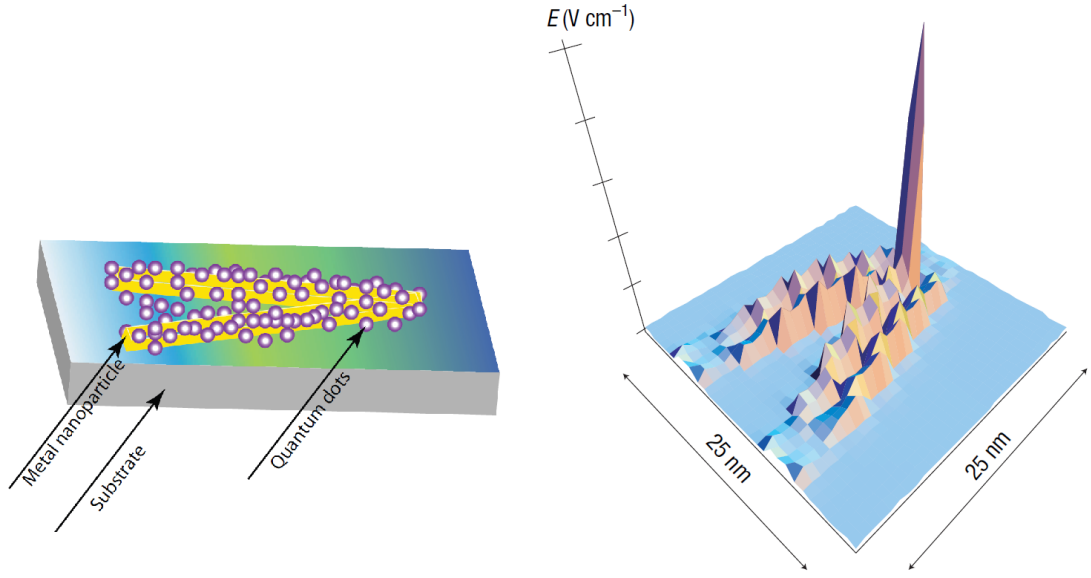


**Figure 1.2:** First structure proposed for a spaser and a plot of its electric field [16, 17].

is supported by a substrate acting as the gain medium [30]. It acts as a source of coherent radiation caused by plasmonic resonances which authors called a ‘lasing spaser’. In addition, a bowtie-shaped metallic structure, in which QDs are placed in the bowtie gap and multiple quantum wells are located in the substrate [31], a metal groove with QDs placed at its bottom [29], and a spaser design with electrically pumped nanowire gain medium [55], are among the notable spaser geometries.

Even though most of these spaser designs employ QDs in the gain medium, it is possible to use quantum wells, rare-earth ions or dyes, as excitable gain elements [24, 56]. QDs are widely used in many lasing setups as well [57–61]. As the charge carriers in a QD are confined in all three dimensions to a very small size, its density of states (DOS) almost resembles a set of delta functions, mimicking an atomistic behavior with a well defined spectral response [60, 62, 63]. They also promise a better stability over temperature variations [61].

### 1.3.1.2 Resonator–Gain Medium Interactions

Many theoretical studies have been performed on interaction between gain elements and either localized or propagating SPs (LSPs or SPPs). In the initial work to study spaser kinetics and determine spaser characteristics, Stockman *et al.* have quantum mechanically analyzed the interaction between a metal nanoparticle and closely located gain elements, which are modeled as two level systems (TLS), where a pump source is present to continuously excite them [28, 32]. In this analysis, plasmonic field is first quantized so that a quanta of SP mode  $l$  possesses an energy of  $\hbar\omega_l$ , where  $\omega_l$  is the mode angular frequency, and SP creation and annihilation operators are defined. Then the spaser Hamiltonian has been derived treating the SP-TLS interactions quantum mechanically and the pump photon-TLS interactions quasiclassically. This Hamiltonian has been used with density matrix analysis in order to obtain operating spaser characteristics such as threshold spasing condition, spasing frequency, and spaser linewidth [16, 28, 32, 42]. However, this analysis does not consider the SP degeneracy which could be important in design aspects of the device. Therefore this work is extended in Chapter 2 to develop a more generalized quantum mechanical model for spasers.

Khurgin *et al.* have discussed the threshold spasing condition, linewidth, and coherence, of a spaser in Refs. [33, 64]. Considering a simple spaser formed of a two level QD attached to a metal nanoparticle, Andrianov *et al.* have examined some attributes of spasers such as dipole response to an optical wave [34], external forced synchronization [35], and occurrence of Rabi oscillations [65].

Among the work on emitted radiation from nanoparticle-TLS ensembles, Ref. [37] that studies the resultant photon statistics, Ref. [36], an examination of the polarization of emitted photons of a ‘dipole nanolaser’, and Ref. [38] which presents the spectral properties, are conspicuous. The theory of the spaser also suggests that propagating SPs can be amplified by placing a gain medium in the vicinity [24]. This idea has been exploited to compensate the losses in metamaterials. A few

of such utilizations are described in Refs. [66, 67] where SP-TLS interactions and Refs. [68, 69] in which SP-four level system interactions are analyzed.

Although significant research has been published on SP-active media interactions, it is seen that spaser operation highly depend on the design parameters. Most of these studies are very much focused on the role of the active medium and there is a need for comprehensive analysis for spasers. Most importantly, it is required to analyze the influence of the degeneracy of the SP modes on operational spaser characteristics such as the spaser mode energy, SP generation rate, threshold gain and resonator quality factor. Having these information, a spaser can be further optimized and clear design guidelines for spasers can be developed as described in the following chapters of this thesis.

### 1.3.2 Experimental Efforts

Since its theoretical formulation, many experimental efforts have been carried out to fabricate a spaser. Although we have seen ‘stimulated emission of photons’ in lasers, it is essential to prove the concept of ‘stimulated emission of SPs’ in practice. This was done by Seidel *et al.* who amplified SPs at the interface between a flat continuous silver film and a liquid containing organic dye molecules [41].

Plum *et al.* demonstrated that a combination of a metamaterial with a layer of QDs can influence its optical properties [40]. When they optically pumped a layer of deposited QDs on a metamaterial, its resonant transmission was altered resulting in a reduction of Joule losses. This was the first step towards the demonstration of a metamaterial gain device. Another loss compensation was reported by Flynn *et al.* who sandwiched a gold-film plasmonic waveguide between optically pumped InGaAs quantum wells [39].

The first demonstration of a spaser was done by Noginov *et al* in 2009 [18]. They used a gold nanosphere with a radius of 7 nm surrounded by the gain medium which is a 15 nm thick silica shell containing dye molecules. When the dye is optically pumped, it released energy to the gold nanosphere causing excitation of localized

SPs. The size of the whole spaser geometry was reported to be 44 nm as shown in Fig. 1.3.

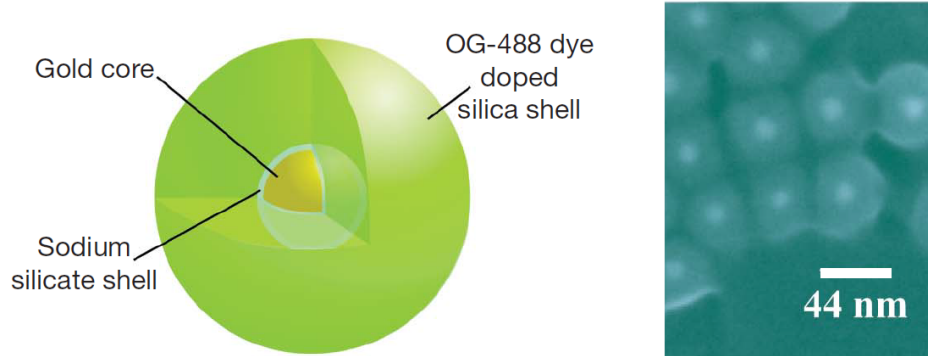


**Figure 1.3:** Structure of the first experimentally demonstrated spaser and a microscope image of an ensemble of them [18].

## 1.4 Research In Summary

In spaser, stimulated emission of SPs occurs as a result of the interactions between SP modes of the plasmonic resonator and the electrons (or excitons) of the active medium, where external energy pumping is present. The nature of these interactions may depend on many factors including the size parameters of spaser components, their relative placement, and the materials used. Therefore, the first step of this research is to develop a general quantum mechanical model for spaser nanolasers to find how these design parameters influence the SP–exciton interactions and performance of a spaser. A new model is needed because the existing theories, which focus more on the kinetics of the active medium, do not consider the degeneracy of SP modes - an important parameter in device design. Analyses based on this model shows that, due to the availability of different degenerate SP states, a spaser can produce a completely different output after a slight alteration

of the geometry. This happens because of the change in the particular SP-exciton interaction matrix elements and its influence on the kinetics of the entire system.

The next step of this research is to apply the developed general model to a spaser with a simple design in which an optically pumped QD gain element supplies energy to the localized SPs of a gold nanosphere. Although, a spaser may consist of a large number of gain elements powering the resonator modes in practice, the proposed method can be readily adopted to describe such spasers, provided that no significant interaction exists among gain elements, thus the principle of superposition prevails [18, 42].

These steps of the research helps to verify that operational characteristics of a spaser—such as SP generation rate, emission wavelength, SP quality factor, and threshold gain—strongly depend on the spaser’s geometry and composition [70]. Although many spaser designs have been proposed and analyzed in search of the best performance, they are mostly based on noble-metal plasmonic nanocavities of different geometries coupled to semiconductor quantum dot/well gain media. Therefore new materials, especially the carbon allotropes, are considered for spaser components and a unique all-carbon spaser is proposed where a graphene nanoflake resonator is powered by a carbon nanotube (CNT) gain element. Graphene and CNTs are widely used in optoelectronic applications due to their remarkable optical and electronic properties. They possess a honeycomb lattice structure, with carbon atoms in  $sp^2$  hybridization [71]. Furthermore, graphene SPs provide better confinement, lower dissipation, and higher tunability than the SPs of noble metals and also provides a unique playground for the realization and studying strong light–matter interactions [72, 73]. Similarly, semiconducting CNTs are well known for generating excitons *via* optical absorption, and having absorption and emission parameters that are strongly dependent on their chirality [71, 74–77]. The performance of this spaser is then investigated as a means of design optimization. In addition, this design offers many advantages including mechanical strength and flexibility, thermal and chemical stability, and utility in biomedical applications

inherited with carbon allotropes [71, 75, 77, 78].

As the final stage of our research, we try to propose the potential applications where spasers can perform much efficiently than other alternatives, especially in computing devices and biomedical engineering. It has been suggested that spaser can perform as ultrafast amplifiers and quantum generators [32]. This capability hints that spasers can act as a building block in future information processing devices. Being ultra-fast and ultra-small, spaser based devices can revolutionize the field of consumer electronics. Similarly, biomedical engineering is a promising area with many potential applications. In this study, an important biomedical application; a new cancer therapy based on spaser nanolasers, is proposed. It is an improved version of the photothermal cancer therapy where guided spaser nanolasers are used to raise the temperature of malignant cells to cause selective cell destruction [4, 79, 80]. In the proposed method of treatment, a cluster of spasers self-assembled of graphene and CNTs operate close to cancer cells concentrating optical energy in large scale. This results in building up a strong electric field on graphene resonators and heat generation, causing thermal ablation of the malignant cancer cells. The method of treatment is proposed and the Efficiency of this therapy over the conventional phototherapy therapy is shown through simulations.

# Chapter 2

## General Quantum Mechanical Model for Spaser

### 2.1 Resonator–Gain Medium Model

Plasmonic resonator, gain medium, and pumping mechanism, are the essential components to construct a spaser. Generally, plasmonic resonator is a metal nanoparticle which supports a series of SP modes denoted by  $l = 1, 2, 3, \dots$ , having angular frequencies  $\omega_l$ , in the order of increasing energy. Spaser operation is based on two main types of interactions; between pump source–gain medium and gain medium–resonator. Figure 2.1 shows a basic interaction diagram of a spaser for the case of optical pumping, in which a light source of angular frequency  $\omega_L$  is used to excite the gain medium. By absorbing this energy, the gain medium can generate electron–hole (e–h) pairs of energy  $\hbar\omega_L$ . Then these e–h pairs relax forming excitons having a slightly less energy, say  $\hbar\omega_e$ . This implies that the gain medium is a three level system. However, Bergman and Stockman assume the  $3 \rightarrow 2$  transition to be a fast relaxation in their model, allowing it to be treated as a two level system in theory [28, 42].

When  $\hbar\omega_e = \hbar\omega_l$  for a certain SP mode  $l$ , and the resonator and gain medium are coupled sufficiently close allowing near field interactions, high energy excitons

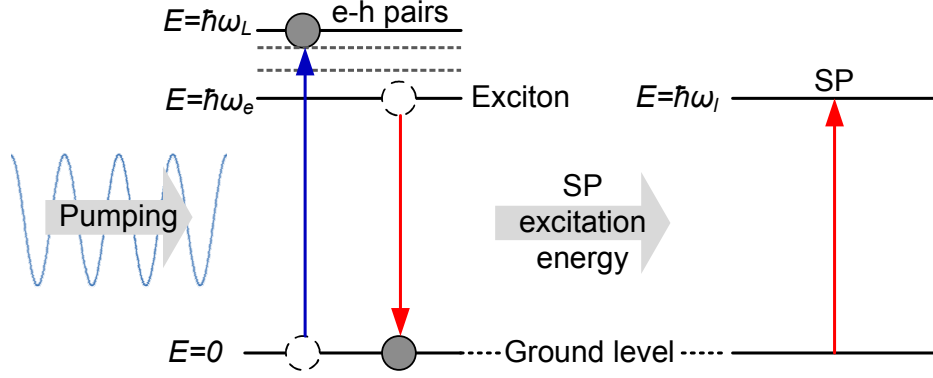


**Figure 2.1:** Interactions and energy transfers in a spaser

are stimulated to annihilate with  $2 \rightarrow 1$  transition, transferring  $\hbar\omega_l$  energy to the SP mode  $l$ . Hence only the  $l$ th SP mode receives energy and get amplified in this scenario becoming the dominant ‘spaser mode’ [42]. Other modes are not excited at all and therefore a highly coherent electric field is concentrated in the resonator volume. Another advantage of spasers is their ability to excite dark modes, the modes that cannot be excited by direct illumination (*i.e.* far field coupling). Therefore, these dark SP modes do not emit light and undergo radiative losses.

### 2.1.0.1 SP Quantization

In the theory of the spaser, SPs are quantized to be treated quantum mechanically. This is done by writing the operator for the total electric field vector as the sum of the fields  $\mathbf{E}_l(\mathbf{r})$  excited due to each SP mode [28, 42]:

$$\hat{\mathbf{E}}(\mathbf{r}) = \sum_l A_l \mathbf{E}_l(\mathbf{r})(\hat{b}_l + \hat{b}_l^\dagger), \quad (2.1)$$

where  $\hat{b}_l^\dagger$  and  $\hat{b}_l$  are the SP creation and annihilation operators of the  $l$  th mode (given by  $\hat{b}_l |n+1\rangle = |n\rangle$  and  $\hat{b}_l^\dagger |n\rangle = |n+1\rangle$  for bosons), and  $A_l$  is a normalization constant found by solving the equation of second quantization within dispersive

media [81, 82]:

$$\int_V \frac{1}{2} \frac{\partial}{\partial \omega} (\omega \varepsilon(\omega)) |A_l \mathbf{E}_l(\mathbf{r})|^2 d\mathbf{r} = \hbar \omega_l. \quad (2.2)$$

When the SPs are quantized, the SP–exciton interactions can be analysed quantum mechanically to study the operating spaser characteristics according to Ref. [28]. However, before doing such analysis, we extend this basic resonator–gain medium model considering the degeneracy of SP modes, an important parameter in design optimization.

## 2.2 Proposed General Model

Referring Fig. 2.1, we can notice that a spaser’s state can be given by a pair of states; the exciton state and the SP state. Hence, it is possible to state that a typical spaser consists of two main subsystems; which we call the ‘electronic subsystem’ and ‘plasmonic subsystem’. Making a spaser is nothing but the resonant coupling of these two subsystems.

### 2.2.1 Plasmonic Subsystem

#### 2.2.1.1 Degeneracy of SP Eigenmodes

Although the plasmonic resonator of a spaser supports a series of SP eigenmodes denoted by  $l = 1, 2, 3, \dots$ , there can be multiple solutions for the electric field  $\mathbf{E}_l(\mathbf{r})$  of a particular mode  $l$ , especially when the resonator is symmetric in shape [83]. For example, the  $l$ th SP mode of a spherical nanoparticle is  $2l + 1$  times degenerate [84]. If the spaser mode is one such SP mode, each degenerate SP state may not receive energy equally from the gain medium although the coupling is resonant. To analyse this situation and study how different degeneracies are amplified, we further generalize the basic resonator–gain medium model with added degenerate SP states to the plasmonic subsystem.

### 2.2.1.2 SP States

The plasmonic resonator can possess many energy levels, including the ground level with energy 0 and the SP states of energy  $\hbar\omega_l$ . Therefore, if the  $l$ th SP mode is  $M_l$  times degenerate, the total number of SP states becomes  $1 + \sum_l M_l$  as shown in Fig. 2.2 below. Hence, any SP state can be denoted by an integer pair  $(l, m)$  where  $m = 1, 2, 3, \dots, M_l$ . The value of  $M_l$  totally depends on the resonator geometry which will be explained with examples in the Chapters 3 and 4. In our notation, we define the ground SP state by  $|0p\rangle$  and any other general state with one SP by  $|1p^{(l,m)}\rangle$ , where ‘ $p$ ’ indicates the plasmonic subsystem.

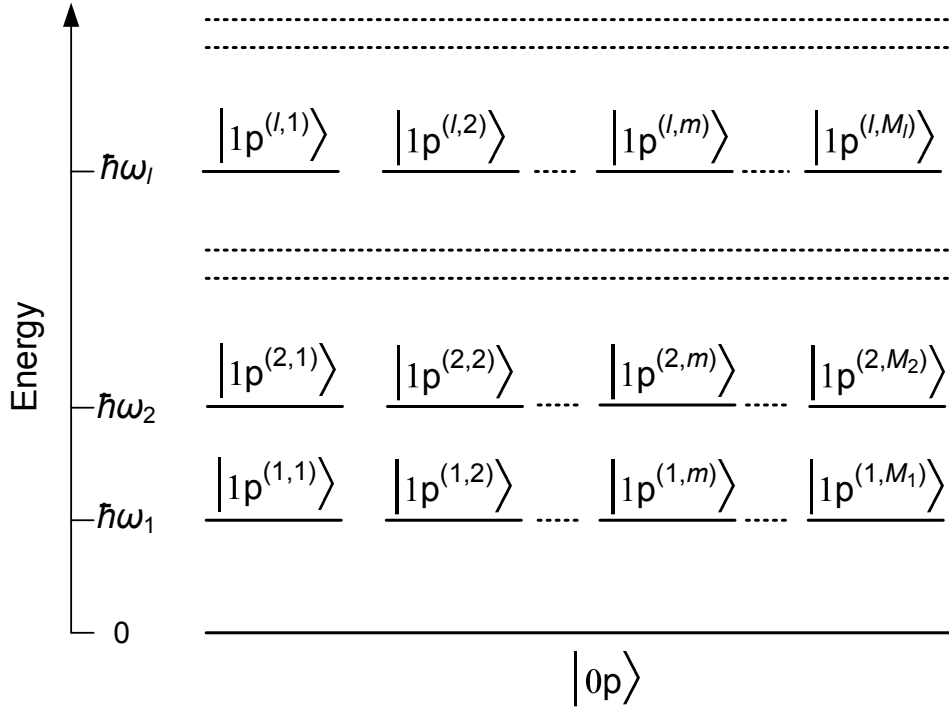


**Figure 2.2:** SP states of the plasmonic subsystem

### 2.2.2 Electronic Subsystem

Despite the typical gain elements such as QD nanocrystals, QW, or dye molecules, have many energy levels in their band structure, it is sufficient to consider 3 main levels in order to study the operation of lasers or spasers [85]. Following a similar notation to the plasmonic subsystem, we denote the ground state of the electronic subsystem by  $|0e\rangle$ , the relaxed exciton state by  $|1e\rangle$ , and the high energy e-h pair state by  $|2e\rangle$  which are assumed to possess the energies 0,  $\hbar\omega_{11}$ , and  $\hbar\omega_{22}$ , respectively as shown in Fig. 2.3.

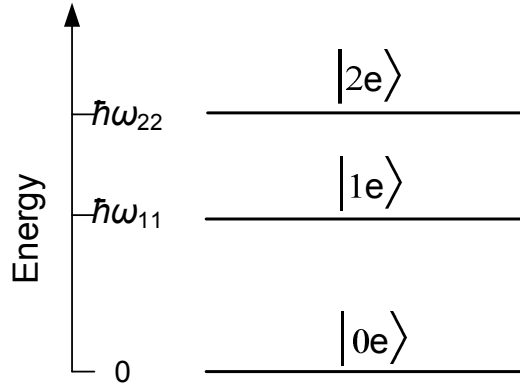


**Figure 2.3:** Exciton states of the electronic subsystem

### 2.2.3 Spaser as an $n$ -State System

Although we have identified the spaser as two different subsystems, it is a single composite system which operates as a SP generation device. Hence, it is possible to define the states of this composite system as the tensor product of the states of the plasmonic and electronic subsystems [86]. However, only the spaser mode is resonantly coupled to the gain medium because only one mode would satisfy the condition  $\hbar\omega_{11} = \hbar\omega_l$ . Therefore, it is sufficient to assume that only the spaser mode would significantly interact with the gain medium so that the states

representing other SP modes can be omitted in analysis.

Figure 2.4 illustrates the main product states of a spaser where a general SP mode  $l$  interacting with the gain medium excitons. The state  $|1\rangle = |0e\rangle|0p\rangle$  is the energy zero ground state of the composite system. By absorbing pump energy  $\hbar\omega_L \approx \hbar\omega_{22}$ , the spaser can excite to the state  $|3\rangle = |2e\rangle|0p\rangle$  by forming e-h pairs with the  $|1\rangle \rightarrow |3\rangle$  transition. These e-h pairs form excitons with  $|3\rangle \rightsquigarrow |2\rangle$  energy relaxation where the state  $|2\rangle = |1e\rangle|0p\rangle$  possesses an energy of  $\hbar\omega_{11}$ . In this transition, an small amount of energy equivalent to  $\hbar(\omega_{22} - \omega_{11})$  is dissipated to the environment. When the spaser is at  $|2\rangle$ , it is stimulated by the spaser mode SPs in the resonator with the resonant energy  $\hbar\omega_l = \hbar\omega_{11}$  to excite (or emit) an identical SP and relax into one of the states  $|4\rangle = |0e\rangle|1p^{l,1}\rangle$ ,  $|5\rangle = |0e\rangle|1p^{l,2}\rangle$ , ...,  $|n\rangle = |0e\rangle|1p^{l,M_l}\rangle$  where  $n = M_l + 3$ . The likelihood of transition to each of these states depends on how strong each degenerate SP mode  $(l, m)$  interacts with the gain medium excitons, which we analyse by studying the spaser kinetics.

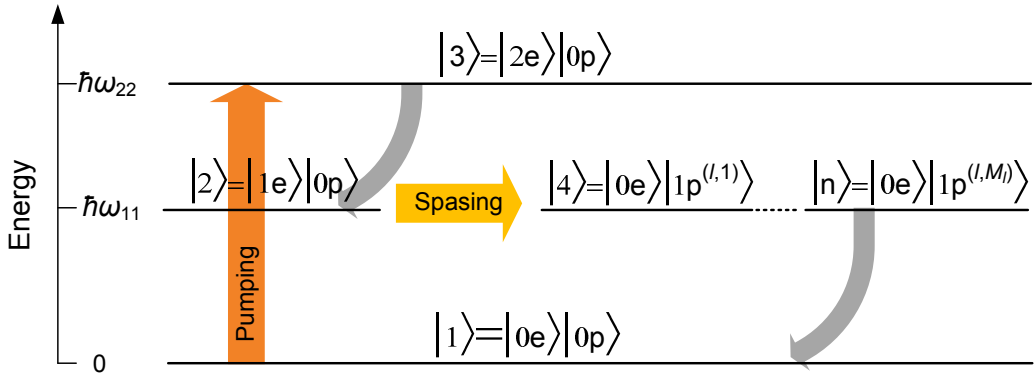


**Figure 2.4:** The composite spaser system formed by taking the product states of the gain medium and the degenerate SP states of the spaser mode

## 2.3 Spaser Kinetics

### 2.3.1 Hamiltonian of the Spaser

Since the spaser is modeled as a composite quantum system, its Hamiltonian  $H(t)$  can be given by the summation of the Hamiltonians of the non interacting states of the electronic and plasmonic subsystems;  $H_e$  and  $H_p$ , and the Hamiltonian of the interacting states  $H_i$  [28]:

$$H(t) = H_e + H_p + H_i(t). \quad (2.3)$$

The Hamiltonian of the non-interacting electronic subsystem is the sum of the operators  $\hbar\omega_a |a\rangle \langle a|$  which creates an exciton of energy  $\hbar\omega_a$  by acting on  $|a\rangle$ :

$$H_e = \hbar\omega_{11} |1e\rangle \langle 1e| + \hbar\omega_{22} |2e\rangle \langle 2e|. \quad (2.4)$$

Here the state  $|0e\rangle$  is omitted because its energy is 0, therefore  $H_e |0e\rangle = 0$ . Similarly, the Hamiltonian of non-interacting SPs,  $H_p$  can be written in terms of the creation and annihilation operators  $\hat{b}_{l,m}^\dagger, \hat{b}_{l,m}$  of SPs corresponding to the quantum numbers  $l$  and  $m$ :

$$H_p = \sum_{m=1}^{M_l} \hbar\omega_l \hat{b}_{l,m}^\dagger \hat{b}_{l,m}. \quad (2.5)$$

There are two types of interactions in a spaser; between the gain medium excitons and the pump light, and the excitons and the SPs of the resonator. Therefore the Hamiltonian of the interacting particles  $H_i$  can be decomposed into two parts:

$$H_i(t) = H_{e,L}(t) + H_{e,p}. \quad (2.6)$$

where  $H_{e,L}$  and  $H_{e,p}$  represent excitons–pump light and excitons–SP interactions respectively. In this analysis, we consider pump light classically treating it as wave of  $\omega_L$  angular frequency with an envelop function  $\varphi(t)$ . However, the SPs are incorporated quantum mechanically. Hence, the Hamiltonians for these interactions

can be given by,

$$H_{e,L}(t) = \frac{\varphi(t)V_{2e,0e}}{2} e^{-i\omega_L t} |2e\rangle \langle 0e| + \text{c.c.}, \quad (2.7)$$

$$H_{e,p} = i\hbar g_l \sum_{m=0}^{M_l} V_{1e,0e}^{l,m} \hat{b}_{l,m}^\dagger |0e\rangle \langle 1e| + \text{c.c.}, \quad (2.8)$$

where  $V_{f,i}$  is the coupling coefficient matrix element for the transition  $|i\rangle \rightarrow |f\rangle$ ,  $i, f = \{0e, 1e, 2e\}$ ,  $g_l = \sqrt{\omega_l/2\varepsilon_g V_n}$ ,  $\varepsilon_g$  is the permittivity of the medium,  $V_n$  is the normalization volume, and c.c. represents the complex conjugate [87–89]. The operator  $|f\rangle \langle i|$  annihilates one particle in the initial state  $|i\rangle$  and creates one particle in the final state  $|f\rangle$  instead.

Then the matrix element  $V_{f,i}^{l,m}$  corresponding to the SP–exciton interactions can be written as

$$V_{f,i}^{l,m} = \langle f | \mathbf{E}_{lm} \cdot \mathbf{x} | i \rangle = \langle f | \langle u_c | \mathbf{E}_{lm} \cdot \mathbf{x} | u_v \rangle | i \rangle, \quad (2.9)$$

where  $\mathbf{E}_{lm}$  is the electric field excited due to one  $(l, m)$  SP,  $|u_c\rangle$  and  $|u_v\rangle$  are the Bloch functions, and  $\mathbf{x}$  is the displacement vector of the excitons [89, 90]. Assuming the equality  $\mathbf{E}_{lm} = E_{lm} \mathbf{e}_{lm}$ , we may write

$$V_{f,i}^{l,m} = \langle u_c | \mathbf{e}_{lm} \cdot \mathbf{x} | u_v \rangle \langle f | E_{lm} | i \rangle, \quad (2.10)$$

The first matrix element in the right hand side can be expressed through the Kane’s parameter  $P$  and the bandgap  $E_g$  as  $\langle u_c | \mathbf{e}_{l_p m_p} \cdot \mathbf{x} | u_v \rangle = \sqrt{2}P/E_g$  [91, 92], and the second matrix element,  $\langle f | E_{lm} | i \rangle = \Upsilon_{f,i}^{l,m}$ , can be expressed by

$$\Upsilon_{f,i}^{l,m} = \int_V \psi_f^*(\mathbf{r}) E_{lm}(\mathbf{r}) \psi_i(\mathbf{r}) \, d\mathbf{r}, \quad (2.11)$$

In the case where the gain element is very small compared to the resonator (*e.g.* a QD), it is reasonable to assume that  $E_{lm}(\mathbf{r})$  is approximately constant over the QD’s volume, therefore the integral in Eq. (2.11) can be simplified to:

$$\Upsilon_{f,i}^{l,m} = E_{lm}(\mathbf{r}_0) \delta_{f,i} \quad (2.12)$$

where  $\mathbf{r}_0$  is the position of the gain element. However, generally from Eq. (2.10) and Eq. (2.11), the matrix element for the SP–exciton interactions is given by

$$V_{f,i}^{l,m} = \frac{\sqrt{2}P}{E_g} \Upsilon_{f,i}^{l,m}. \quad (2.13)$$

Since this quantity determines the contribution to the total Hamiltonian by the interactions of the spaser mode with the gain element, it is also an estimation of the strength of spasing. When evaluating the matrix element  $V_{2e,0e}$ , electric field term  $\mathbf{E}_{lm}$  in Eq. (2.9) should be replaced by the electric field generated by the pump light.

### 2.3.2 Plasmon Generation Rate

Having the Hamiltonian calculated, we can analyze the  $n$  states system comprises of the product states  $|1_s\rangle, |2_s\rangle, \dots, |n_s\rangle$ , using the density matrix formalism. We define the populations of the  $n$  states by  $\rho_{11}, \rho_{22}, \dots, \rho_{nn}$  and assume that the system has a short-term memory and its ambient is the reservoir for system’s dissipations [93]. Then the relaxation superoperator, which is added to the commuted Hamiltonian and density operator to incorporate dissipations, consists of a set of constants that define the relaxation kinetics of the diagonal and off-diagonal elements of the reduced density matrix [87, 93]. Using the Markov and secular approximations, master equation of such a system can be given by [94]

$$\frac{\partial \rho_{\mu\nu}(t)}{\partial t} = \frac{1}{i\hbar} [H(t), \rho(t)]_{\mu\nu} - \gamma_{\mu\nu} \rho_{\mu\nu}(t) + \delta_{\mu\nu} \sum_{\kappa \neq \nu} \xi_{\nu\kappa} \rho_{\kappa\kappa}(t), \quad (2.14)$$

where  $\gamma_{\mu\mu}$  is the population relaxation rate of the state  $|\mu\rangle$ ,  $\gamma_{\mu\nu} = (\gamma_{\mu\mu} + \gamma_{\nu\nu})/2 + \hat{\gamma}_{\mu\nu}$  is the coherence relaxation rate between the states  $|\mu\rangle$  and  $|\nu\rangle$ ,  $\hat{\gamma}_{\mu\nu}$  is the pure dephasing rate, and  $\xi_{\nu\kappa}$  is the transition rate from state  $|\kappa\rangle$  to state  $|\nu\rangle$  due to interaction with the environment. We assume that the lifetime of the ground state  $|1\rangle$  is very large, by setting  $\gamma_{11} = 0$ . The parameters  $\gamma_{44}, \gamma_{55}, \dots, \gamma_{nn}$  define the dissipation of degenerated states of the SP mode denoted by  $(l, m)$  quantum numbers. However, since the energy and dielectric properties are common for all

the degenerated SP states, we assume that all the spaser mode SP dissipation constants are equal, and can be denoted by  $\gamma_p$ .

Populations  $\rho_{44}, \rho_{55}, \dots, \rho_{nn}$  represent the excitation rates for the SP modes  $(l, m) = (l, 1), (l, 2), \dots, (l, M_l)$  respectively. Therefore, the total SP generation rate of the  $l$ th mode,  $\mathcal{R}_l$  is the sum of those populations. We can solve the system of partial differential equations given in the Eq. (2.14) for the continuous wave (CW) operation assuming that  $\varphi(t) = 1$  and obtain an expression for the total SP generation rate given by

$$\mathcal{R}_l = \sum_{j=4}^n \frac{\omega_l^2}{2\varepsilon_2 \hbar} \frac{\xi_{23}}{\gamma_{22}\gamma_{33}\gamma_{jj}} \frac{\gamma_{13}}{\gamma_{13}^2 + \Delta_{L3}^2} \frac{\gamma_{2j}}{\gamma_{2j}^2 + \Delta_{2j}^2} |V_{2e,0e}|^2 |V_{1e,0e}^{l,j-3}|^2, \quad (2.15)$$

where  $\Delta_{L3} = \omega_L - \omega'_3$ ,  $\Delta_{2j} = \omega'_2 - \omega'_j$  when  $\hbar\omega'_2$ ,  $\hbar\omega'_3$ , and  $\hbar\omega'_j$ , are the energies of the states  $|2\rangle$ ,  $|3\rangle$ , and  $|j\rangle$ , respectively. Since all the degenerate SP modes have the same energy  $\omega'_j = \omega_l \forall j$ , therefore  $\Delta_{2j} = \Delta_{2l}$ . We can assume that the detuning of the energy of the pump light with the energy of the state  $|3\rangle$ ,  $\Delta_{L3} \ll \gamma_{13}$  (*i.e.*  $\omega_L \simeq \omega_{11}$ ), hence  $\frac{\gamma_{13}}{\gamma_{13}^2 + \Delta_{L3}^2} \simeq \frac{1}{\gamma_{13}}$ . Further, we also assume that all degenerate SPs of the same mode  $l$  decay equally and therefore  $\gamma_{jj} = \gamma_p$  and  $\gamma_{2j} = \gamma_{2p} \forall j$ . With these simplifications, Eq. (2.15) can be further reduced to:

$$\mathcal{R}_l = \frac{\xi_{23}\omega_l^2}{2\varepsilon_2 \hbar \gamma_{13}\gamma_{22}\gamma_{33}\gamma_p} \frac{\gamma_{2p}}{\gamma_{2p}^2 + \Delta_{2p}^2} |V_{2e,0e}|^2 \sum_{j=4}^n |V_{1e,0e}^{l,j-3}|^2. \quad (2.16)$$

### 2.3.2.1 Parameters for Design Optimization

Suppose all the decay rates and the transition rates due to interaction with the environment are constant for given materials. In that case, the total SP generation rate of the spaser,  $\mathcal{R}_l$  mainly depends on the matrix elements for the exciton-SP interactions  $V_{1e,0e}^{l,m}$ , pump light-exciton interactions  $V_{2e,0e}$ , and the detuning  $\Delta_{2p}$ . If exact resonance is achieved,  $\Delta_{2p} = 0$  and we achieve the highest SP generation rate. Therefore, from Eqs. (2.16) and (2.10) it is clear that there are many material and geometrical parameters which influence the SP generation rate of a spaser as they are directly related to the interaction matrix elements. In addition, the parameter

$\rho_{jj}$  represents the likelihood of each degenerate mode to be excited, which gives an idea of the exact resultant electric field distribution. Since our general quantum mechanical gives an idea of the spaser's output and the relevant tuning parameters, it is possible to utilize it as a platform for design optimization of spasers. In order to investigate the means of doing that, we apply this model on a simple spherical spaser design and analyse its performance in Chapter 3.

# Chapter 3

## Metal Nanosphere–Quantum Dot Spaser

As described in Chapter 2, a typical spaser consists of a plasmonic resonator which supports SP modes and a gain medium which amplifies them. Having developed a new general quantum mechanical model that considers the degeneracy of SP modes, in this chapter we apply it to study a simple spaser design with a spherical geometry for design optimization. In this study, the optimum design parameters of this spherical spaser are sought to achieve a high SP generation rate.

### 3.1 Spaser Design

Figure 3.1 shows a schematic diagram of the considered spaser design in which the plasmonic resonator is a metal nanosphere surrounded by dielectric shell, and a QD is embedded in the shell as a gain element. Spasing occurs when the QD transfers energy nonradiatively to the nanosphere exciting localized SPs due to stimulated emission with pumping is present.

The spherical core-shell structure is one of the most studied geometries for surface plasmon resonance, because it is one of the few geometries where Maxwell's equations can be analytically solved [2, 84, 95–97]. Suppose the inner radius of

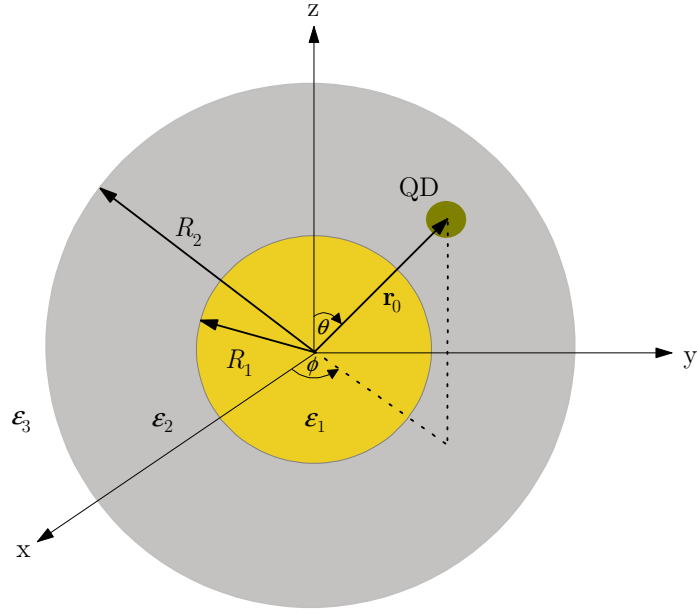


**Figure 3.1:** Spaser model under consideration:  $R_1$  is the nanosphere radius,  $R_2$  is the radius of the dielectric shell's outer boundary. A QD is located at the position  $\mathbf{r}_0$  with respect to the nanosphere's center. The parameters  $\epsilon_1, \epsilon_2$  and  $\epsilon_3$  denote the permittivities of the nanosphere, dielectric shell, and ambient, respectively.

the metal nanosphere is  $R_1$  and it is smaller than the skin depth of the metal, which is usually around 25 nm for noble metals [98]. The latter assumption is necessary to allow the localized SP modes to excite within the whole nanosphere as a coherent electron cloud oscillation. Further, we assume that  $R_1$  is greater than the nonlocality length, which is about 1 nm for noble metals, to avoid the effects of Landau damping [32, 42]. The outer radius of the shell ( $R_2$ ) must be chosen such that the shell thickness is large enough for the QD to be entirely embedded in the dielectric shell (i.e.  $R_2 - R_1 > \text{QD diameter}$ ).

When the nanosphere radius and the shell thickness are fixed, the resonator supports a series of SP modes (dipole, quadrupole, *etc.*) with unique energies [2, 95]. These SP modes may overlap with the QD in different degrees, hence experience the gain in different amounts as we have shown in Chapter 2. The SP mode receiv-

ing the highest gain survives and becomes the dominant spaser mode. The spasing mode receives gain as a result of the electronic transitions in the QD causing annihilation of high energy excitons. Therefore the population inversion of the two energy levels pertaining to these transitions becomes necessary, which is achieved by optical pumping.

### 3.2 SP Modes of the Nanosphere

To find the localized SP modes of the metal nanosphere, we assume that QD's presence does not significantly affect the electric field in the system because the QD is very small (*i.e.* about 1 nm in size) compared to the nanosphere so that the effective permittivity change in the dielectric shell is negligible. Although this trivial inhomogeneity can cause a very small shift of the mode frequencies of the plasmonic subsystem [99], the omission of this perturbation does not affect our study of this simple spherical spaser for design optimization.

We adopt a standard spherical coordinate system  $(r, \theta, \phi)$  where the origin coincides with the center of the spherical shell (see Fig. 3.1). The supported SP modes and relevant electric fields can be found by solving the vector Helmholtz equation for this geometry,  $(\nabla^2 + k^2)\mathbf{E}(\mathbf{r}, t) = 0$  where  $\mathbf{E}(\mathbf{r})$  is the electric field and  $k$  is the wavenumber. For this spherical geometry, the method of Debye potentials can be used to analytically solve the Helmholtz equation, which gives a series of modes denoted by the angular momentum number  $l = 1, 2, 3, \dots$  and its projection  $m = -l, -l + 1, \dots, 0, \dots, l$  as the solution [84, 97]:

$$\mathbf{E}(\mathbf{r}, t) = \sum_{l=1}^{\infty} \sum_{m=-l}^l \mathbf{E}_{lm}(\mathbf{r}) e^{i\omega_l t}, \quad (3.1)$$

where  $\omega_l$  is the angular frequency of the mode  $l$ . Due to the relation between  $l$  and  $m$  for the resonator's spherical geometry, SP mode  $l$  is  $2l + 1$  times degenerate. The solution also gives stationary electric field  $\mathbf{E}_{lm}(\mathbf{r})$  for each degenerate SP mode by

the expression:

$$\mathbf{E}_{lm}(\mathbf{r}) = \begin{cases} d_l \mathbf{N}_{lm}^{(1)} & \text{for } r \leq R_1, \\ g_l \mathbf{N}_{lm}^{(1)} + f_l \mathbf{N}_{lm}^{(2)} & \text{for } R_1 < r \leq R_2, \\ a_l \mathbf{N}_{lm}^{(3)} & \text{for } r > R_2, \end{cases} \quad (3.2)$$

where

$$\mathbf{N}_{lm}^{(\nu)} = (1/k) \nabla \times \nabla \times [\cos \phi P_l^m(\cos \theta) z_l^{(\nu)}(kr)], \quad (3.3)$$

$z_l^{(\nu)}(kr)$  is one of the spherical Bessel functions  $j_l(kr)$ ,  $y_l(kr)$ ,  $h_l(kr)$  in the standard notation for  $\nu = 1, 2, 3$  respectively,  $P_l^m$  are associated Legendre polynomials, and  $a_l$ ,  $d_l$ ,  $g_l$  and  $f_l$  are constants assuring the field's continuity at boundaries.

### 3.2.1 SP Energies

The SP modes expressed by Eq. (3.1) possess a unique energy determined by  $\hbar\omega_l$ . To find  $\omega_l$ , we first write a set of equations expressing the constants  $a_l$ ,  $d_l$ ,  $g_l$  and  $f_l$  in Eq. (3.2) by equating the tangential components of the field at the metal-dielectric and dielectric-ambient interfaces. This results in a homogeneous system of linear equations in which the condition for a nontrivial solution is applied and the following relation for the  $l$ th mode SP resonance is obtained:

$$m_1 [s_1(k_3 q_2 - k_2 q_3) - q_1(k_3 s_2 - k_2 s_3)] = k_1 [s_1(m_3 q_2 - m_2 q_3) - q_1(m_3 s_2 - m_2 s_3)] \quad (3.4)$$

where,

$$\begin{aligned} q_1 &= \sqrt{\varepsilon_2} \psi'_l(k_m R_1) & q_2 &= -\sqrt{\varepsilon_1} \psi'_l(k_d R_1) & q_3 &= \sqrt{\varepsilon_1} \chi'_l(k_d R_1), \\ s_1 &= -\psi_l(k_m R_1) & s_2 &= \psi_l(k_d R_1) & s_3 &= -\chi_l(k_d R_1), \\ k_1 &= \sqrt{\varepsilon_2} \xi'_l(k_0 R_2) & k_2 &= -\psi'_l(k_d R_2) & k_3 &= \chi'_l(k_d R_2), \\ m_1 &= \xi_l(k_0 R_2) & m_2 &= -\psi_l(k_d R_2) & m_3 &= \chi_l(k_d R_2), \end{aligned}$$

$\psi_l(x) = x j_l(x)$ ,  $\xi_l(x) = x h_l^{(1)}(x)$  and  $\chi_l(x) = -x y_l(x)$  are the Reccati-Bessel functions in standard notation and  $k_m$ ,  $k_d$ , and  $k_0$  are the wavenumbers of the

electromagnetic field in the metal, dielectric, and ambient, respectively. According to Eq. (8.2), the energy of a SP ( $\hbar\omega_l$ ) is a function of  $R_1$ ,  $R_2$ ,  $\varepsilon_1$ ,  $\varepsilon_2$ , and  $\varepsilon_3$ , which implies that the geometric parameters of the resonator determine the energy of the SP modes when the spaser materials are chosen.

Furthermore, this nontrivial solution of the boundary conditions allows us to express the coefficients  $a_l$ ,  $d_l$ ,  $g_l$  in terms of  $f_l$  as

$$a_l = \frac{s_1(k_2q_3 - k_3q_2) - q_1(k_2s_3 - k_3s_2)}{k_1(q_2s_1 - q_1s_2)} f_l, \quad (3.5)$$

$$d_l = \frac{q_3s_2 - q_2s_3}{q_2s_1 - q_1s_2} f_l, \quad (3.6)$$

$$g_l = \frac{q_1s_3 - q_3s_1}{q_2s_1 - q_1s_2} f_l. \quad (3.7)$$

To find an expression for  $f_l$  as a normalization constant, we follow the procedure of secondary quantization for dispersive media as described in Section 2.1.0.1, and equate the total energy of the electric field of a SP to  $\hbar\omega_l$ :

$$\int_V \frac{1}{2} \frac{\partial}{\partial \omega} (\omega \varepsilon(\omega)) |\mathbf{E}_{lm}(\mathbf{r})|^2 d\mathbf{r} = \hbar\omega_l, \quad (3.8)$$

where  $V$  implies the volume integral over three dimensional Euclidean space.

### 3.3 QD Gain Element

Properties of the gain medium determine the nature of the exciton–SP interactions of a spaser and the amount of amplification that each SP mode receives. We have chosen a QD as the gain element in this spaser design as they are widely used in many lasing setups [57–61]. As the charge carriers in a QD are confined in all three dimensions to a very small size, its density of states (DOS) almost resembles a set of delta functions, mimicking an atomistic behavior with a well defined spectral response [60, 62, 63]. They also promise a better stability over temperature variations [61]. The decisive characteristics of a QD are its wavefunction and the energy levels of the excitons. Electronic transitions between these levels fuel

spacing and, as in the case of lasers, those transitions representing annihilation of excitons would excite the SPs in the nanosphere by stimulated emission.

According to the general model discussed in Chapter 2, an excitable QD like this can be effectively described by three energy levels to account for pumping and stimulated transitions. We denote the ground level of the QD by the state vector  $|0e\rangle$  and two excited levels by  $|1e\rangle$  and  $|2e\rangle$ . To assign energies to these three levels, the quantum confinement effects of the QD are taken into account. Although a QD can have any geometry, for the sake of simplicity, we assume that the QD is spherical with a radius  $R_q$ , confined by an infinite potential barrier (i.e. potential  $V(r) = 0$  for  $r < R_q$  and it is infinite otherwise). The resulting time-independent Schrodinger equation is separable in spherical coordinates and possesses a solution similar to the hydrogen atom and given by [100],

$$\psi_{n_q, l_q, m_q}(r, \theta, \phi) = \sqrt{\frac{2}{R_q^3} \frac{j_{l_q}(\xi_{n_q l_q} r/R_q)}{j_{(l_q+1)}(\xi_{n_q l_q})}} Y_{l_q}^{m_q}(\theta, \phi), \quad (3.9)$$

where  $n_q, l_q, m_q$  are principal, azimuthal and magnetic quantum numbers describing the states,  $\xi_{n_q l_q}$  is the  $n_q$ th root of the spherical Bessel function of the first kind (i.e.  $j(\xi_{n_q l_q}) = 0$ ), and  $Y_{l_q}^{m_q}$  are spherical harmonics.

The corresponding eigenvalues of the wave function  $\psi_{n_q, l_q, m_q}(r, \theta, \phi)$  give the excitable energy levels of an exciton:

$$E_{n_q, l_q} = E_g + \frac{\hbar^2}{2\mu R_q^2} \xi_{n_q, l_q}^2, \quad (3.10)$$

where  $\mu = m_e^* m_h^* / (m_e^* + m_h^*)$  is the reduced mass of an exciton,  $m_e^*$  and  $m_h^*$  are effective masses of an electron and a hole, and  $E_g$  is the bandgap of the QD material. The energy levels denoted by  $E_{n_q, l_q}$  are  $2l_q + 1$  times degenerate. For a transition from an initial state  $|i\rangle$  with quantum numbers  $s_i = (n_i, l_i, m_i)$  to a final state  $|f\rangle$  with quantum numbers  $s_f = (n_f, l_f, m_f)$ , the absorbed energy from the system will be  $\Delta E_{f,i} = E_{n_f, l_f} - E_{n_i, l_i}$ . Energy is released in case this quantity is negative.

Having this knowledge, we map the energy levels in Eq. (3.10) to three QD energy levels. The state  $|0e\rangle$  is mapped to the energy zero ground level and for

the states  $|1e\rangle$  and  $|2e\rangle$  we chose the next two lowest energy levels:  $(n_q, l_q) = (1,0)$  and  $(1,1)$ , assuming that probability of populating even higher energy levels is very small. This mapping allows us to calculate the QD radius  $R_q$  required for a resonant energy transfer to the resonator, where the energy of the spaser mode  $\hbar\omega_l$  equals to the energy released by the QD transition  $|1e\rangle \rightarrow |0e\rangle$ , *i.e.*  $\Delta E_{0e,1e}$  giving

$$R_q = \frac{\hbar\xi_{n_i l_i}}{\sqrt{2\mu(\hbar\omega_l - E_g)}}. \quad (3.11)$$

Although achieving perfectly matched resonance may be difficult in practice, having a closer value to the quantity in Eq. (3.11) is adequate for spasing [28].

### 3.4 Applying the General Model for a Dipole Mode Spaser and Design Optimization

Let us consider a case of a gold nanosphere-QD spaser where the dipole mode ( $l = 1$ ) of the gold nanosphere is resonantly coupled to the QD gain element as shown in Fig. 3.1. The experimental realisation of this design can be achieved within a few steps of nanofabrication. The gold nanosphere can be synthesised by coagulation of colloidal gold and a silica ( $\text{SiO}_2$ ) coating can be used to embed a CdSe QD according to the techniques described in Refs. [101] and [102]. The radius and shell thickness of such particles can be easily controlled by chemical means [18, 103, 104].

As the optical properties, a non-dispersive permittivity  $\varepsilon_2 = 2.15$  is assumed for silica in contrast to gold which shows a frequency dependent dielectric properties. The spaser's outer boundary is assumed to be in free space, hence  $\varepsilon_3 = 1$ . Since this gold nanosphere is very small, it is required to consider the size dependency modification to the permittivity given by [105, 106],

$$\varepsilon_1(\omega, R_1) = \varepsilon_\infty - \frac{\omega_p^2}{\omega^2 + i\omega\Gamma(R_1)}, \quad (3.12)$$

where  $\omega_p$  is the bulk plasma frequency of gold,  $\Gamma$  is the electron collision frequency with damping defined by  $\Gamma = \gamma_b + (v_F/2R_1)$ ,  $\gamma_b$  is the bulk electron collision

frequency of gold,  $v_F$  is the Fermi velocity, and  $\varepsilon_\infty$  is the contribution from the interband transitions obtained by fitting  $\varepsilon_1(\omega, R_1)|_{R_1 \rightarrow \infty}$  to the experimental data published by Johnson and Christy [107] for bulk material. We also assume the realistic values  $\omega_p = 1.36 \times 10^{16} \text{ s}^{-1}$ ,  $\gamma_b = 3.33 \times 10^{13} \text{ s}^{-1}$ ,  $v_F = 1.4 \times 10^6 \text{ m/s}$ , and  $\varepsilon_\infty = 9.84$  in the solutions derived in Section 3.2 [106, 108].

### 3.4.1 Spaser Mode Energy

The knowledge of permittivities of the spaser materials helps to solve Eq. (8.2) for  $l = 1$  and find the spaser mode energy  $\hbar\omega_1$ . Because the wavenumber  $k = \omega/c = \omega\sqrt{\mu\varepsilon} \simeq \omega\sqrt{\varepsilon}$  (we assume permeability  $\mu = 1$ ), all the terms in this equation ( $q_1, q_2, \dots, \text{etc.}$ ) can be given in the terms of  $\omega_1$ ,  $R_1$ ,  $R_2$ ,  $\varepsilon_1(\omega_1, R_1)$ ,  $\varepsilon_2$ , and  $\varepsilon_3$ . Therefore,  $\omega_1$  becomes a function of  $R_1$  and  $R_2$  when the permittivities are known. However the presence of Reccati-Bessel functions in each term and the complexity of the equation make an analytical solution unattainable. Therefore we solve Eq. (8.2) numerically and plot the spaser mode energy with respect to the nanosphere radius  $R_1$  and shell thickness  $t_{shell} = R_2 - R_1$  as shown in Fig. 3.2.

The contour plot shows that there exist many  $(R_1, t_{shell})$  pairs which can give the same spaser mode energy. For example, if the spaser mode energy is 2.385 eV (i.e. equivalent wavelength is approximately 520 nm), it traces a curve on the contour plot as marked showing the  $(R_1, t_{shell})$  values which can be used to make a spaser resonator having the dipole mode energy of 2.385 eV.

### 3.4.2 Quantum States of the Spaser

The dipole SP mode of the spherical resonator is triply degenerate with  $(l, m) = (1, -1), (1, 0), (1, 1)$  and therefore the states of the spaser's plasmonic subsystem are the SP states  $|1p^{(1,-1)}\rangle$ ,  $|1p^{(1,0)}\rangle$ ,  $|1p^{(1,1)}\rangle$ , and the ground state  $|0p\rangle$ . When the spaser mode energy is known, appropriate QD radius ( $R_q$ ) for resonant coupling can

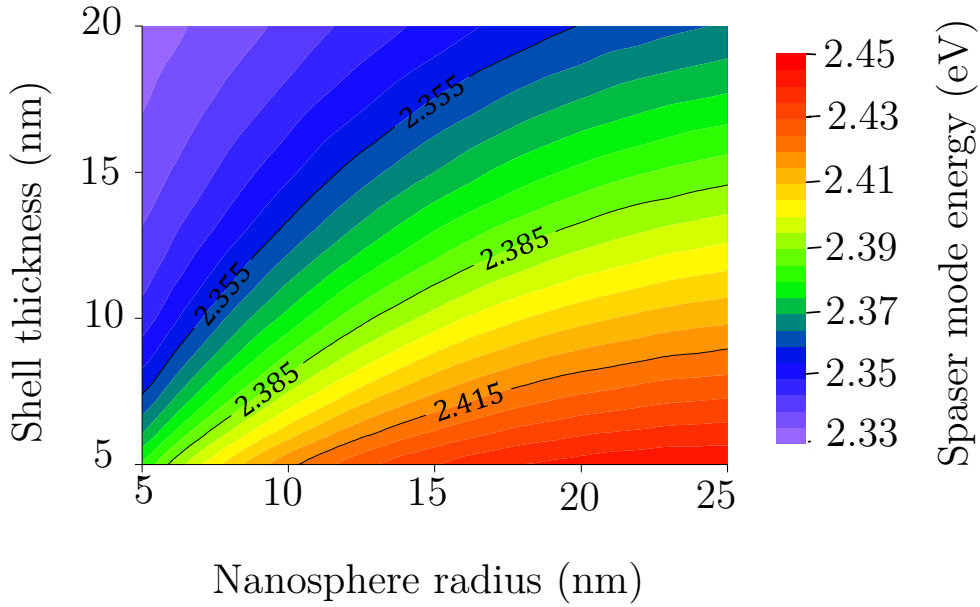


**Figure 3.2:** Energy of the spaser mode as a function of the nanosphere radius  $R_1$  and the shell thickness  $t_{shell} = R_2 - R_1$ .

be found using Eq. (3.11). For the previously set operating point ( $\hbar\omega_1 = 2.385$  eV), the substitution gives resonant QD radius to be 2.4 nm, for the assumed parameters  $E_g = 1.74$  eV,  $m_e^* = 0.13$ , and  $m_h^* = 0.45$  for a spherical CdSe QD [109, 110]. Using these parameters and  $R_q = 2.4$  nm in Eq. (3.10) gives the three lowest energy levels for QD: 0, 2.385, and 3.059 eV, assigned to the states of the electronic subsystem  $|0e\rangle$ ,  $|1e\rangle$ , and  $|2e\rangle$ , respectively. Hence, according to the general model developed in Section 2.2.3, the total system of the dipole spaser consists of essential six states as shown in Fig. 3.3:

$$\begin{aligned}
 |1\rangle &= |0e\rangle |0p\rangle & |2\rangle &= |1e\rangle |0p\rangle & |3\rangle &= |2e\rangle |0p\rangle \\
 |4\rangle &= |0e\rangle |1p^{1,-1}\rangle & |5\rangle &= |0e\rangle |1p^{1,0}\rangle & |6\rangle &= |0e\rangle |1p^{1,1}\rangle
 \end{aligned} \tag{3.13}$$

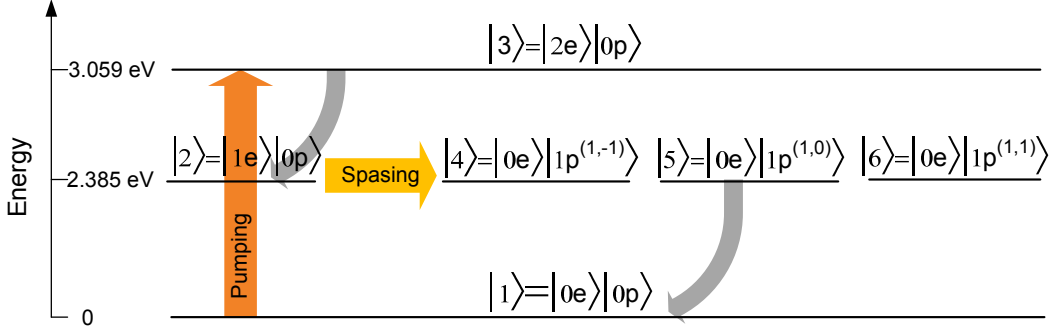


**Figure 3.3:** Product states of the dipole spaser.

### 3.4.3 SP Generation Rate

Although Fig. 3.2 shows that there are many  $R_1, t_{shell}$  values that one can choose for a known spaser mode energy, just opting for an arbitrary  $(R_1, t_{shell})$  pair on the preferred spaser mode energy curve (*e.g.* 2.385 eV) may not result in the highest SP generation. Therefore it is necessary to find the SP generation rate for this dipole spaser by analysing its 6-state system in order to find the optimum design parameters.

As shown earlier in Section 2.3.2, the total SP generation rate of this dipole spaser can be given by the sum of the populations of the states  $|4\rangle$ ,  $|5\rangle$ , and  $|6\rangle$ :  $\mathcal{R}_1 = \rho_{44} + \rho_{55} + \rho_{66}$ . This quantity can be evaluated using the expression for  $\mathcal{R}_l$  given in Eq. (2.16),

$$\mathcal{R}_1 = \frac{\xi_{23}\omega_1^2}{2\varepsilon_2\hbar\gamma_{13}\gamma_{22}\gamma_{33}\gamma_p} \frac{\gamma_{2p}}{\gamma_{2p}^2 + \Delta_{2p}^2} |V_{2e,0e}|^2 \sum_{j=4}^6 |V_{1e,0e}^{1,j-5}|^2. \quad (3.14)$$

The relaxation constants,  $\gamma_{13}$ ,  $\gamma_{22}$ ,  $\gamma_{33}$ ,  $\gamma_{2p}$ , and  $\xi_{23}$ , depend on the environment and used materials, but not on the spaser geometry. As the materials have already been chosen, we can keep them constant and compare the normalized SP generation rate as our goal is to find the optimum geometrical parameters result in maximum SP populations. The only rate constant influenced by spaser's geometry is the decay

rate of SPs  $\gamma_p$ , which is a function of the spaser mode energy and given by [17]

$$\gamma_{pl} \simeq \frac{\text{Im}[\varepsilon_1(\omega)]}{\frac{\partial}{\partial \omega} \text{Re}[\varepsilon_1(\omega)]} \Big|_{\omega=\omega_1}. \quad (3.15)$$

By substituting the model for nanosphere's permittivity given in Eq. (3.12), this can be simplified to:

$$\gamma_p \simeq \frac{\Gamma}{2} [1 + (\Gamma/\omega_1)^2]. \quad (3.16)$$

Since both the quantities  $\Gamma$  and  $\omega_1$  depend on  $R_1$  and  $R_2$ ,  $\gamma_p$  also depends on them for a given material.

Other required quantities to calculate the SP generation rate are the matrix elements  $V_{2e,0e}$  for pump light–exciton interactions and  $V_{1e,0e}^{1,-1}$ ,  $V_{1e,0e}^{1,0}$ ,  $V_{1e,0e}^{1,1}$  for exciton–SP interactions. As pump light is a controllable parameter at operation we keep  $V_{2e,0e}$  constant when optimizing the design parameters. However it is necessary to compare the threshold gain requirement from the pump, which we consider later. The expression for  $V_{i,f}^{l,m}$  is given in Eq. (2.13):

$$V_{f,i}^{l,m} = \frac{\sqrt{2}P}{E_g} \int_V \psi_f^*(\mathbf{r}) E_{lm}(\mathbf{r}) \psi_i(\mathbf{r}) \, d\mathbf{r}, \quad (3.17)$$

This integral is numerically evaluated using the QD's wavefunction given in Eqn. (3.9) for  $\psi_f^*(\mathbf{r})$ , and  $\psi_i(\mathbf{r})$ , and the expression for the electric field  $E_{lm}$  from Eqn. (3.2).

### 3.4.3.1 Optimum $R_1$ and $R_2$

First, we plot the SP generation rate,  $\mathcal{R}_1$  of the dipole spaser with respect to nanosphere radius and shell thickness as shown in Fig. 3.2, when the QD's location is fixed to the middle of the dielectric shell and  $R_q$  is fixed to the resonant radius given by Eq. (3.11). From the figure, it can be noted that SP generation rate is higher for smaller nanosphere radii and shell thicknesses. It monotonically decreases when the total volume is increased.

Let us continue with the previous example (see Fig. 3.2) and draw the curve corresponds to the spaser mode energy 2.385 eV on Fig. 3.4. Based on this curve, it

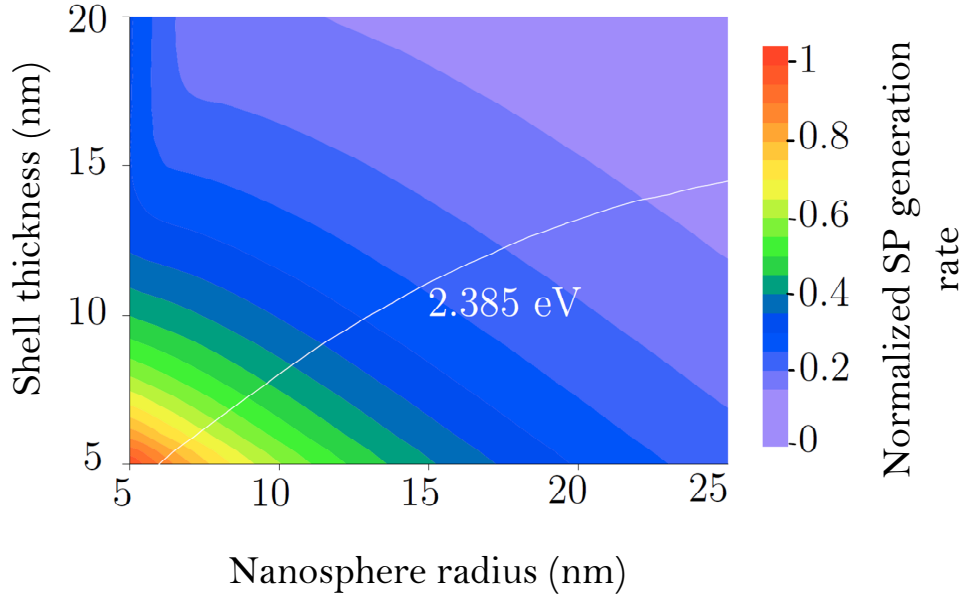


**Figure 3.4:** Normalized SP generation rate is plotted with respect to nanosphere radius  $R_1$  and shell thickness  $t_{shell}$  when the QD's location is fixed to the middle of the dielectric shell. The drawn curve corresponds to the spaser mode energy 2.385 eV.

is observed that the SP generation rate varies with geometric parameters, even for the same spaser mode energy. Hence, we may select parameters for the optimum design by picking the  $(R_1, R_2)$  pair which results in the highest SP generation rate. In our example, parameters  $(R_1, R_2) = (6 \text{ nm}, 11 \text{ nm})$  offer the highest spaser mode amplification for the 2.385 eV energy curve. Here we emphasize that, although this result is obtained for a single QD dipole spaser, another spaser configuration may consists of many QDs to achieve a higher gain. If this dipole spaser consists of  $N$  QDs, then  $N \propto (R_2^3 - R_1^3)/R_q^3$  if the QDs are uniformly distributed inside the dielectric shell. In that case, having a bigger shell volume to accommodate more QDs may result in a higher SP generation because all QDs contribute to the total amplification. However, each QD does not contribute equally in many QDs case as the location of the QD and its size play vital roles in deciding the SP generation rate.

### 3.4.3.2 QD Placement and Size

In order to examine how the location of the QD affects the SP generation rate of the spaser, we fix  $R_1$  and  $R_2$ , and plot  $\mathcal{R}_1$  for the case of resonant QD radius (i.e.  $R_q$  is also fixed) in Fig. 3.5. Here QD's location  $r_0$  is varied within the dielectric shell from the innermost to the outermost position with respect to the nanosphere's center. Such plots for four different  $(R_1, R_2)$  pairs are shown in Fig. 3.5. It can be observed from these plots that the SP generation rapidly decreases when the QD is moved away from the nanosphere. This happens because the interactions between SPs and excitons get weaker towards the shell's outer boundary as the matrix element for interactions ( $V_{1e,0e}^{l,m}$ ) decreases in the radial direction according to Eqs. (3.2) and (3.17). The decreasing rate is higher for smaller nanosphere radii. Especially, when there are many QDs, their contribution to the spasing mode will not be uniform. Hence, when designing a multiple QD spaser, we must set the optimum size parameters such that a large number of QDs are closely located to the nanosphere center.

Thus far, we have only considered the case where the QD radius is tuned according to Eq. (3.11) such that its emission energy exactly equals to the energy of the spaser mode. However, achieving the exact resonance may be difficult in practice. To investigate the influence of matching the QD radius on spasing, we vary  $R_q$  within an interval of 1-3 nm and plot the SP generation rate, as shown in Fig. 3.6 for different shell thicknesses keeping the nanosphere radius fixed to 10 nm. According to this plot, highest SP generation is observable in the case of exact resonance and it rapidly decreases when the  $R_q$  deviates from the resonant QD radius. For example, if the the QD radius deviates about 0.5 nm from the resonant value, the resultant plasmon excitation rate will tend to zero.

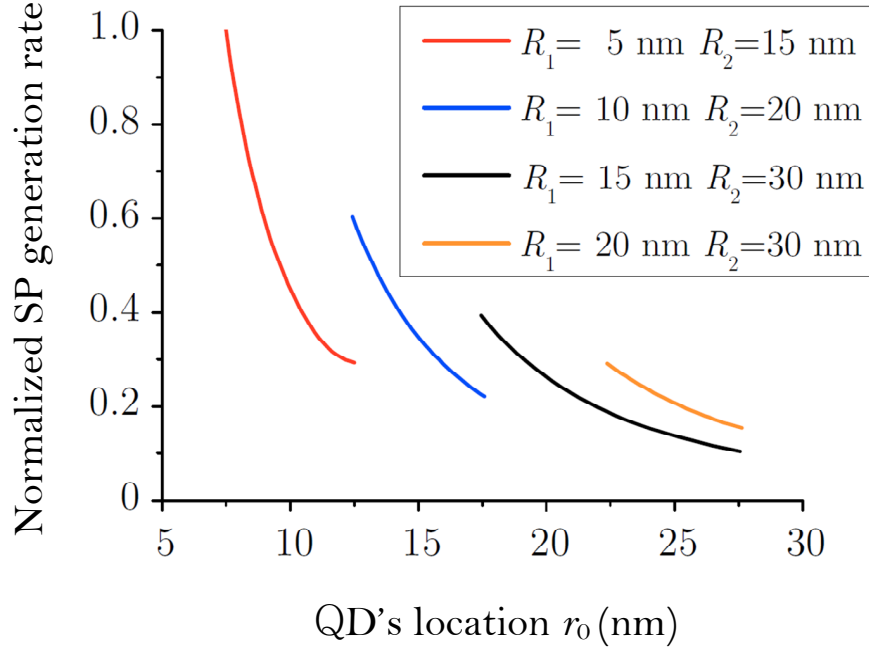


**Figure 3.5:** Plot of SP generation rate with respect to the QD's location  $r_0$  for different  $R_1, R_2$  pairs.

### 3.4.4 Threshold Gain

The plots in Figs. 3.4, 3.5, and 3.6, clearly illustrate how the geometrical parameters of spaser design can be optimized to attain an elevated SP generation rate. In addition, we need to discuss the threshold power required from optical pumping which is a condition of spasing. This threshold power gain, which does not depend on spaser geometry, is a function of the dielectric constants of the spaser components and the spaser mode energy given by [17],

$$g_{th} = \frac{\omega_l}{c\sqrt{\varepsilon_2}} \frac{\text{Im}\varepsilon_1(\omega_l)}{\left[\text{Re}\left(\frac{\varepsilon_2}{\varepsilon_2 - \varepsilon_1(\omega_l)}\right)\right]^{-1} - 1}. \quad (3.18)$$

However, the geometrical parameters of the spaser design indirectly affect the threshold gain as the spaser mode energy is a function of them. Hence  $g_{th}$  also becomes a function of the nanosphere radius and shell thickness as plotted in Fig. 3.7. According to this plot, the gain does not vary much with the size parameters but

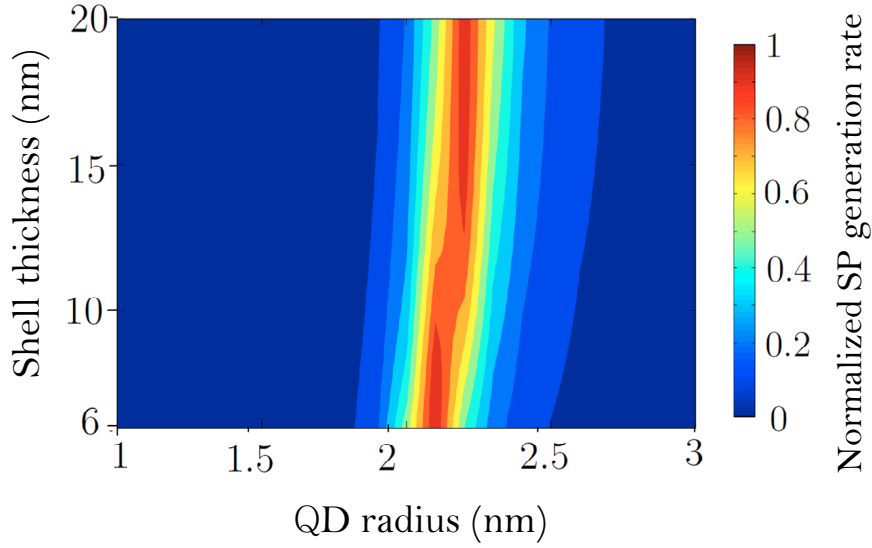


**Figure 3.6:** The normalized SP generation rate is plotted with respect to the QD radius and the shell thickness when the nanosphere radius is fixed to 10 nm and the QD’s location is fixed to the middle of the dielectric shell.

the required threshold pump power for spasing is little higher when the nanosphere is smaller. This might be because the influence of nanosphere radius and  $\omega_l$  on the metal’s permittivity whereas the influence of the shell thickness comes only through  $\omega_l$ . We mark the 2.385 eV curve, which was used in the previous example, on threshold pump power plot and it gives an idea of choosing the optimal geometrical parameters.

The case study performed throughout this chapter can be used to develop clear design guidelines on choosing the optimum size parameters of the spaser components and QD placement to achieve a maximum SP generation rate. In the process of designing a spaser with this particular geometry, one might choose its operating wavelength as the first step, then pick possible values for the size parameters  $R_1$ ,  $R_2$  and  $R_q$  by examining the resulting in SP generation rate. Then, it is necessary to figure out where to embed the QD. Although placing the QD closer to the nanosphere would give a higher SP generation rate, the one need

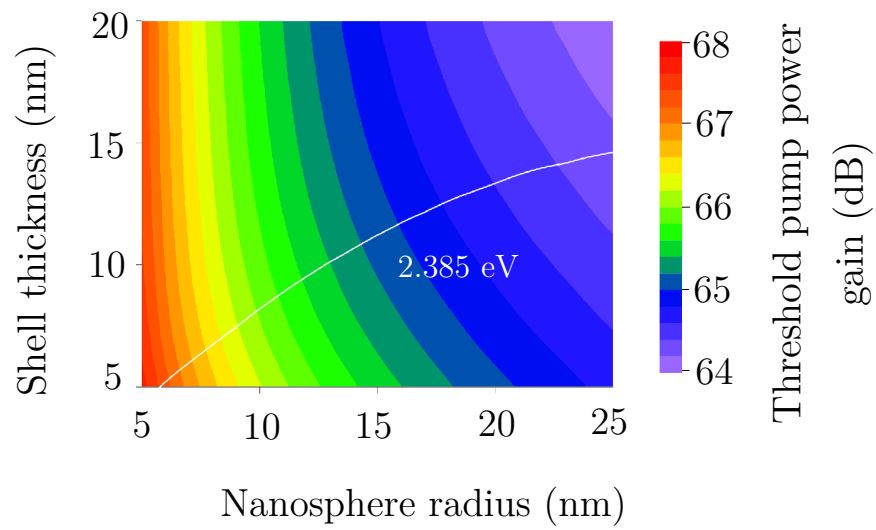


**Figure 3.7:** Threshold gain required by pumping with respect to nanosphere radius and shell thickness.

to consider about the precise placement if multiple QDs are to be taken because not all QDs can be placed close to the nanosphere's boundary.

## Chapter 4

# Spaser Materials and Potential of Carbon

The analyses done in Chapters 2 and 3 suggest that the operating characteristics of a spaser highly depend on its geometry and the used materials. Particularly in Chapter 3, we sought the optimization methods for a nanosphere–QD spaser design by tuning certain geometric parameters when the materials are chosen. In this chapter we study on different materials can be used for different spaser components and show that carbon based materials such as graphene and CNTs can be effectively used in spaser designs.

Many designs have been proposed for spasers since its theoretical formulation. These include a sandwiched gold-film plasmonic waveguide between optically pumped quantum wells [39], a V-shaped metal nanoparticle surrounded by quantum dots (QDs) [28], an array of split-ring shape resonators placed on an active substrate[30], a bowtie shaped metallic structure with bound QDs [31], and a metal nanogroove with QDs placed at its bottom [29]. The common attribute of all these designs is all of them use noble metals for the plasmonic resonator and quantum dots/wells or dyes for the gain medium.

## 4.1 Commonly Used Spaser Materials

### 4.1.1 Noble Metals

Although any metal nanoparticle placed in a dielectric ambient may undergo localized surface plasmon resonance and support SP modes, noble metals (especially silver and gold) are unique because their resonances fall within visible light or infrared frequencies and showing high absorption compared to alkali metals [25]. Applications of the resonant absorption and scattering effects of noble metals have a long history of hundreds of years from when gold and silver were used for glass staining for windows or ornamental cups giving bright colours. Although other noble metals such as Cu, Pd, Al, and Pt also have resonance frequencies in visible or IR regimes, they show weak absorption properties and face problems like surface oxides [1, 25]. This is the reason why most spaser designs have a gold or silver nanoparticles as plasmonic resonators. They provide the luxury of tuning the spaser mode energy of the design by altering the shape or changing size parameters as we have seen in Section 3.4.1.

### 4.1.2 Quantum Dots/Wells

Similarly, there are few choices for the spaser gain medium. The semiconductor QDs are the most popular among them and the first proposed spaser design also had QDs in the gain medium [28]. The size of a QD could be as small as a nanometer and as the charge carriers in a QD are confined in all three dimensions to this small size, its density of states (DOS) plot becomes a set of delta functions, very much similar to an atom [60, 62, 63]. They also promise a good stability over temperature variations [61]. Quantum wells (QWs) also show distinct energy levels similar to QDs but the carriers are confined only in two dimensions [111]. The used materials to fabricate QDs and QWs include CdSe, GaAs, InP, and many other semiconductor materials [7–9].

### 4.1.3 Florescent Dyes and Rare Earth Ions

Florescent dyes and rare earth ions are another two types of materials used in some laser gain media and can be used for spasers as well. In addition, dyes (or chromophores), which are fluorescent chemical compounds, can get excited by absorbing light and emit in a different wavelength, are also used. For example, the first experimentally demonstrated spaser had OG-488 dye molecules in the gain medium [18]. Rare earth ions are the charged particles (*e.g.*  $\text{Er}^{3+}$ ,  $\text{Yb}^{3+}$ , and  $\text{Nd}^{3+}$ ) having the same capability [24]. All these gain elements can be conveniently used in a spaser gain medium and regarded as a three level system in analysis [18, 24, 42].

## 4.2 Carbon Allotropes

Carbon has revolutionized nanotechnology research with the invention of its new allotropes graphene, carbon nanotubes (CNTs), and fullerenes [112, 113]. Many research have been carried out to replace conventional semiconductor materials with these materials due to their remarkable electrical, mechanical, and thermal properties. It has been found that graphene is a much better conductor than silver [71, 113]. Importantly, it has also been shown that graphene support SP excitations which exhibit better confinement, low dissipation and highly tunable characteristics compared to noble metal SPs. Therefore it is also a platform for strong light-matter interactions [72, 73]. Hence, graphene becomes an excellent substitution for a spaser cavity [114]. Similarly, semiconducting CNTs are well known for forming excitons by electromagnetic absorption and consequent photoluminescence [71, 74, 75]. The absorption and emission characteristics can be tuned by changing the diameter or chirality of the CNT [76, 77]. These optical properties similar to QDs and dye molecules suggest that CNTs can also be used as a spaser gain medium. Therefore in the following sections, we investigate these properties of graphene and CNTs in detail in order to design an all-carbon spaser.

### 4.3 Surface Plasmons in Graphene

Many recent theoretical [73, 115, 116] and experimental [117–119] studies suggest that graphene possesses much better plasmonic properties in terms of tunability, field confinement and low resistive losses compared to noble metals. Carriers in graphene behave as massless Dirac fermions (MDFs) due to their well known conical band structure [72, 73, 118]. Due to high carrier concentration and mobility, graphene plasmons can travel much longer distances compared to noble metal plasmons [72, 120]. Plasmonic properties of 2-dimensional graphene can be derived from its frequency dependent optical conductivity:

$$\sigma(\omega) = \sigma_{intra}(\omega) + \sigma_{inter}(\omega), \quad (4.1)$$

representing the contributions by interband and intraband carrier transitions. Following the random phase approximation (RPA) and semiclassical Drude model with finite temperature correction, intraband conductivity of 2-dimensional graphene can be given by [120, 121]

$$\sigma_{intra}(\omega) = \frac{e_c^2 E_F}{\pi \hbar^2} \frac{i 2 k_B T}{\omega + i \tau^{-1}} \ln \left[ 2 \cosh \left( \frac{E_F}{2 k_B T} \right) \right] \quad (4.2)$$

where  $E_F$  is the Fermi level,  $e_c$  is the charge of an electron,  $\omega$  is the angular frequency,  $\tau$  is the finite relaxation time,  $k_B$  is the Boltzmann's constant and  $T$  is the temperature. However, at room temperature and within the Fermi levels of interest,  $E_F/2k_B T \gg 1$  making  $\cosh(E_F/2k_B T) \approx (1/2)e^{\frac{E_F}{2k_B T}}$  giving

$$\sigma_{intra}(\omega) \approx \frac{e_c^2 E_F}{\pi \hbar^2} \frac{i}{\omega + i \tau^{-1}}. \quad (4.3)$$

The interband contribution:

$$\sigma_{inter}(\omega) = \frac{e_c^2}{4 \hbar} \left[ f(\hbar \omega - 2 E_F) + \frac{i}{\pi} \ln \left| \frac{\hbar \omega - 2 E_F}{\hbar \omega + 2 E_F} \right| \right], \quad (4.4)$$

where  $f$  is the Fermi-Dirac distribution function. It is assumed that the interband contribution to the conductivity is negligible for low energies but it becomes much significant for high energies such as visible light.

Since  $E_F$  can be controlled by either doping or electrostatic gating, the conductivity of graphene is highly tunable, even allowing dynamic controlling. Therefore many applications based on graphene SPs have been proposed including waveguide and plasmonic switches [72, 73, 122]. Therefore, here we examine how graphene can be effectively used in the plasmonic resonator of a spaser.

### 4.3.1 Graphene Plasmonic Resonators

Plasmonic resonator of a spaser should have a confined geometry so that localized SP oscillations are allowed. Graphene is a 2-dimensional sheet of carbon atoms having a honeycomb lattice structure, with carbon atoms being in  $sp^2$  hybridization. We can cut a preferred 2D shape from a graphene sheet as shown in Fig. 4.1. Such a shape could be called a graphene nanoflake (GNF) and prepared using common nanofabrication technologies such as chemical vapor deposition (CVD), micromechanical cleavage, graphite oxide exfoliation, or epitaxial growth on a substrate [123, 124]. When finding the SP modes supported by such a GNF, first we use the expression for  $\sigma(\omega)$  in Eq. (4.1) to derive the permittivity of graphene:

$$\varepsilon(\omega) = 1 + \frac{\sigma(\omega)}{\varepsilon_0\omega} \quad (4.5)$$

where  $\varepsilon_0$  is the permittivity of free space [125]. Although the Eqs. (4.2–4.4) are derived for an infinitely wide graphene sheet, these expressions provide a reasonably accurate estimate for sufficiently wide GNFs exceeding at least 50 atoms (*i.e.* about 5 nm) in both dimensions [73]. In much narrower graphene sheets, the conductivity may be affected by extreme carrier confinement. Therefore, the dimensions of the cavity geometry can be carefully chosen well above this limit to avoid those effects.

#### 4.3.1.1 SP Modes of a Square Shaped GNF

A GNF may take any geometry, such as rectangular, circular, or hexagonal shape. Depending on the confinement geometry and dielectric properties, it possesses a unique set of eigenfrequencies describing the supported SP modes [42].

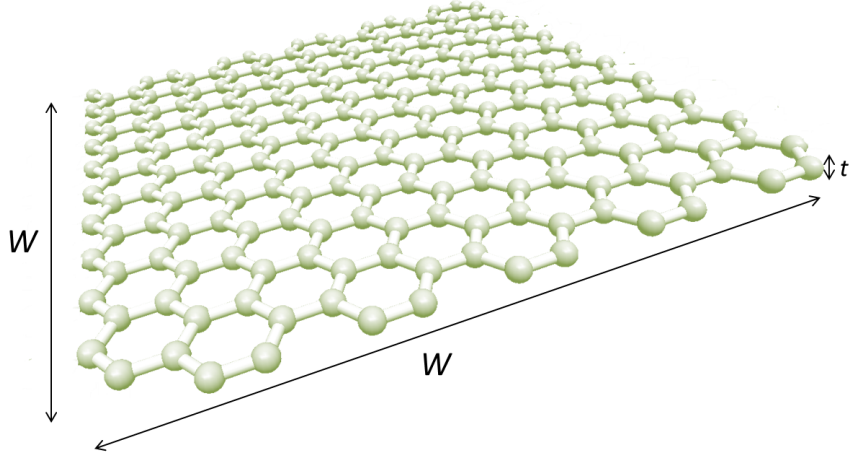


**Figure 4.1:** A square shaped  $W$  wide GNF cut from a graphene sheet

In this chapter the SP modes of square shape GNF are studied considering the fabrication ability with high precision and the convenience in analysis. Although any rectangular graphene flake is easily preparable, without loss of generality, the case of square is considered where only one geometric parameter comes into equations. For a given width  $W$ , the square shaped GNF resonator supports a series of localized SP modes with unique energies.

As shown in Chapter 2, SPs localized on a spaser resonator can be represented by two quantum numbers  $(l, m)$  representing the mode number and degeneracy number. The eigenfrequencies of the localized SP modes on a GNF and respective degeneracies are found by solving the Helmholtz equation  $(\nabla^2 + k^2)\mathbf{E}(\mathbf{r}) = 0$  for the considered  $W \times W$  square geometry. This equation can be solved numerically for any geometry using the finite element method [126]. In order to do attain this numerical solution, the GNF is assigned a finite thickness of  $t = 0.5$  nm as shown in Fig. 4.1, which is the most common numerical modelling technique for graphene and it has been shown that this value does not affect the solution significantly [73, 116, 120]. This modification allows us to model graphene as a three dimensional structure with very small thickness and the modified conductivity is given

by  $\sigma(\omega)/t$ .

Normalized electric field  $\mathbf{E}_{lm}(\mathbf{r})$  of the first five (lowest energy) SP modes supported by a  $W$  wide GNF are shown in Fig. 4.2(a). These modes can be indexed as  $l=1, 2, 3, \dots$ , following the order of increasing SP energy. It is seen that only some SP modes such as 2, 4 and 5 exhibit degeneracy unlike the spherical resonator we studied in Chapter 3 where the degeneracy number is directly related to the mode number. Although the shown 2, 4 and 5 modes are doubly degenerate, higher order modes may show higher degeneracy numbers which can be found only by observing the eigenfrequency solutions.

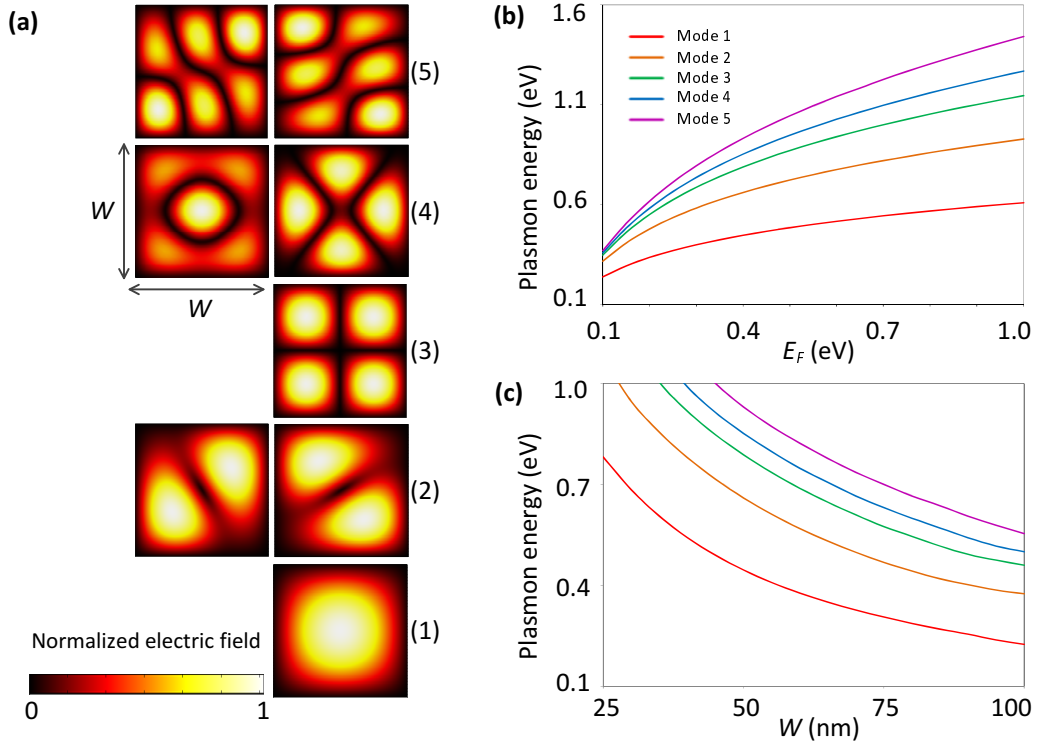


**Figure 4.2:** (a) Normalized electric field distributions of the five lowest-energy modes supported by a square GNF of width  $W$ . The mode energies are plotted as functions of (b) Fermi energy for  $W = 50$  nm and (c) GNF width for  $E_F = 0.4$  eV (the color legend applies to both the plots).

The tunability of SP energies of a GNF with respect to  $E_F$  and  $W$  is illustrated in Figures 4.2(b) and 4.2(c). According to the plots, SP energies span over a wide range over the mid and near infrared regimes offering a tremendous freedom of choice. Since  $E_F$  can be changed by either doping or gating, SP energies are tunable with respect to both the geometric and material parameters. One outstanding advantage of graphene is even the dynamic tuning of a device by electrostatic gating is possible while operation. Our results are validated as the trends in these plots follow the proven relations for one dimensionally confined  $W_r$  wide graphene nanoribbons having SP energies proportional to  $\sqrt{E_F}$  and  $1/\sqrt{W_r}$  [72, 120].

## 4.4 Carbon Nanotubes

As explained earlier, CNTs show favourable optical absorption and strong photoluminescence efficiency so that they can be used in spaser gain medium [71, 75, 77]. Recent studies have revealed that the transitions involved in this phenomena occur between exciton like states, which arise due to the unique electronic properties inherited by their molecular structure [75, 127]. In analysis, a CNT is assumed to be formed by rolling a graphene sheet around a chiral vector  $\mathbf{C}$  denoted by a pair of integers  $(n, m)$  as shown in Fig. 4.3. Therefore, the electronic properties of CNTs can be derived by applying necessary boundary conditions on graphene band structure according to the zone folding method [71, 112].

### 4.4.1 Density of States of CNTs

First, the two dimensional band structure of graphene is derived according to the tight-binding model and given by [71, 77],

$$E(k_x, k_y) = \pm E_c \sqrt{1 + 4 \cos\left(\frac{3}{2}k_y a\right) \cos\left(\frac{\sqrt{3}}{2}k_x a\right) + 4 \cos^2\left(\frac{\sqrt{3}}{2}k_x a\right)} \quad (4.6)$$

where  $a$  is the c-c bond length and  $E_c$  is the binding energy of carbon atoms. Since a CNT is formed by rolling a graphene sheet along the chiral vector, CNT band

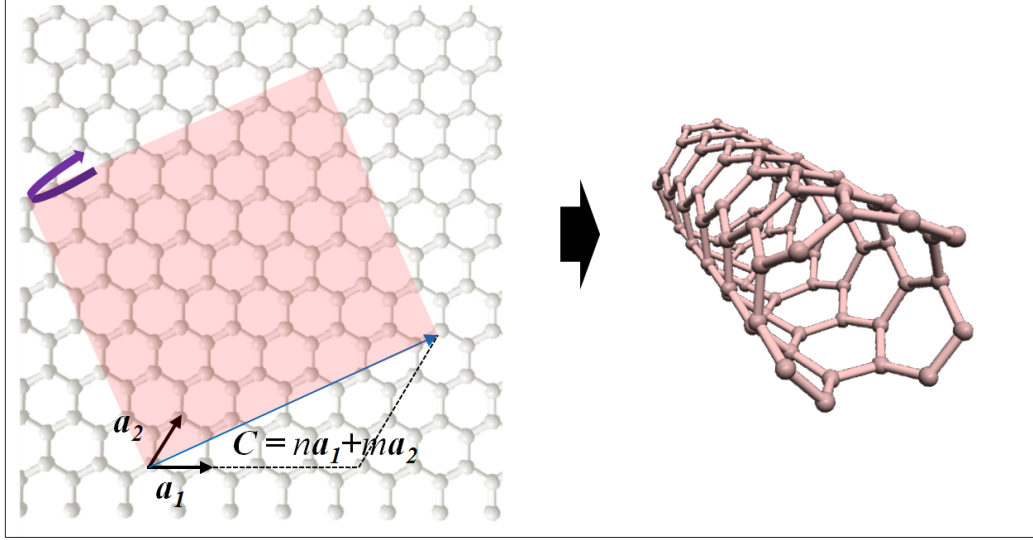


**Figure 4.3:** Formation of a CNT by rolling a graphene sheet

structure is obtained by quantizing the graphene's wavevector along the chiral vector:  $\mathbf{k} \cdot \mathbf{C} = 2\pi\nu$  (where  $\mathbf{k} = (k_x, k_y)$  and  $\nu$  is an integer). Because the angle between  $\mathbf{a}_1$  and  $\mathbf{a}_2$  is  $\pi/3$ , the bandgap becomes zero (*i.e.* the CNT is metallic) if  $\text{mod}|n - m| = 0$  and the CNT is semiconducting otherwise.

Once the band structure is found, the DOS  $D(E)$  can be obtained by summing up the contribution by each band  $\nu$  [71, 77]:

$$D(E) = \frac{\sqrt{3}a^2}{2\pi R} \sum_{\nu=1}^N \int \delta(k - k_\nu) \left| \frac{d\epsilon(k)}{dk} \right|^{-1} dk, \quad (4.7)$$

where  $R$  is the nanotube radius,  $\epsilon(k_\nu) = E$ , and  $N$  is the number of bands. It can be shown that

$$D(E) = \frac{\sqrt{3}a}{\pi^2 R E_c} \sum_{\nu=1}^N \frac{|E|}{\sqrt{E^2 - \epsilon_i^2}} \quad (4.8)$$

where,

$$\epsilon_i = aE_c |3i+1|/2R, \quad N = 4(m^2 + mn + n^2)/\text{gcd}(n, m) \text{ for semiconducting CNTs,}$$

$$\epsilon_i = aE_c |3i|/2R, \quad N = 4(m^2 + mn + n^2)/3\text{gcd}(n, m) \text{ for metallic CNTs,}$$

and 'gcd' stands for greatest common divisor. This gives the CNT DOS plots comprising a series of singularities known to be 'Van Hove singularities' as shown in Fig. 4.4 [77].

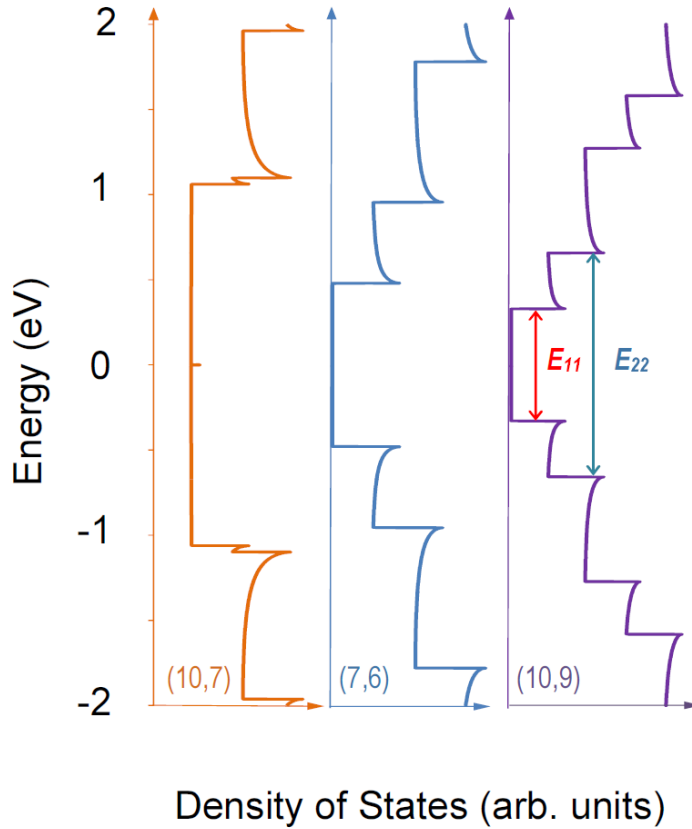


**Figure 4.4:** Density of states for (10,7), (7,6), and (10,9) carbon nanotubes

#### 4.4.2 Semiconducting CNTs for Spaser Gain Medium

The DOS plot of the  $(n, m) = (10, 7)$  CNT in Fig. 4.4 is seen to be everywhere nonzero, indicating the metallic behavior of the nanotube. In contrast, the DOS of the (7,6) and (10,9) CNTs exhibit wide bandgaps, which implies that both nanotubes behave as semiconductors. The peaks in the DOS, Van Hove singularities, facilitate the formation of the well-defined exciton states which enable optical transitions among those states [75, 112]. The energies of the exciton states can be readily found using the DOS plots, as the first two exciton energies as  $E_{11}$  and  $E_{22}$  are marked on the figure.

When used as a gain element in a spaser design, a semiconducting CNT can be resonantly excited by a suitable pump source so that it generates excitons of

energy  $E_{22}$ . These excitons can then relax to a lower state of energy  $E_{11}$  while releasing the excess of energy  $E_{22} - E_{11}$  to the system's ambient. If the energy of the spaser mode equals to  $E_{11}$  and its plasmonic resonator is located closely to the CNT allowing near field interactions, these excitons may annihilate and transfer their energy exciting SPs in the resonator by stimulated emission.

# Chapter 5

## Graphene–Carbon Nanotube Spaser

In this chapter, we propose a carbon-based spaser design where a graphene nanoflake (GNF) resonator is coupled to a carbon nanotube (CNT) gain element. We theoretically demonstrate that the optically excited CNT can nonradiatively transfer its energy to the localized SP modes of the GNF due to near-field interactions between the SPs and the CNT excitons. According to the general model presented in Chapter 2, by calculating the localized fields of the GNF SP modes and the matrix elements for SP–exciton interactions, we find the optimal geometric and material parameters of the spaser that yield the highest SP generation rate. This design is specifically considered because it offers many advantages of carbon materials, including mechanical strength and flexibility, thermal and chemical stability, and utility in biomedical applications [71, 75, 77, 78].

### 5.1 Spaser design

The proposed spaser design shown in Figure 5.1 employs a square shaped graphene nanoflake (GNF) for the plasmonic resonator. This choice of the GNF’s shape is made considering the simplicity of fabrication. As shown in Section 4.3,

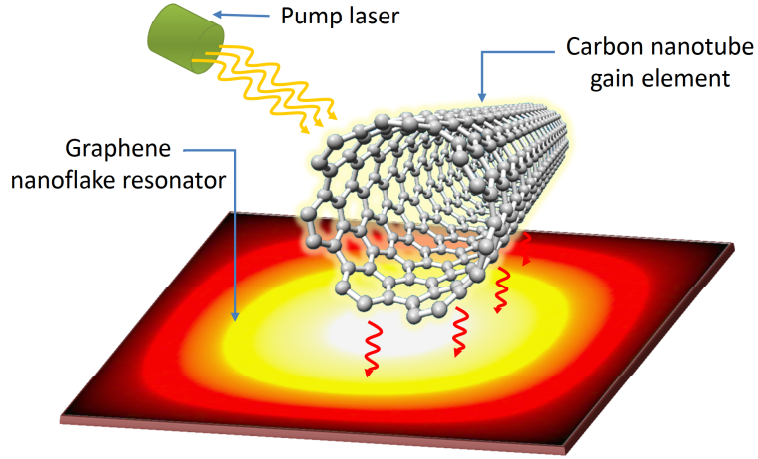


**Figure 5.1:** Schematic of the proposed spaser made of an optically pumped carbon nanotube located above a square graphene nanoflake resonator.

for a given GNF width  $W$ , this resonator supports a series of localized SP modes of unique energies. These modes spatially and spectrally overlap with the CNT excitons in different degrees, therefore experience different amounts of gain. The SP mode that is in resonance with the emission line of the CNT survives receiving the maximum gain and becomes the dominant the spaser mode.

In order to maintain the spasing state, we assume that the CNT is continuously excited by a suitable pump source. Owing to the large absorption cross section of CNTs at visible and infrared frequencies, we consider optical pumping [74, 76]. However, it has also been shown in a quantum wire based setup that even electrical pumping of such a CNT gain element is possible [55]. The CNT excitons generated by absorbing the pump photons annihilate and nonradiatively transfer their energy to GNF SPs. These SPs stimulate the CNT's excited excitons to relax by generating more SPs of the same mode and energy, resulting in a buildup of the spaser mode intensity.

## 5.2 Implementation of the General Model

### 5.2.1 Plasmonic Subsystem

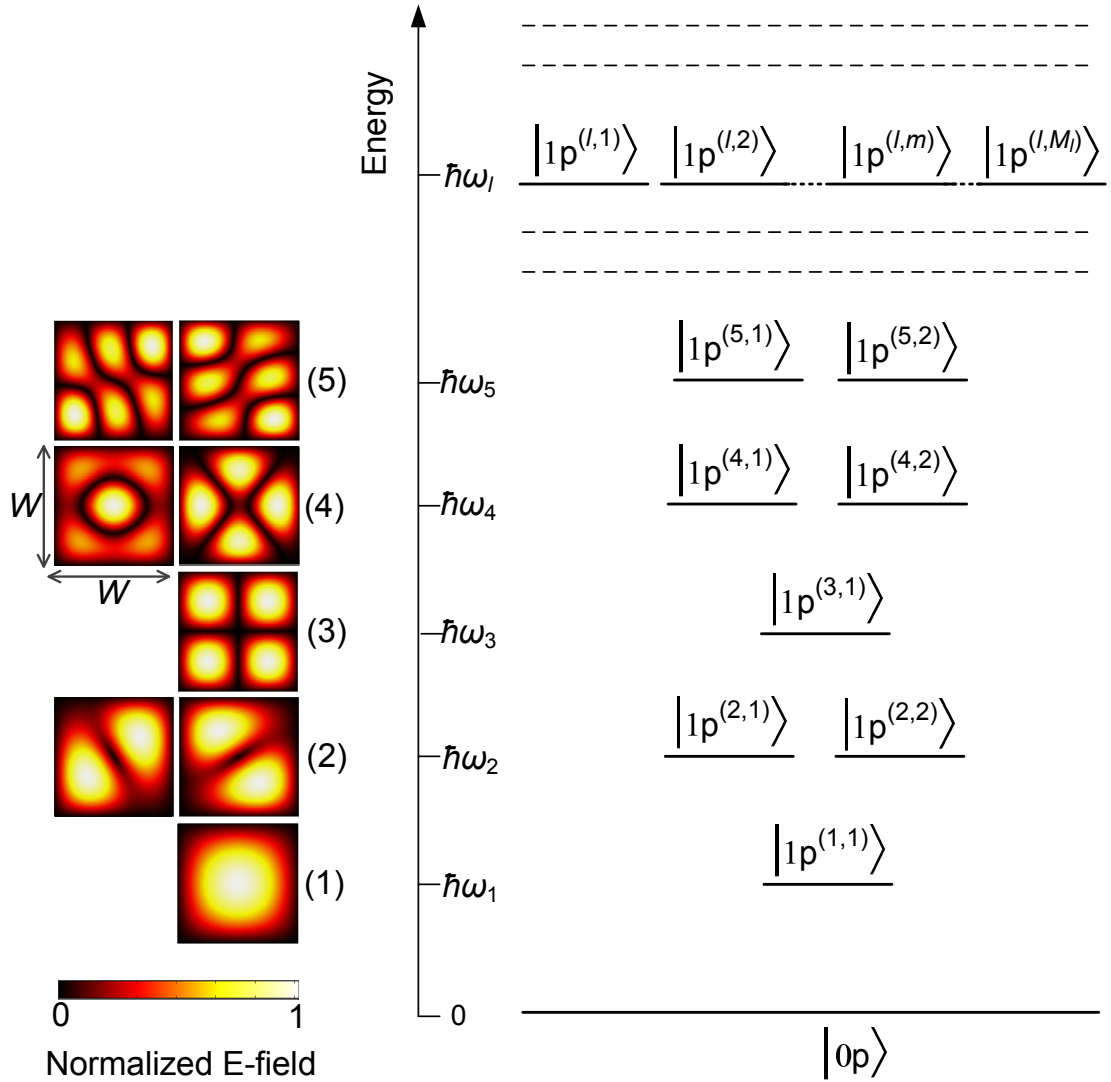


**Figure 5.2:** Plasmonic subsystem of the carbon spaser representing the all SP states with the respective electric field distribution of the each state plotted for the first five modes.

The SP modes supported by the square shaped GNF can be denoted by

$(l, m)$  and their respective energies and field distributions can be found by solving the Helmholtz wave equation with appropriate boundary conditions. According to the numerical solutions obtained (see Section 4.3.1) the square-shaped GNF supports both the degenerate and non-degenerate SP modes. Therefore, the states of the spaser's plasmonic subsystem can be denoted as shown in Fig. 5.3. The SP modes  $l = 1, 3, \text{etc.}$  are non-degenerate, hence the respective SP states can be defined by  $|1p^{l,1}\rangle$ . In contrast, the modes  $l = 2, 4, 5, \text{etc.}$  are doubly degenerate (*i.e.*  $M_l = 2$ ) and the SP states are defined by either  $|1p^{l,1}\rangle$  or  $|1p^{l,2}\rangle$ . We have solved the Helmholtz equation only up to five SP modes and it should be noted that, unlike the case for a sphere, there is no notable pattern for the maximum degeneracy  $M_l$ . This design allows one to select the spaser mode energy to be degenerate or non-degenerate depending on the application requirements.

## 5.2.2 Electronic Subsystem

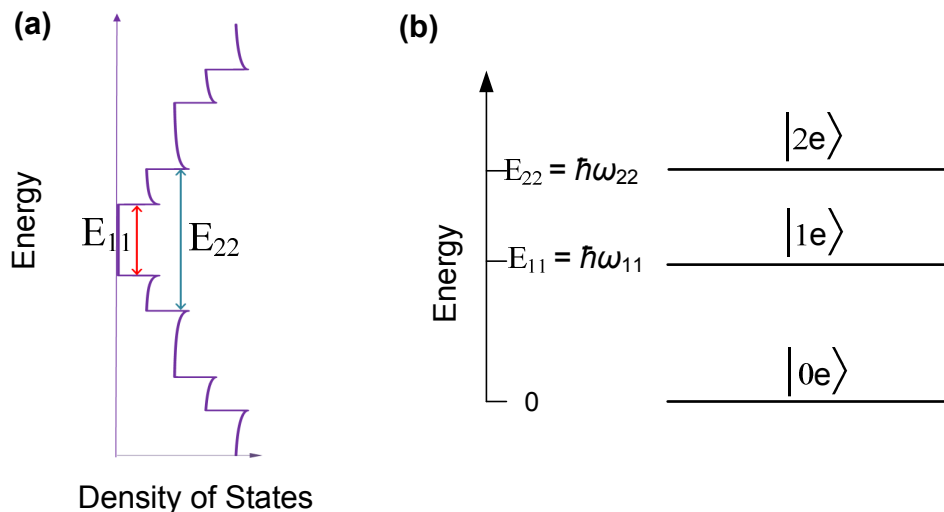


**Figure 5.3:** (a) The excitons having  $E_{11}$  and  $E_{22}$  energy difference between electron and hole bands marked on the DOS plot of a semiconducting CNT and (b) relevant exciton states of the electronic subsystem.

In our spaser design, the optically excited CNT transfers energy nonradiatively to the GNF *via* the exciton–SP interactions. As described in Section 4.4.1, the Van Hove singularities help the formation of exciton states enabling optical transitions [75, 112]. The energies of these exciton states can be readily found using the DOS plots, where we marked the first two exciton energies as  $E_{11}$  and  $E_{22}$ . We design our spaser such that the pump laser resonantly excites a semiconducting CNT from the state  $|0e\rangle$  to  $|2e\rangle$  absorbing  $E_{22}$  amount of energy. The excitons then relax to the state  $|1e\rangle$  of energy  $E_{11}$ , and eventually transfers the excess energy  $E_{22} - E_{11}$  to the environment. If a GNF SP mode is resonantly coupled to the state  $E_{11}$ , the excitons may annihilate and transfer their energy to the GNF in the form of SPs by stimulated emission.

### 5.2.3 States of the Spaser

According to the derived general model in Chapter 2, the carbon spaser can be defined as a quantum system with  $n = M_l + 3$  states given by the tensor product states of the electronic and plasmonic subsystems:

$$\begin{aligned}
|1\rangle &= |0e\rangle|0p\rangle, \\
|2\rangle &= |1e\rangle|0p\rangle, \\
|3\rangle &= |2e\rangle|0p\rangle, \\
|4\rangle &= |0e\rangle|1p^{l,1}\rangle, \\
|5\rangle &= |0e\rangle|1p^{l,2}\rangle, \\
&\dots\dots\dots \\
|n\rangle &= |0e\rangle|1p^{l,M_l}\rangle.
\end{aligned}$$

where  $l$ th SP mode is the spaser mode. For example, the total system will consist of 4 states if the non-degenerate  $l = 1$  is the spaser mode, and 5 states if the doubly degenerate  $l = 2$  is the spaser mode, as shown in Figs. 5.4(a) and (b). This  $n$ -state

system is evaluated using the master equation Eq. (2.14):

$$\frac{\partial \rho_{\mu\nu}(t)}{\partial t} = \frac{1}{i\hbar} [H(t), \rho(t)]_{\mu\nu} - \gamma_{\mu\nu} \rho_{\mu\nu}(t) + \delta_{\mu\nu} \sum_{\kappa \neq \nu} \xi_{\nu\kappa} \rho_{\kappa\kappa}(t), \quad (5.1)$$

which is comprehensively described in Section 2.3.

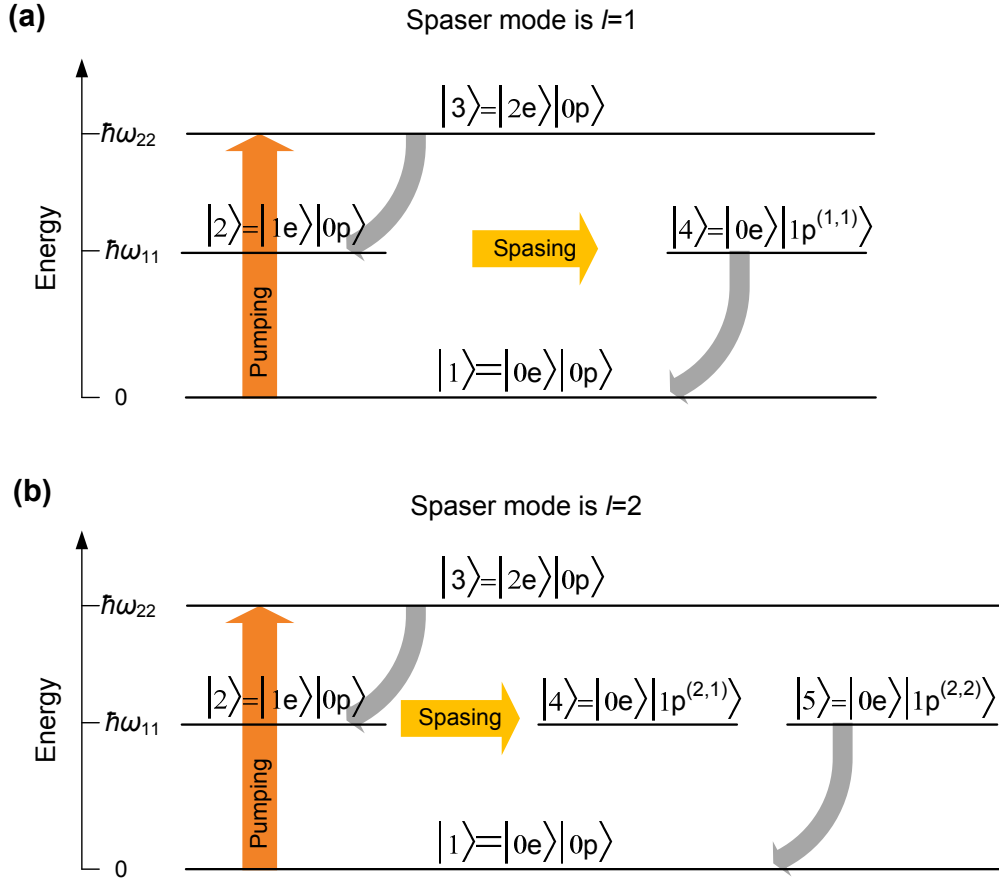


**Figure 5.4:** Product states of the spaser where the (a) non-degenerate  $l = 1$  and (b) doubly degenerate  $l = 2$  SP mode is the spaser mode respectively

## 5.3 Design Optimization

### 5.3.1 Spaser Mode Energy

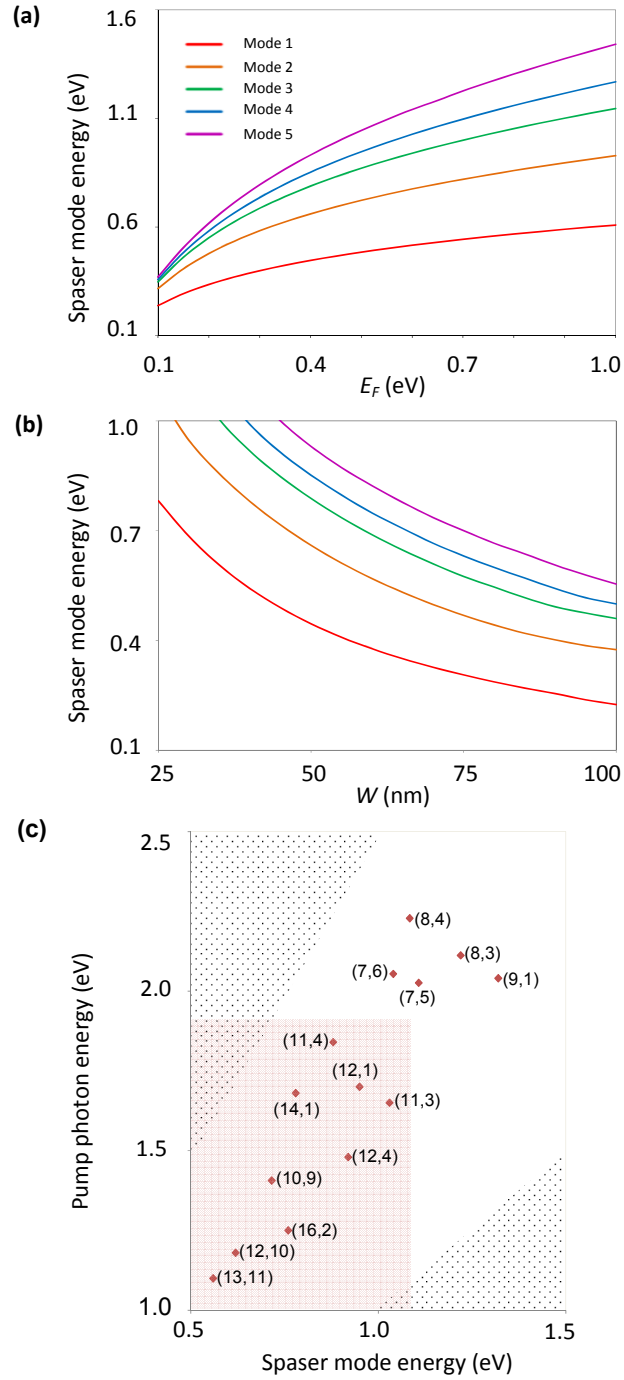
We may choose any SP mode as the spaser mode whose energy can be tuned by changing the width of the GNF  $W$  or Fermi level  $E_F$  by doping or electrostatic gating as shown in Figs. 5.5(a) and 5.5(b). The energies are seen to vary over a wide range from mid to near infrared regimes offering a great flexibility in spaser design. Depending on the application, a suitable energy and a mode could be chosen. However, it should be noted that finding a resonant gain medium would be difficult if the spaser mode energy is very high. If a certain application requires the spaser mode to be  $l = 4, 5$ , *etc.*, picking a low  $E_F$  range around 0.1 eV would give the best results.

Figure 5.5(c) shows several CNTs of different chiralities that can be used in different spaser configurations. There are no CNTs in the dotted region because  $E_{22}$  should be larger than  $E_{11}$ . The CNTs within the red color shaded area are the most favorable for spaser operation, because the energy of the most GNF SP modes are below 1 eV and the energy difference ( $E_{22} - E_{11}$ ) for such CNTs is relatively small. Hence, for a preset ranges of the emission and pumping wavelengths of the spaser, SP generation can be improved by selecting one of the CNTs from the favorable region.

### 5.3.2 SP Generation Rate

By analysing the  $n$ -states system of the carbon spaser using the density matrix formalism (see Section 2.3.2), the total SP generation rate  $\mathcal{R}_l = \sum_{j=4}^n \rho_{\kappa\kappa}$  is given by Eq. (2.16):

$$\mathcal{R}_l = \frac{\xi_{23}\omega_l^2}{2\varepsilon_2\hbar\gamma_{13}\gamma_{22}\gamma_{33}\gamma_p} \frac{\gamma_{2p}}{\gamma_{2p}^2 + \Delta_{2p}^2} |V_{2e,0e}|^2 \sum_{j=4}^n |V_{1e,0e}^{l,j-3}|^2. \quad (5.2)$$



**Figure 5.5:** Spaser mode energy is plotted with respect to (a) Fermi level when  $W = 50$  nm and (b) GNF width when  $E_F = 0.4$  eV, and (c) the spaser mode and pump energies for CNTs with different chirality  $(n, m)$

The required transition matrix elements  $V_{1e,0e}^{l,m} = \langle 1e | \mathbf{E}_{lm} \cdot \mathbf{r} | 0e \rangle$  for SP–exciton interactions are numerically evaluated according to the integral in Eq. (2.11), substituting the numerically obtained  $\mathbf{E}_{lm}$  using the finite element method. Here we assume that the state of the excitons along the CNT is described by the (with respect to the CNT’s center) symmetric Gaussian wave function and also neglect the inhomogeneity of the plasmonic field across the nanotube’s diameter, which is less than 1 nm [113].

Now, using these results, we study how the performance of the spaser could be optimized. Similar to the approach followed for the nanosphere–QD spaser in Chapter 3, we keep the material dependant decay rates ( $\xi_{23}$ ,  $\gamma_{13}$ ,  $\gamma_{22}$ , and  $\gamma_{33}$ ) and the matrix element for pump light–exciton interactions  $|V_{2e,0e}|$  constant and plot normalized  $\mathcal{R}_i$  with respect to the tuning parameters we consider for design optimization. We assume the values for other constants as  $\tau=10^{-13}$  s,  $\gamma_p=10^{10}$  s $^{-1}$ ,  $a=0.142$  nm, and  $E_c=3$  eV, reasonably agreeing with literature [70, 71, 73, 75, 77].

Consider the spaser configuration shown in Fig. 5.6 which consists of a semi-conducting CNT of length  $L$  whose axis is located at a distance  $H$ , parallel to the surface of a  $W \times W$  square GNF. For the sake of simplicity, we assume that the centers of the GNF and CNT coincide while the nanotube’s axis makes an angle  $\theta$  with the GNF edge. The interested GNFs widths lie between 25 and 100 nm, where the used conductivity model is accurate enough. The CNT length  $L$  may vary from  $0.2W$  to  $2.5W$  and  $H$  is varied within the range of 5 to 20 nm, allowing the near-field coupling between the GNF SPs and CNT excitons.

Figures 5.7(a) and 5.7(b) show how the normalized rates  $\mathcal{R}_1$  and  $\mathcal{R}_2$  vary with respect to geometric parameters  $W$ ,  $L$  and  $\theta$  for  $H = 5$  nm. It is seen that both  $\mathcal{R}_1$  and  $\mathcal{R}_2$  peak for  $L \approx 1.1W$ , with their absolute maxima achieved for  $\theta = \pi/4 + (\pi/2)k$  and  $\theta = \pi k$  ( $k = 0, 1, 2, \dots$ ), respectively. There are optimal angles because the electric field distribution shapes are different for each SP mode. This is why the mutual orientation of the CNT and GNF is crucial for spaser performance and it should be tuned according to the spasing mode. When the

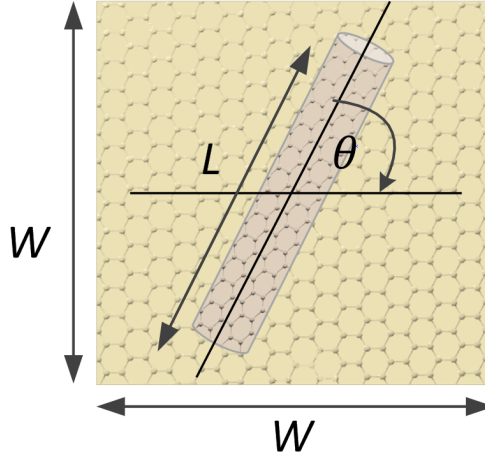


**Figure 5.6:** Configuration of the spaser design

length of the CNT becomes smaller than the optimal length, the SP generation rate reduces due to the reduction in the CNT's dipole moment. In the alternate situation of CNT's size exceeding the optimal length, the reduction in the SP generation rate is explained by the reduced spatial overlap between the SP field and the CNT's excitons.

Figure 5.7(c) illustrates the impact of the near-field coupling between the CNT and GNF on the SP generation rate. The figure shows how  $\mathcal{R}_l$  varies with the distance from the CNT center to the GNF's plane for the first five SP modes. For each mode, we choose the optimal spaser parameters:  $L = 1.1W = 35$  nm,  $\theta = \pi/4$  for  $l = \{1, 3\}$ , and  $\theta = 0$  for the rest of the modes. The SP generation rate is seen to rapidly decrease with the CNT moving away from the GNF for all spaser modes. In addition, the SP generation rate corresponding to the degenerate modes (with  $l = 2, 4,$  and  $5$ ) are slightly larger than for the nondegenerate modes. This might be due to the stronger spatial overlap of their near fields with the CNT excitons as there are two mode orientations present.

To achieve a high spasing efficiency, the spaser mode should be resonantly coupled to the lower exciton state  $|1e\rangle$ . The coupling can be realized by matching the GNF's SP mode energy  $\omega_l$  with  $E_{11}$  by changing  $W$  or  $E_F$  (see Figs. 5.5(a)

and (b)). Figure 5.8(a) shows how the SP generation rate  $\mathcal{R}_1$  varies with the SP mode energy for five different CNTs, at their optimum configuration  $\theta = \pi/4$ ,  $L = 1.1W = 35$  nm, and  $H = 5$  nm. The widths of the spectra on this figure together with Fig. 5.5(b) indicate that the realization of the resonant SP–exciton coupling would require a fabrication tolerance of about 1 nm. Alternatively, one can achieve the resonance between the GNF SPs and the CNT excitons by doping the CNT, oxidizing it, or having multiple carbon layers [71, 128, 129].

If several CNTs have the desired exciton spectrum, then the preference should be given to the CNT with the highest emission and absorption cross sections at resonance. The most preferable CNTs are located in the right top corner of Fig. 5.8(b), which indicates the two kinds of cross sections for 13 CNTs of different chirality vectors. The positions of the CNTs within the plot were obtained using empirical formulas [130].

### 5.3.3 Threshold Gain and Quality Factor

In addition to the SP generation rate, it is important to analyze the threshold gain required for continuous spasing. This gain is known to predominantly depend on the dielectric properties of spaser materials [42]. According to Fig. 5.9(a), threshold gain grows exponentially with the spaser mode energy. For a given value of  $E_{SP}$ , the spasing threshold can be significantly reduced by doping the GNF and increasing its Fermi level. As evidenced by Fig. 5.9(b), doping would simultaneously improve the quality factor of the GNF resonator, which would in turn result in lower losses and improved spaser performance.

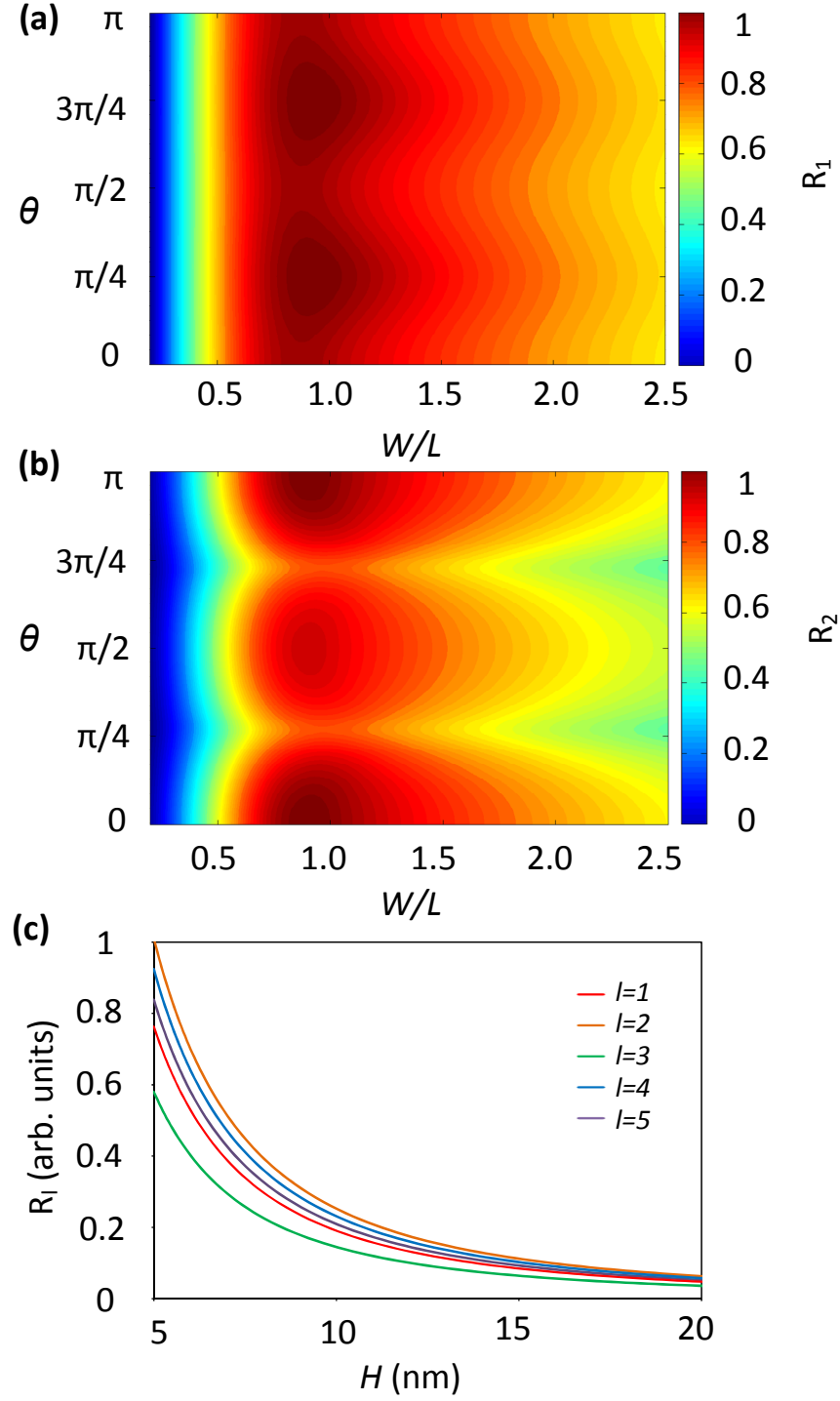


**Figure 5.7:** Normalized plasmon generation rates (a)  $\mathcal{R}_1$  and (b)  $\mathcal{R}_2$  in the  $\vartheta$ - $W/L$  domain and (c)  $\mathcal{R}_l$  vs  $H$  for five lowest-energy spaser modes;  $L = 1.1W = 35$  nm,  $\theta = \pi/4$  for  $l = \{1, 3\}$  and  $\theta = 0$  for  $l = \{2, 4, 5\}$

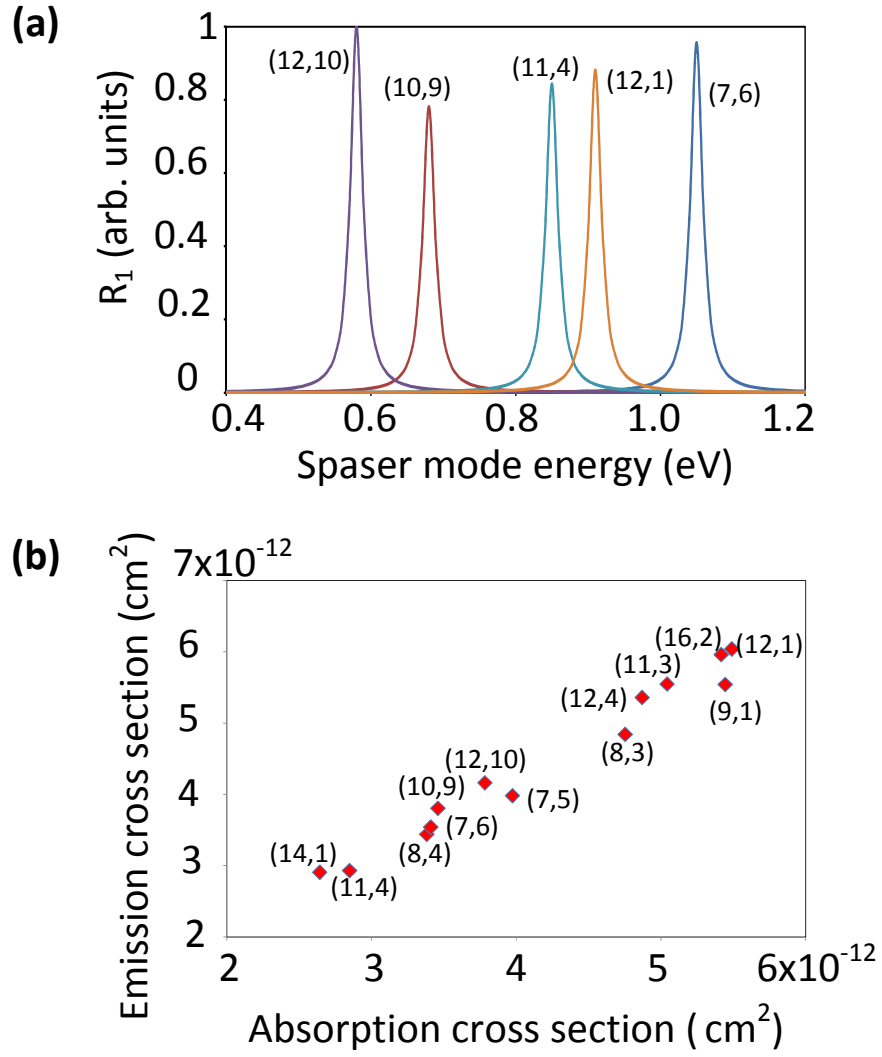


**Figure 5.8:** (a)  $\mathcal{R}_1$  as a function of spaser mode energy for five CNTs,  $\theta = \pi/4$ , and  $L = 1.1W = 35$  nm and (b) absorption and emission cross sections at resonance for different nanotubes of unit lengths.

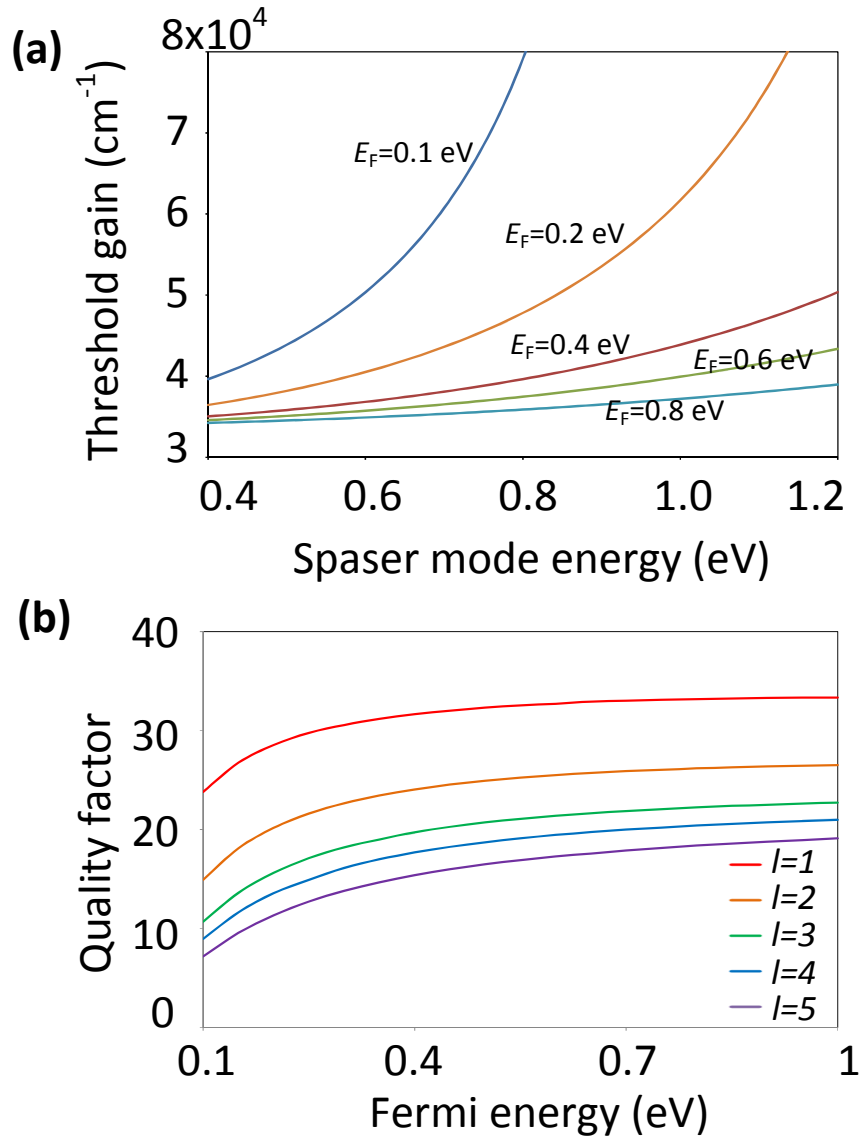


**Figure 5.9:** (a) Threshold gain *vs* spaser mode energy for different Fermi energies; (b) quality factor of the first five SP modes *vs*  $E_F$  for  $W = 30$  nm.

## 5.4 Advantage of the Design

The analysis of the spaser performance suggests that the proposed all-carbon design is highly tunable and can be optimized to achieve a high SP generation rate. In particular, the spaser mode energy can be varied from 0.2 to 1.2 eV, spanning across a wide range of near and mid infrared frequencies. The emission energy can be tuned within this range by changing the geometric parameters ( $W$ ,  $L$ , and  $\theta$ ) and the material parameters ( $E_F$  and CNT chirality) of the spaser. The results presented in Figs. 5.5–5.9 provide the necessary information for such a parametric tuning. For instance, to design a spaser emitting at the 1362 nm wavelength (which corresponds to the SP mode energy of 0.91 eV), one might use the second mode of a sufficiently doped, 38 nm wide GNF with  $E_F=0.4$  eV (see Fig. 5.5(b)). According to Figs. 5.5(c) and 5.8(b), the optimum generation of the spaser mode could be achieved using a 34 nm long CNT of chirality vector (12,1) oriented parallel to a pair of the GNF's edges ( $\theta = 0$ ). The pumping wavelength must then be set around 730 nm. This example suggests that the obtained results can serve as the design guidelines for the experimental realization of a graphene–CNT spaser. Availability of many tuning parameters of the spaser design significantly facilitate easy fabrication by making the suggested parameters flexible.

The proposed graphene–CNT spaser can be experimentally realized using the common nanofabrication techniques. A graphene sheet can be formed using such methods as chemical vapor deposition (CVD), micromechanical cleavage, graphite oxide exfoliation, or epitaxial growth on a substrate [123, 124]. When the spaser's emission wavelength (or the spaser mode energy) is chosen, Fig. 5.5 allows one to select the appropriate width of the GNF to be patterned using a convenient method, *e.g.* lithography, transfer printing, or direct laser shaping [131]. The GNF can then be transferred to a low-index dielectric substrate such as SiO<sub>2</sub> or polydimethylsiloxane (PDMS). After that, a suitable CNT, picked up according to the pumping and emission energies shown in Fig. 5.5(c), can be fabricated using

CVD or other convenient technology [132]. The distance between the GNF and CNT can be controlled by depositing a layer of the substrate material on top of the GNF. This may introduce weak substrate effects, such as a small shift of the spacing wavelength, which can be neglected if the substrate material is of low refractive index and nondispersive [133].

In addition to broad tunability, the proposed spaser design offers advantages such as mechanical strength and thermal stability due to the unique properties of both graphene and CNTs. It can be used as an active element in plasmonic nanocircuits, which overcome the miniaturization and bandwidth limitations of the conventional optical and electronic circuits. The devices employing these circuits would inherit the robustness and stability properties of carbon allotropes. The possible applications of spasers made of GNFs and CNTs range from ultrafast processors and flexible electronics to high-temperature devices and biomedical sensing [71].

# Chapter 6

## Guidelines for Spaser Design and Optimization

So far, we have presented a general quantum mechanical model for spaser nanolasers which considering the SP degeneracy, and studied the performance of two spaser designs; a simple metal nanosphere–QD spaser (in Chapter 3) and a GNF–CNT spaser (in Chapter 5) based on the developed model. In both the cases, we saw that both the designs can be optimized for a high SP generation rate by tuning some material and geometric parameters of the spaser components. With this knowledge of the influence of different design parameters on the output characteristics, in this chapter we attempt to provide clear design and optimization guidelines for spasers in general.

### 6.1 Designing Spaser Components

#### 6.1.1 Plasmonic Resonator

The plasmonic resonator of a spaser is supposed to support SP modes and therefore essentially made of plasmonic materials. As comprehensively described in Chapter 4, only gold, silver, and graphene, could be used as the resonator materials

because only the nanoparticles made of these materials have shown strong localized surface plasmon resonances in visible or infrared frequencies. Table 6.1 summarizes the achievable spaser mode energies  $\hbar\omega_l$  for some types of resonators. It is seen that graphene resonators are tunable over a wide range in the near and mid infrared energies. However, if one needs a visible light frequency, the only choice would be gold or silver. Once the spaser mode energy and the type of the resonator are decided, the exact tuning parameters can be calculated by solving the Helmholtz equation analytically or numerically as we have done in Sections 3.2 and 4.3.1 for gold and graphene resonators.

Although  $\hbar\omega_l$  could be tuned at a high precision with the given geometrical parameters, it might be difficult to find a gain medium that can be resonantly coupled to all the  $\hbar\omega_l$  values. Therefore in practice, once the favourable range for  $\hbar\omega_l$  is identified, the best match could be achievable by first selecting the gain medium and then tuning the resonator to achieve the resonant energy transfer.

### 6.1.2 Gain Medium

There are plenty of options available when designing the gain medium of a spaser, some of which are listed in Table 6.2. Depending on the spaser mode energy, there can be many ways to select the suitable gain medium for a design. Different types of QDs provide a large range of emission energies within both the visible and NIR regimes. The advantages of QDs are smaller linewidths and continuous tunability with its size parameters. Although only few types are given in the table there are many varieties of QDs with different semiconductor materials.

Although dyes do not support continuous tuning like QDs, there are many dye types made out from a large number chemical compounds which can resonantly transfer energy to any plasmonic resonator after a slight tuning of the spaser mode energy. Rare earth ions are similar, but as there are not much variations, there is less freedom of tuning. Semiconducting CNTs are nanowires those with discrete energy levels as we have described comprehensively in Section 4.4. There are a

**Table 6.1:** Tunability of spaser mode energies for some resonator types [1–6]

<b>Material</b>	<b>Shape</b>	<b>Spaser mode energy (eV)</b>	<b>Tuning parameters</b>
Silver	sphere core/shell	2.4 – 3.5 visible	radius, shell thickness
	cube	2.5 – 3.1 visible	width, length, height
	rectangular bar	1.38 – 3.1 visible & NIR	width, length
	spheroid	1.4 – 3.1 visible & NIR	radius 1, radius 2
Gold	sphere core/shell	1 – 2.4 visible & NIR	radius, shell thickness
	rod	1.3– 1.8 NIR	radius, length
	cube	2– 2.5 visible	width, length, height
	spheroid	1.4– 2.5 visible and NIR	radius 1, radius 2
Graphene	square	0.1 – 1.5 near & mid IR	width, length

**Table 6.2:** Characteristics of different gain media [7–15]

Gain Medium	Pump energy (eV)	Spaser mode energy (eV)	Tuning parameters
<b>Quantum dots</b>			
CdSe	1.9 – 3 visible	1.7 – 2.7 visible	size
CdS	3.0 – 4.5 visible	2.5 – 4.2 visible	size
CdTe/CdSe	1.7 – 2.3 visible	1.4 – 1.9 visible and NIR	core size, shell thickness
InAs	1.1 – 1.7 NIR	0.9 – 1.5 NIR	size
<b>Dyes</b>	0.8 – 4.5 visible & NIR	0.6 – 4 visible & NIR	chemical compound (discrete values)
<b>Rare earth ions</b>	0.8 – 4.5 visible & NIR	0.9 – 3 visible & NIR	chemical compound (discrete values)
<b>Carbon nanotubes</b>	1 – 2.5 visible & NIR	0.5 – 1.5 NIR	chirality ( $n, m$ ) (discrete values)

number of different CNTs with different chiralities giving a large set of possible spaser mode and pumping energies. Although CNTs are not tunable as QDs, they can be much advantageous in applications, especially where robustness is a key factor.

### 6.1.3 Pumping Mechanism

*Optical pumping* is the most common method of exciting the spaser gain medium. In this mechanism an external laser is used to pump energy in the form of photons which are absorbed by the gain medium atoms to achieve population inver-

sion [18, 42]. The stimulated emission of SPs can take place continuously as the population inversion is maintained by an uninterrupted supply of pump photons. However, if a semiconductor gain medium is used, *electrical pumping* would also be a viable option. In this method an electrical current is injected through the semiconductor, generating e–h pairs of high energies. In some cases a nanocrystal or nanowire gain medium like CNT is used to directly inject through the pump energy [55, 134]. In addition, there are some other mechanisms such as electric discharge and chemical pumping used in lasers which we do not consider in spaser design due to practical limitations.

## 6.2 Operational Characteristics and Optimization Parameters

### 6.2.1 SP Generation Rate

The main purpose of a spaser nanolaser is to be utilized as a coherent source of SPs. Therefore the SP generation rate becomes the most important parameter when designing a spaser. As derived from our general model, the SP generation rate of a spaser is given by Eq. (2.16):

$$\mathcal{R}_l = \frac{\xi_{23}\omega_l^2}{2\varepsilon_2\hbar\gamma_{13}\gamma_{22}\gamma_{33}\gamma_p} \frac{\gamma_{2p}}{\gamma_{2p}^2 + \Delta_{2p}^2} |V_{2e,0e}|^2 \sum_{j=4}^n |V_{1e,0e}^{l,j-3}|^2. \quad (6.1)$$

This expression suggests that the SP generation rate can be boosted by the following methods.

#### 1. Increasing the SP–exciton matrix element for each degenerate SP state of the spaser mode $l$ .

The matrix element  $|V_{1e,0e}^{l,m}|$  is a measure of how strong the energy transfer from gain medium to the SP mode  $(l, m)$ . According to Eq. (2.11)

$$|V_{1e,0e}^{l,m}| \propto \int_V \psi_{1e}^*(\mathbf{r}) E_{lm}(\mathbf{r}) \psi_{0e}(\mathbf{r}) \, d\mathbf{r}, \quad (6.2)$$

which depends on the amount of excitons' spatial overlap with the SP's electric field. Therefore placing the gain elements as close as possible to the field's hotspots would produce the best results. The effect of clever gain medium placement can be clearly seen in Figs. 3.5 and 5.7 for nanosphere–QD and graphene–CNT spaser designs. If there are more than one gain element, the resultant matrix element is the summation of the integrals relevant to each gain element. In such situations, gain elements should be placed to achieve the highest collective spacial overlap rather than focusing on getting the maximum overlap for one or few elements.

## 2. Increasing the pump light–exciton matrix element

Similar to  $|V_{1e,0e}^{l,m}|$ , the matrix element for pump light–exciton interactions is given by

$$|V_{2e,0e}| \propto \int_V \psi_{2e}^*(\mathbf{r}) E_L(\mathbf{r}) \psi_{0e}(\mathbf{r}) d\mathbf{r}, \quad (6.3)$$

where  $E_L(\mathbf{r})$  is the electric field caused by pump light. This integral value can be increased by using gain elements with high absorption cross section and having a high exciton density in the gain medium. Although increasing the pumping intensity would also increase  $|V_{2e,0e}|$ , we do not consider it as an optimization parameter because that requires raising the input power of the device.

## 3. Using an optimum spaser mode energy $\hbar\omega_l$

Although  $\mathcal{R}_l \propto \omega_l^2$ , having a very high spaser mode energy might cause an increase in the threshold gain requiring high pumping power. Spasing would not occur if the pump power is less than the threshold. Therefore it is required to determine the spaser mode energy to be at the optimum point of operation.

## 4. Decreasing the detuning $\Delta_{2p}$

The detuning  $\Delta_{2p} = \hbar(\omega_2 - \omega_p)$  is the energy difference between the state  $|2\rangle = |1e\rangle|0p\rangle$  and any degenerate SP state  $|p\rangle = |0e\rangle|1p^{l,m}\rangle$ . In ideal reso-

nant coupling  $\Delta_{2p} = 0$  which may be difficult to achieve in practice. However, a slightly high value for  $\Delta_{2p}$  causes a drastic drop in SP generation rate as shown in Figs. (3.6) and (5.8). Therefore this detuning should be minimized as much as possible to obtain a high SP generation rate.

## 5. Selecting materials with suitable relaxation constants

In addition to these parameters, there is a significant contribution from the relaxation rates  $\gamma_{13}$ ,  $\gamma_{22}$ ,  $\gamma_{33}$ ,  $\xi_{23}$ , and  $\gamma_p$ , of the gain medium materials. Gain medium materials should be chosen such that the SP generation rate is maximized.

### 6.2.2 Threshold Gain

Spaser should be designed to minimize the required input power for the continuous operation. This is determined by the threshold gain required by the gain medium for continuous spasing which is given by Eq. (7.7):

$$g_{th} = \frac{\omega_l}{c\sqrt{\varepsilon_2}} \frac{\text{Im}\varepsilon_1(\omega_l)}{\left[ \text{Re}\left(\frac{\varepsilon_2}{\varepsilon_2 - \varepsilon_1(\omega_l)}\right) \right]^{-1} - 1}. \quad (6.4)$$

where  $\varepsilon_1(\omega_l)$  and  $\varepsilon_2$  are the dielectric constants of the resonator and the gain medium respectively. This quantity mainly depends on the spaser mode energy  $\hbar\omega_l$ . Figs. 3.7 and 5.9 show how the respective design parameters influences  $g_{th}$  for the analyzed two spaser designs. Threshold gain is found to be exponentially increasing with the spaser mode energy. Therefore the parameters should be chosen such that both the SP generation rate and threshold gain are at optimum values.

### 6.2.3 Resonator Quality Factor

Another characteristic to be optimized is the resonator's quality (Q) factor. The Q factor is a measurement of the energy loss with SP oscillations. When the eigenfrequencies  $\omega_l + i\gamma_l$  of a resonator are found by solving the Helmholtz equation, Q factor of the resonator is given by  $\omega_l/2\gamma_l$  for each mode. Although

nanoscale spaser resonators may not have large Q factors (see Fig. (5.9)) like microresonators, it is important to design resonators with relatively high Q factor to sustain SP oscillations for a long time.

#### 6.2.4 Direction of Symmetry Breaking

One advantage of the presented general model in Chapter 2 is that it enables the designer to manipulate the direction of symmetry breaking. It is possible to populate one SP state with a particular degeneracy. By placing the gain medium such that  $|V_{1e,0e}^{l,m}|$  is large for certain  $m$  compared to others, the SP field can be oriented in one direction. This might be helpful in some applications where non-symmetric field patterns are required.

# Chapter 7

## Applications of Spasers

### 7.1 SP Sources in Nanoplasmonic Devices

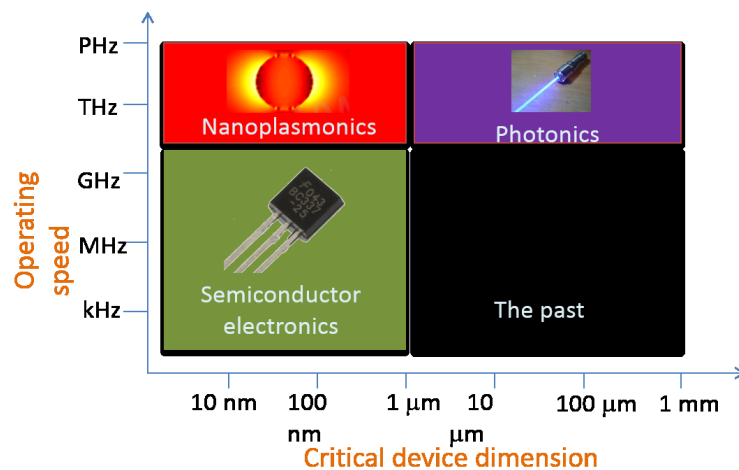


**Figure 7.1:** Speed and critical device dimensions of different technologies [19]

Earlier, nanoplasmonics was only used in the applications such as microscopy and sensing. However, recently new trends have been emerged of nanoplasmonic circuitry and devices, as they can potentially overcome the speed and miniaturization barriers of other technologies. Although semiconductor electronics have shown a great success in past 50 years or so, they experience RC delays limiting

the processing speed. In contrast, photonics can facilitate high speed processing but the miniaturizing beyond the diffraction limit is constrained. Therefore nanoplasmonics is the only technology which allows the fabrication of ultra-fast and ultra-small devices as shown in Fig. 7.1, because SPs can be confined to the nanoscale [19, 25, 42].

To build circuits, we need active devices which act as sources of carriers, similar to the transistor in electronics or laser in optics. Spaser is the device that can fulfill this requirement in nanoplasmonics. As we have shown in Chapter 3 and 5, spasers may have different designs where their SP generation rate and frequencies can be controlled by tuning some design parameters and the pumping intensity. Figure 7.2 shows such a proposed rough schematic for a nanoplasmonic circuit where the spaser nanolasers pump SPs into the circuits which propagate along plasmonic waveguides. A substrate containing gain elements can be used to compensate losses, ensuring the SP propagation.

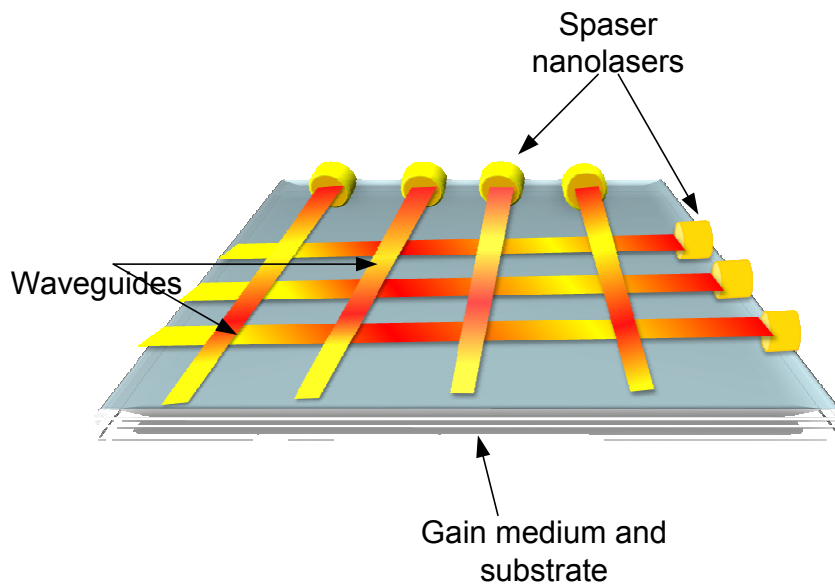


**Figure 7.2:** Use of spasers in a nanoplasmonic circuit

### 7.1.1 Logic Circuits and Processors

According to Ref. [32], spaser can be used as a bistable amplifier representing logical ‘0’ and ‘1’. The bit transitions  $0 \rightarrow 1$  and  $1 \rightarrow 0$  can be controlled by changing the pumping level. Notably, it has been shown that the transition time is in the order of femtoseconds, therefore the information processing speed can reach well above 100 GHz. In these ultrafast nanoplasmonic chips, individual spasers can communicate with each other through their local optical fields or connected nanoplasmonic wires Fig. 7.2.

## 7.2 Qbits in Quantum Computers

Quantum bits are different from the bits used in conventional computing as they can take more than two states of ‘0’ and ‘1’. Instead, a qbit can be in any of superposition state  $\alpha |\mathbf{0}\rangle + \beta |\mathbf{1}\rangle$  where the probability amplitudes  $|\alpha|^2 + |\beta|^2 = 1$ . Generally, any quantum system with an observable quantity, which has at least two discrete eigenvalues, is a suitable candidate for implementing a qubit [135, 136]. Hence, there are many ways of using spasers in quantum computers.

According to the general model discussed in Chapter 2, spaser is a quantum systems with  $n$  linearly independent states. For example, when the mode 2 is the spaser mode in carbon spaser discussed in Chapter 5, it becomes a system with 5 states (see Fig. 5.4):

$$\begin{aligned} |1\rangle &= |0e\rangle |0p\rangle \\ |2\rangle &= |1e\rangle |0p\rangle \\ |3\rangle &= |2e\rangle |0p\rangle \\ |4\rangle &= |0e\rangle |1p^{2,1}\rangle \\ |5\rangle &= |0e\rangle |1p^{2,2}\rangle. \end{aligned}$$

Therefore it is possible to employ this spaser as a qbit with the notation  $|4\rangle \equiv |\mathbf{0}\rangle$  and  $|5\rangle \equiv |\mathbf{1}\rangle$ . This approach is much similar to the qbits defined with respect to the polarisation of photons in linear optics quantum computing (LOQC), where horizontal and vertical polarizations are considered as the states  $|\mathbf{0}\rangle$  and  $|\mathbf{1}\rangle$  [137, 138].

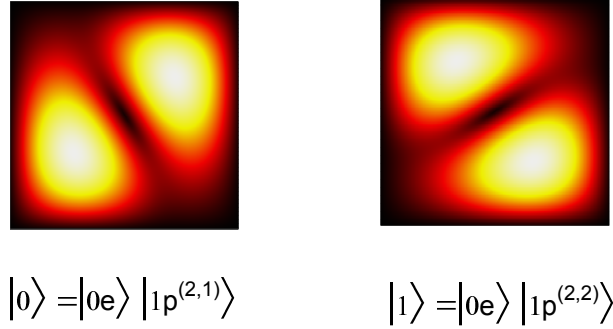


**Figure 7.3:** Utilization of square GNF's doubly degenerate SP mode  $l = 1$  in a spaser to implement  $|\mathbf{0}\rangle$  and  $|\mathbf{1}\rangle$  qbits

Therefore values of  $\alpha$  and  $\beta$  in the superposition states  $\alpha |\mathbf{0}\rangle + \beta |\mathbf{1}\rangle$  would be proportional to the interaction matrix elements  $V_{1e,0e}^{1,1}$  and  $V_{1e,0e}^{1,2}$  respectively. It is possible to use two CNTs in both sides of the GNF aligned with two mode shapes. Then the preferred states can be easily prepared by tuning the pumping strength for each CNT.

### 7.2.1 Cavity QED Approach

Another promising way of implementing quantum computers is using cavity quantum electrodynamics [139, 140]. This approach uses a resonantly coupled atom and an optical cavity as a qbit. The same concept can be applied for spasers as well. For a non-degenerate SP mode (*e.g.*  $l = 1$ ), it is possible to define  $|\mathbf{0}\rangle = |2\rangle = |1e\rangle |0p\rangle$  and  $|\mathbf{1}\rangle = |4\rangle = |0e\rangle |1p^{l,1}\rangle$  as the qbit states. According to the Hamiltonian for interactions between SP modes and exciton states given in

Eq. (2.8):

$$H_{e,p} = i\hbar g_l V_{1e,0e}^{l,1} (\hat{b}_{l,1}^\dagger |0e\rangle \langle 1e| + \hat{b}_{l,1} |1e\rangle \langle 0e|), \quad (7.1)$$

and there exist entangled states [139];

$$|\pm\rangle = \frac{1}{\sqrt{2}}(|\mathbf{0}\rangle \pm |\mathbf{1}\rangle), \quad (7.2)$$

hence possible to construct quantum logic gates [139].

### 7.3 In Biomedical Applications

Plasmonic nanoparticles are excellent optical energy absorbers and also capable of concentrate heat energy. Therefore they have been widely used in biosensing and photothermal cancer therapy research [19, 25, 42, 141]. Spaser resonators too are plasmonic nanoparticle assisted by a gain medium. Therefore they can perform better than individual nanoparticles in many situations. For example, a spaser can sense biological signals much efficiently with amplification and concentrate much larger heat energy with stimulated emission of SPs.

### 7.4 Spaser Powered Photothermal Cancer Therapy

Effective cancer therapies are among the most sought after technologies in biomedical research. Although centuries of oncology research has been able to deliver somewhat satisfactory chemotherapy and radiotherapy based treatments, they cause many undesired side effects [142, 143]. This is because both these methods considerably damage the healthy cells in the patient's body while destroying the malignant cancer cells. Therefore, with the advancements of nanotechnologies, much attention has been drawn on selective destruction of malignant cells while healthy cells around are kept intact. One of the well known proposal to achieve this

objective is photothermal cancer therapy, in which the cancer cells are thermally ablated by electromagnetic radiation [141].

Early proposals of photothermal therapy were mostly focused on local hyperthermia generated using a laser or microwave beam as a direct thermal energy source for cells [144, 145]. However, it has been shown later that metal nanoparticle assisted photothermal therapy can deliver much improved results as they can efficiently absorb photo-energy from laser radiation and convert them into heat through surface plasmon resonance (SPR) [17, 141]. In this approach, initially a large number of metal nanoparticles are delivered into the patient's body so that most of them surround the malignant cancer cells. This can be practically achieved *in vivo* by binding those nanoparticles with so called 'targeting agents'; *e.g.* some antibodies and peptides [4, 141, 146], or employing a passive targeting mechanism like enhanced permeability and retention (EPR) effect [79]. Then the locality of targeted cells can be illuminated with an external laser so that metal nanoparticles can absorb energy and dissipate heat into the surrounding. This should be done until a sufficient temperature is achieved to burn these cells.

The proposed nanolaser cancer therapy is an improved version of photothermal therapy because the targeted cells are surrounded by spaser nanolasers instead nanoparticles. In spaser, there is a metal nanoparticle that undergoes SPR, and in addition, there is a gain medium that amplifies the resonant plasmonic fields in the nanoparticle. The stimulated emission based field amplification in spasers causes the build-up of a certain SP mode in the metal nanoparticles. Hence, when spasers are used in photothermal therapy, this active component can help to multiply the energy concentration and make the cell destruction more efficient compared to the conventional approach.

Using the guidelines provided in Chapter 6, these spasers can be designed and optimized by proper selection of materials and tuning the structural design to suit *in vivo* operation. So far, successful demonstrations of conventional photothermal therapy have used nanoparticles such as spherical gold nanoshells [141, 147],

nanorods [4], graphene [79], and carbon nanotubes (CNTs) [80], as the photon absorbing elements. Importantly, these nanoparticles have been chosen because their resonance energies can be tuned within the NIR regime where light shows relatively less attenuation in biological tissues [141]. Here we opt for graphene and CNTs to surround cancer cells and operate together as spasers for enhanced cell ablation with optical pumping is present. This choice is made due to recent experimental success of much improved photothermal therapy with graphene [79, 148], and our previous work (Chapter 5) showing that a graphene nanoflake (GNF) in tandem with a semiconducting CNT can efficiently operate as a spaser. Another advantage of using graphene and CNTs is their favourable thermal properties. Both these materials are excellent heat conductors and thermally stable even at very high temperatures over 1000 °C [71], thus the thermal damage of the device is not possible during the therapy.

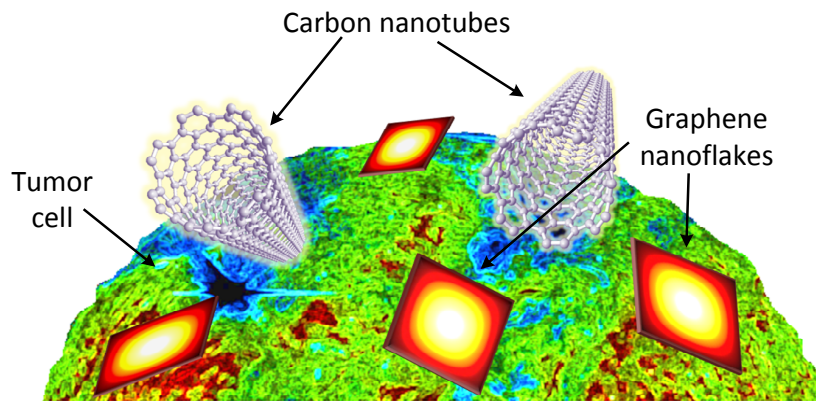


**Figure 7.4:** Delivered GNFs and CNTs surround the tumor cells due to targeting mechanisms and becomes a self-assembled cluster of nanolasers

### 7.4.1 Spaser Operation Near Cancer Cells

When GNFs and CNTs are successfully delivered to a cancer cell, they can operate as a self-assembled cluster of spaser nanolasers as shown in Fig. 7.4. Here,

GNFs behave as plasmonic resonators and receive energy nonradiatively from excited CNTs in the vicinity. As discussed in Chapter 5, this energy transfer takes place when the excitons of CNTs are in resonance with one of the SP modes supported by GNFs. Since these excitons decay with this energy relaxation, CNTs should be pumped with a suitable energy source to maintain them in excited state. An advantage of using CNTs is their excitation energies in the NIR regime which helps minimally attenuated optical pumping for *in vivo* operation of the spaser cluster. It is possible to use one of the two NIR windows; 600-950 nm and 1000-1350 nm wavelength ranges, where the attenuation of the electromagnetic waves in biological tissues is relatively low. The attenuation can be further minimized by using optical fibre to deliver the pump photons as close as possible to a tumor site. When sufficient pump energy is available to achieve population inversion (*i.e.* above threshold gain), stimulated emission of SPs (spasing) occurs building up a large plasmonic field localized on GNFs [28, 149]. Due to high energy concentration on GNFs, temperature of the surrounding increases thermally ablating the cancer cells [79, 141].

For a substantial heat dissipation, GNFs should receive energy resonantly at the SPR wavelength ( $\lambda_{SP}$ ) which mainly depends on the GNF shape and the level of doping. For the case of a square shaped GNF, the case we considered throughout this thesis for the sake of simplicity,  $\lambda_{SP}$  mainly depends on the GNF width  $W$  and the Fermi level  $E_F$  possessed due to doping [149]. The wavelength  $\lambda_{SP}$  and the corresponding electric field  $\hat{\mathbf{E}}_{SP}$  generated on a GNF can be found by solving the Helmholtz wave equation  $(\nabla^2 + k^2)\hat{\mathbf{E}}_{SP} = 0$  where  $k$  is the wave number. Although the solution gives a series of SP eigenmodes (see Section 4.3.1), for this therapy, we only take the lowest energy first mode which is usually within the considered wavelengths and easy to excite [25].

The field intensity of the first SP mode excited on a  $W$  wide square shaped GNF is shown in Fig. 7.5(a). This eigenmode has the form  $|\hat{\mathbf{E}}_{SP}(\mathbf{r})| = A_{SP} \sin(\frac{x}{W}) \sin(\frac{y}{W})$  where the amplitude  $A_{SP}$  depends on the number of SPs ( $N_{SP}$ ) sustained on the

GNF by the active medium. Within the SP quantization scheme (Eq. (2.2)):

$$\int_V \frac{1}{2} \frac{\partial}{\partial \omega} (\omega \epsilon(\omega)) |\hat{\mathbf{E}}_{SP}(\mathbf{r})|^2 d\mathbf{r} = \hbar \omega_{SP}, \quad (7.3)$$

amplitude of  $\hat{\mathbf{E}}_{SP}(\mathbf{r})$  is of the order of  $10^7$  V/m for one SP on a GNF with considered dimensions where  $|\hat{\mathbf{E}}_{SP}| \propto \sqrt{N_{SP}}$ . Therefore the plot in Fig. 7.5(a) is normalized for an arbitrary  $N_{SP}$ .

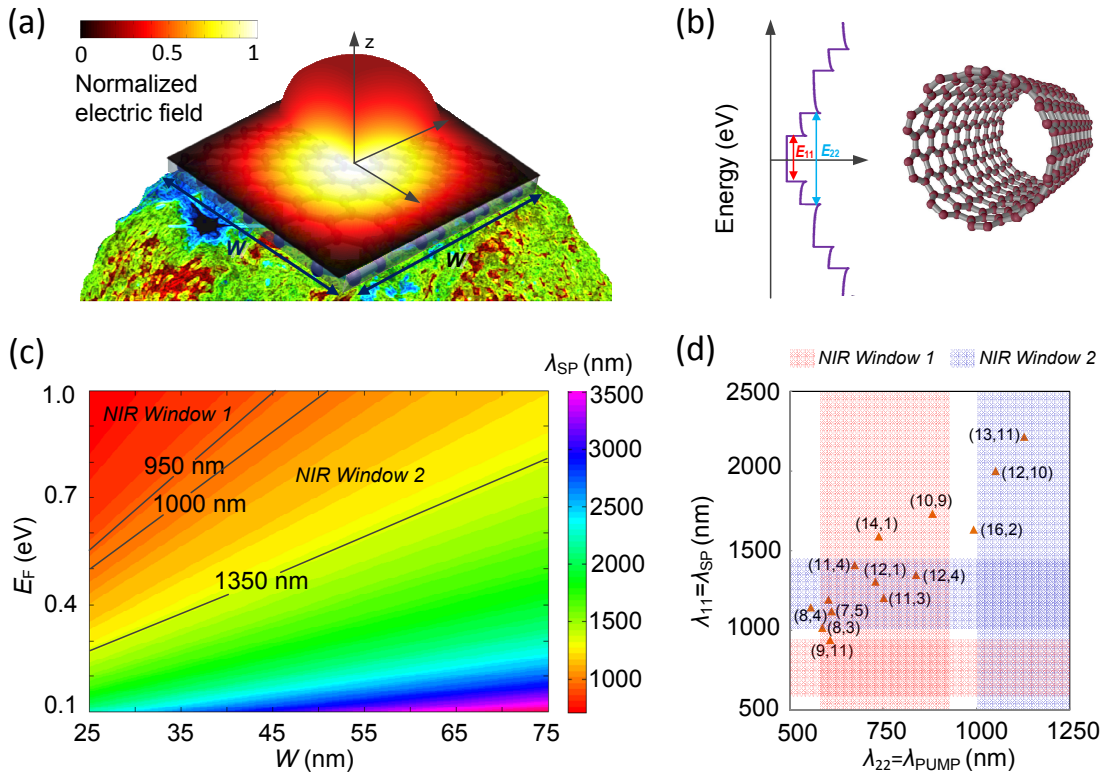


**Figure 7.5:** (a) Electric field generated on the GNF resonator, (b) a typical density of states plot of a semiconducting CNT where two lowest energy excitons  $E_{11}$  and  $E_{22}$  are marked, (c) GNF's resonant wavelengths depending on the width  $W$  and Fermi level  $E_F$ , and (d) the dependence of the  $\lambda_{11}$  and  $\lambda_{22}$  wavelengths (corresponding energies  $E_{11}$  and  $E_{22}$ ) on the chirality  $(n, m)$  of CNTs

The wavelengths of generated SPs on GNFs ( $\lambda_{SP}$ ) and absorption by CNTs ( $\lambda_{PUMP}$ ) should be properly selected to optimize this therapy. First, these wave-

lengths should be preferably placed within NIR windows. Figure 7.5(c) shows the placement of  $\lambda_{SP}$  for different values of  $W$  and  $E_F$ . However, the best case scenario would be selecting pumping wavelength within NIR window 1 ( $E_{22} = 1.3 \sim 2$  eV) and the spasing wavelength within NIR window 2 ( $E_{22} = 0.9 \sim 1.25$  eV) so that the gain medium CNTs can be selected according to Fig. 7.5(d). It is possible to select a range of CNTs like (8,3), (7,5), (11,3), *etc.* within the NIR windows of interest to meet the requirement of spasing. These CNTs also have relative high absorption cross sections compared to other nanotubes (see Fig. 5.8(b)). When a CNT is selected, the spasing wavelength is known and the resonant GNF width could be found according to Fig. 7.5(b) enabling strong interactions between the resonator and the gain medium.

## 7.4.2 Efficiency of the Therapy

Let us assume a treatment for a tumor of  $V_t$  volume. To treat this cancer, first we inject targeting agents attached  $m_g(g)$  dose of GNFs and  $m_{cnt}(g)$  dose of CNTs to deliver  $N_g$  number of GNFs and  $N_{cnt}$  number of CNTs to the tumor site. Hence,

$$N_g \approx \alpha_g \frac{m_g \times N_A}{12 \times (W^2/1.3 \times a^2)}, \quad (7.4)$$

$$N_{cnt} \approx \alpha_{cnt} \frac{m_{cnt} \times N_A}{12 \times (\pi d_{cnt} L / 1.3 \times a^2)}, \quad (7.5)$$

where  $\alpha_g$  and  $\alpha_{cnt}$  are the targeting efficiencies of functionalized GNFs and CNTs,  $N_A$  is the Avogadro constant,  $a = 0.142$  nm is the C-C bond length in graphene,  $L$  is the CNT length, and  $d_{cnt} \approx 0.0783\sqrt{n^2 + nm + m^2}$  nm is the CNT diameter. For this therapy we keep  $N_g : N_{cnt} \approx 1 : 1$  for formation of the spaser cluster and  $W \approx L$  considering the optimized performance according to Section. 5.3. In addition, the density of the resonators and gain elements of the spaser cluster are given by  $N_g/V_t$  and  $N_{cnt}/V_t$  respectively, giving the average resonator–gain element displacement:

$$d_x = \frac{1}{2} \left( \frac{3V_t}{4\pi N_g N_{cnt}} \right)^{1/3} (N_g^{1/3} + N_{cnt}^{1/3}), \quad (7.6)$$

assuming that the nanoparticles are Poisson distributed. This becomes  $d_x = \left(\frac{3V_t}{4\pi N_g}\right)^{1/3}$  for the case of  $N_g \approx N_{cnt}$ .

Let us study the case in which (11,3) semiconducting CNTs are used for the gain medium. Then, the pumping and spasing wavelengths would be 751 nm and 1190 nm ( $\hbar\omega_{SP}=1.05$  eV) respectively. This energy would be resonant to a 25 nm wide GNF with 0.4 eV Fermi level. We assume that the attached targeting agents do not alter the optical properties of GNFs and CNTs in this theoretical treatment. Within our general model, availability of many gain elements can be taken through superposition by each element. Since  $N_g : N_{cnt} \approx 1 : 1$ , it is reasonable to assume that the whole effect by the spaser cluster is equivalent to the operation of  $N_g$  average spasers having similar design considered in Chapter 5. In order to sustain population inversion within the gain medium, pumping should be provided above the spasing threshold. Threshold gain of a spaser design is given by,[42]

$$g_{th} = \frac{\omega_{SP}}{c\sqrt{\varepsilon_2}} \frac{\text{Im}\varepsilon_1(\omega_{SP})}{\left[\text{Re}\left(\frac{\varepsilon_2}{\varepsilon_2 - \varepsilon_1(\omega_{SP})}\right)\right]^{-1} - 1}, \quad (7.7)$$

where  $\varepsilon_1(\omega_{SP})$  and  $\varepsilon_2$  are permittivities of the resonator and gain medium respectively. For above set parameters, threshold gain is  $4.5 \times 10^4 \text{ s}^{-1}$  and therefore the threshold pump power turns out to be  $0.015 \text{ W/cm}^2$ . Therefore *in vivo* spasing takes place when the external NIR laser pumps energy beyond this rate and the SP field gets largely amplified due to stimulated emission.

Therefore, the kinetics of this spaser cluster can be analysed according to Section 5.3 and we prefer CNT length  $L \approx W$  for the optimum SP generation rate (see Fig. 5.7). Under these conditions, the SP generation rate for the mode 1 can be derived from Eq. (5.2):

$$\mathcal{R}_1 = \frac{\xi_{23}\omega_{SP}^2}{2\varepsilon_2\hbar\gamma_{13}\gamma_{22}\gamma_{33}\gamma_p} \frac{\gamma_{2p}}{\gamma_{2p}^2 + \Delta_{2p}^2} |V_{2e,0e}|^2 |V_{1e,0e}^{1,1}|^2, \quad (7.8)$$

where the matrix elements  $V_{2e,0e}$  and  $V_{1e,0e}^{1,1}$  are found from the integral in Eq. (2.11). For the relaxation rate constants we assume conservative values  $\gamma_{13} = \gamma_{22} = \gamma_{33} = 10^{10}$ ,  $\gamma_p = 10^{13}$  and  $\gamma_{2p} \approx 1/2(\gamma_{22} + \gamma_p)$  reasonably agreeing with literature [71,

73, 75, 77]. This allows us to obtain a rough estimation of the efficiency of the therapy by calculating the electric field generated on GNFs and then estimating the temperature rise of the surrounding.

Since the objective of this study is to calculate the efficiency of the nanolaser therapy, we do not focus on the exact scattering and the propagation through the tissue. Instead, it is assumed that the NIR laser beam is  $\beta$  times attenuated when a treated cancer cell is reached. We'll show that, even with high attenuation values such as  $\beta = 10$  times, spaser based therapy can efficiently ablate cancer cells. Therefore in this analysis (and in Figs. 7.6) and (7.7), pump power implies the power density received at a cancer cell which is much less than the actual laser power. We also assume that the linewidth of the pump laser is less than 1 MHz, so that the coherence length within biological tissue is high enough, allowing to be treated as continuous wave pumping for the gain elements.

We use the RF module of COMSOL Multiphysics finite element analysis software to calculate the electric fields and its Bioheat transfer module to study the temperature rise with time. Here, the time dependant temperature  $T(t)$  is found by solving the Pennes bioheat equation [150, 151]:

$$\rho C_p \frac{\partial T}{\partial t} + \nabla \cdot (-k \nabla T) = \rho_b C_b \omega_b (T_b - T) + Q_{met} + Q_{ext}, \quad (7.9)$$

where  $\rho$ ,  $C_p$ , and  $k$ , are the density, specific heat capacity, and thermal conductivity of the tissue where the cancer is grown,  $\rho_b$ ,  $C_b$ ,  $T_b$  and  $\omega_b$ , are the density, specific heat capacity, temperature, and perfusion rate of blood, and  $Q_{met}$  and  $Q_{pump}$  are the heat generated by metabolism and the NIR pump laser respectively. For this study, we consider a nanolaser treatment for tumor grown in liver area with the values:[152–154]

blood density  $\rho_b = 1 \times 10^3 \text{ kg/m}^3$ ,

specific heat capacity of blood  $C_b = 3,639 \text{ J/(kg}\cdot\text{K)}$ ,

perfusion rate of blood  $\omega_b = 3.6 \times 10^{-3} \text{ 1/s}$ ,

temperature of blood  $T_b = 37^\circ\text{C}$ ,

thermal conductivity of liver tissues  $k_p = 0.56 \text{ W}/(\text{m}\cdot\text{K})$ ,  
density of liver tissues  $\rho_p = 1.05 \times 10^3 \text{ kg}/\text{m}^3$ ,  
specific heat capacity of liver tissues  $C_p = 3600 \text{ J}/(\text{kg}\cdot\text{K})$ ,  
and heat generated due to metabolism  $Q_{met} = 33,800 \text{ W}/\text{m}^3$  and

$$Q_{SP} = \frac{1}{2}\sigma(\omega)|\mathbf{E}_{lm}(\mathbf{r})|^2 \quad (7.10)$$

Figures 7.6 and 7.7 show the simulation results with respect to different pump powers and nanoparticle dosages. For effective cell ablation, temperature should be raised over  $50 \text{ }^\circ\text{C}$  [79, 141]. According to Fig. 7.6(a), which plots the temperature of the tumor after 10 s laser irradiation,  $50 \text{ }^\circ\text{C}$  can be easily reached within a short period of radiation with power varying from  $0.1$  to  $2 \text{ W}/\text{cm}^2$  with appropriate number of nanoparticles  $N_g$  ( $\approx N_{cnt}$ ) in the vicinity. In these plots, zero attenuation of the laser power and 100% targeting efficiency are assumed. This is because the targeting efficiency and attenuation coefficient highly depend on the situation. Therefore, the actual power and dosage should be selected according to the conditional estimations. For example, if the attenuation  $\beta$  is found to be 10 times and the targeting efficiencies  $\alpha_g$  and  $\alpha_{cnt}$  are about 50%, the pump laser should be 10 times powerful and the dosage should be as double as the values derived from the plots.

Figure 7.6(b) shows the time taken by tumor cells to reach  $60 \text{ }^\circ\text{C}$ , which is more than sufficient for thermal ablation, under different conditions. It might take as long as 250 s for low powers and low nanoparticle (NP) concentrations. However, with  $N_g = 10^{13} \text{ NP}/\text{cm}^3$  GNFs and CNTs,  $60 \text{ }^\circ\text{C}$  can be achieved with much low powers such as  $0.1 \text{ W}/\text{cm}^2$  within 50 s. Power requirement gets even smaller for larger dosages and *vice versa*. The temperature variation with time is more clearly illustrated in Fig. 7.7. According to Fig. 7.7(a), which plots the time dependant temperature for a fixed nanoparticle concentration  $N_g = 10^{12} \text{ NP}/\text{cm}^3$ , the rate of the temperature rise rapidly increases with the irradiation power. This is because the undertaking stimulated emission is getting stronger

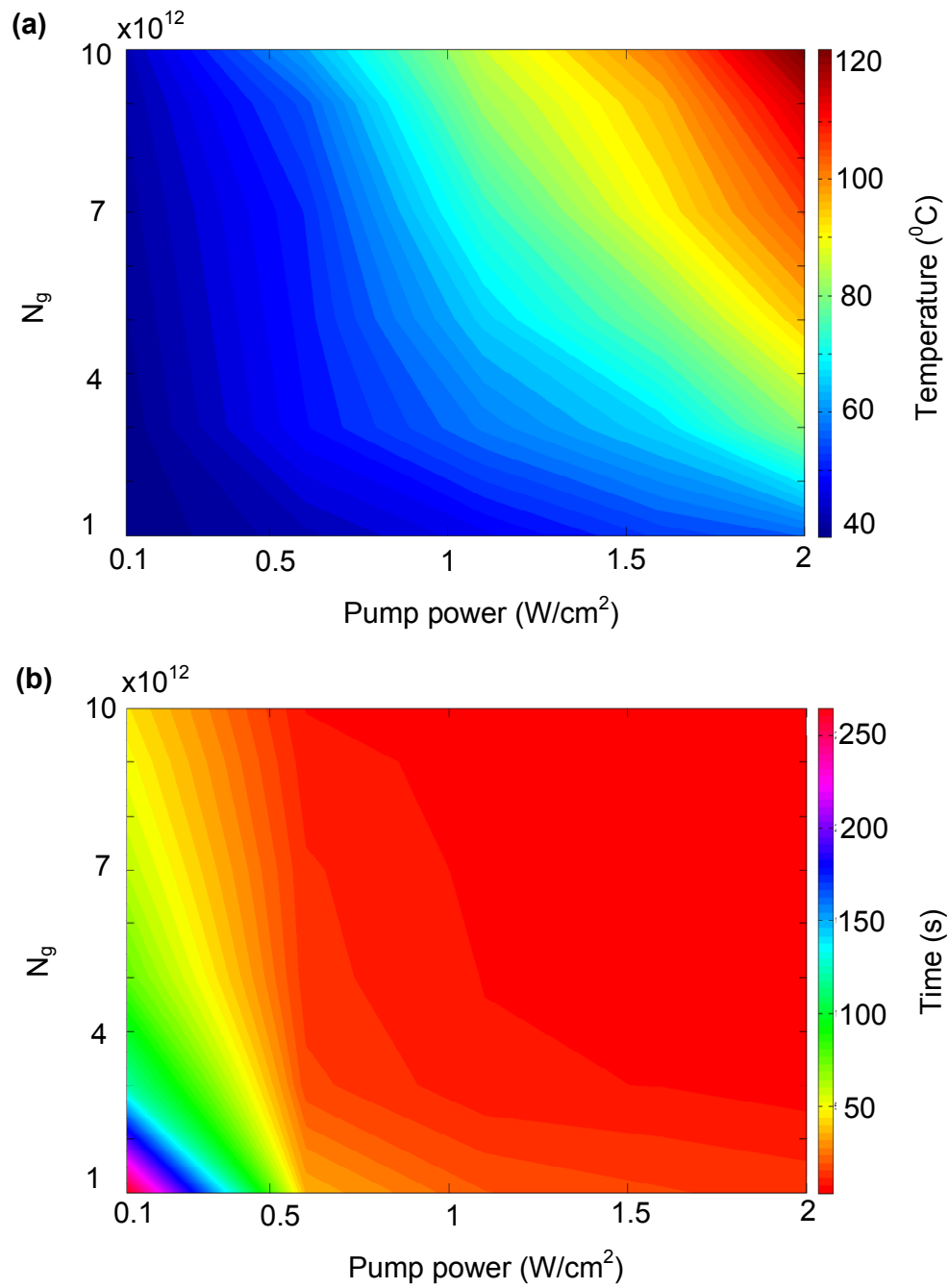


**Figure 7.6:** (a) The temperature after 10s of NIR laser irradiation and (b) time taken to reach 60<sup>o</sup> C for different pump power values and number of nanoparticles reached the tumor site

due to the fast excitation of the gain medium. From these plots, it is advisable to have a nanoparticle concentrations over  $N_g = 10^{12}$  NP/cm<sup>3</sup> because the time to reach 60 °C looks too high for lower irradiation powers. This fact is consolidated according to Fig. 7.7(b), where slightly higher concentrations show better results. This is due to the increase of the GNF–CNT coupling efficiency with strong near field interactions.

Although high concentrations and irradiation powers result in large heat generation, low values are always preferable for the patient’s health. In this therapy, when 10 times attenuation and 50% targeting efficiency are assumed, injection of  $2 \times 10^{13}$  NP/cm<sup>3</sup> GNFs and CNTs (total  $4 \times 10^{13}$  NP/cm<sup>3</sup>) and irradiating with 1 W/cm<sup>2</sup> NIR for 40 s can elevate the tumor’s temperature to 60 °C. This is a considerable improvement compared to the recently obtained best results for conventional photothermal therapy in Ref. [79], where a 2 W/cm<sup>2</sup> laser is used with about  $10^{15}$  nanoparticles delivered to the tumor site raising its temperature over 50 °C. This significant improvement is achieved because the stimulated emission of SPs is the underlying mechanism of this therapy. As the theory of spaser and experimental verifications suggest, spasers can generate much larger SP fields compared to SP generation by direct light illumination [18, 42]. Therefore, proposed spaser powered nanolaser cancer therapy can show much better results compared to conventional photothermal therapy.

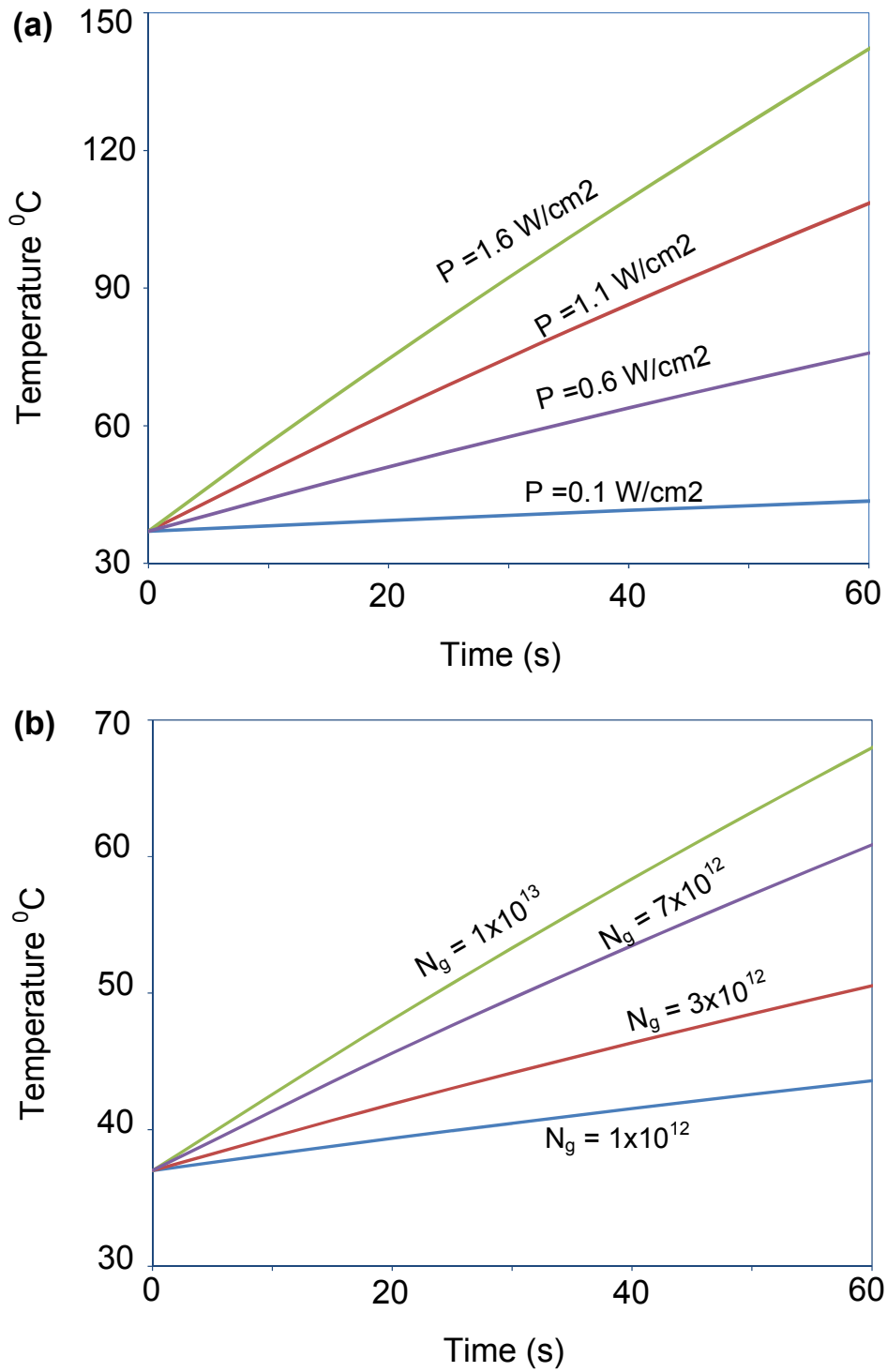


**Figure 7.7:** The temperature rise with respect to irradiation time (a) for different pump powers when  $N_g = 10^{12}$  and (b) for different nanoparticle numbers when pump power is  $0.1 \text{ W/cm}^2$ .

# Chapter 8

## Conclusions and Suggestions for Future Work

### 8.1 Conclusions

The spaser (or nanolaser), which is the nanoplasmonic counterpart of the laser, enables the generation and amplification of coherent SPs by means of stimulated emission. A typical spaser consists of a plasmonic resonator which supports SP modes and an externally pumped gain medium which amplifies these SP modes. Spasing occurs as a result of non-radiative resonant energy transfer from the gain medium to a particular SP mode called ‘spaser mode’ *via* exciton relaxation. This research has been conducted with the objectives of studying the engineering aspects of the spaser, particularly the models for design optimization, new designs with unique characteristics, design guidelines, and the potential applications of spasers.

First, we developed a general quantum mechanical model for spaser considering the degeneracy of SP modes to identify the important parameters in design and optimization. This model describes the spaser as a composite quantum system with  $n$ -states when the spaser mode is  $(n - 3)$  times degenerate. The performed density matrix analysis on this system led to obtain an expression for the SP generation rate of a spaser. This analysis also revealed that a spaser design can

be optimized for improved output characteristics by tuning certain material and geometrical parameters.

Then we studied a simple spaser design in which a spherical gold-silica core-shell resonator is powered by an optically pumped QD gain element. The spherical resonator supports a series of SP modes denoted by  $l$  which are  $2l + 1$  times degenerate. Hence the total system consists of  $n = 2l + 4$  states and it becomes  $n = 6$  for the dipole mode. The geometrical parameters such as core radius, shell thickness, QD radius, and the QD placement, were found directly influencing the resonator-gain medium interactions. Therefore, the optimum output characteristics such as the spaser mode energy, SP generation rate, threshold gain, resonator quality factor, and direction of symmetry breaking can be achieved by proper tuning of these parameters. The other important parameters are the pumping intensity and the decay constants of the spaser materials.

Suitable materials for a plasmonic resonator are silver, gold, and graphene, and the gain medium may consist of QDs, QWs, dyes, rare earth ions, or CNTs. However, most proposed spaser designs have used only few of these such as silver, gold, and QD/QWs. Nonetheless, graphene possesses much better plasmonic properties compared to gold or silver, whilst CNTs are phenomenal in absorption and photoluminescence. In addition, the devices made of them offer excellent tunability, robustness, flexibility, and thermal stability characteristics. Therefore, we have proposed a new all-carbon spaser design where a square shaped GNF resonator powered by a CNT gain element. Degeneracy levels of GNF SP modes are much different from the spherical resonator. The quantum systems having  $n = 4$  states for the non-degenerate first mode and  $n = 5$  states for the doubly degenerate second mode have been analysed according to the developed general model. The identified tuning parameters are the width and Fermi level of the GNF, CNT length, and relative placement of them.

According to our results for both these designs and the developed model, the operational characteristics of any spaser highly depend on its design. Therefore we

attempted to obtain clear design guidelines to meet the requirements and optimized the design. These guidelines include identifying the crucial parameters, designing the resonator, choosing the appropriate gain medium and pumping mechanism, and relative placement of the components.

From the engineering perspective, potential applications are equally important as the models, designs, and optimization guidelines, for spaser nanolasers. It has already been shown that they can be used to construct ultra-fast and ultra-small logic devices with nanoplasmonic circuits. Further, we have proposed more application scenarios in quantum computing and biomedical engineering. Especially, we have proposed a new ‘nanolaser cancer therapy’ where a large number of nanolasers selectively destroy cancer cells by thermal ablation. These nanolasers are self-assembled of separately injected GNFs and CNTs which are attached with targeting agents. The proposed therapy has shown improved efficiency compared to the conventional photothermal cancer therapy.

The idea of the spaser was proposed in 2003 [28] and experimentally demonstrated in 2009 [18]. It has been identified as the potential device that can take Moore’s law beyond 2020 with improving the processing speed. Our effort by this research is to discuss it in terms of models for design optimization, unique designs, and new applications of spasers, catalysing its progress and seeing real world applications in near future.

## **8.2 Suggestions for Future Work**

The work presented in this thesis can be extended in many pathways. First, we assumed that there is no interaction between gain elements in the context of multiple gain elements. For this reason our analysis is based on the resonator’s interaction with one gain element, so that the total result can be obtained by the superposition of the influence of individual elements. However, this might not be 100% accurate in some situations. Therefore the proposed general model can be im-

proved for the spasers with multiple gain elements with the presence of interactions between them. Secondly, although CW pumping is assumed in all our analyses, pulsed pumping methods might be useful in some applications. Hence, extending our model for pulsed operation may make it even more beneficial. Thirdly, factors affecting the decay rates of the materials were not considered. Sometimes they were kept constant or conservative values were assumed while giving priority to major tuning parameters. However, these constants also contribute to the output characteristics and may be tuned by controlling some factors such as temperature or chemical means. Another factor to be considered is the possibility of electric-field-induced fluorescence quenching in the gain medium. Although this might slightly reduce the expected SP generation rate of a spaser, the effect will be minimal as spasing is a nonradiative phenomenon [155, 156]. However, the consideration of fluorescence quenching can further improve the developed general model. Therefore extending the model with these additional information may provide more flexibility in design optimization.

Finally, much more work can be done on the proposed applications. In the performance analysis done on the cancer therapy, the growth factor of tumors, change of dielectric factors with cell death, change of optical properties of the nanoparticles due to attaching targeting agents, and the moving nature of nanoparticles were not considered. Therefore much precise estimations can be obtained incorporating these facts. For other applications of nanoplasmonic circuits and quantum computers, we have just highlighted the possible use case scenarios and a proper analysis is yet to be done. A detailed work may help to get an idea on device function, processing speed, and methods of realization.

# Abbreviations

CNT	Carbon Nanotube
CW	Continuous Wave
DOS	Density of States
e-h pair	electron-hole pair
GNF	Graphene Nanoflake
IR	Infrared
Laser	Light Amplification by Stimulated Emission of Radiation
LSP	Localized Surface Plasmons
LOQC	Linear Optics Quantum Computing
LSP	Localized Surface Plasmon Resonance
MIR	Mid Infrared
NIR	Near Infrared
NP	Nanoparticle
QD	Quantum Dot
QED	Quantum Electrodynamics
QW	Quantum Well
SP	Surface Plasmon
Spaser	Surface Plasmon Amplification by Stimulated Emission of Radiation
SPP	Surface Plasmon Polaritons
SPR	Surface Plasmon Resonance
TLS	Two Level System

# Bibliography

- [1] Matthew Rycenga, Claire M Cobley, Jie Zeng, Weiyang Li, Christine H Moran, Qiang Zhang, Dong Qin, and Younan Xia. Controlling the synthesis and assembly of silver nanostructures for plasmonic applications. *Chem. Rev.*, 111(6):3669–3712, 2011.
- [2] Prashant K. Jain, Kyeong Seok Lee, Ivan H. El-Sayed, and Mostafa A. El-Sayed. Calculated absorption and scattering properties of gold nanoparticles of different size, shape, and composition: applications in biological imaging and biomedicine. *J. Phys. Chem. B*, 110(14):7238–7248, 2006.
- [3] Benjamin J Wiley, Sang Hyuk Im, Zhi-Yuan Li, Joseph McLellan, Andrew Siekkinen, and Younan Xia. Maneuvering the surface plasmon resonance of silver nanostructures through shape-controlled synthesis. *J. Phys. Chem. B*, 110(32):15666–15675, 2006.
- [4] Xiaohua Huang, Ivan H El-Sayed, Wei Qian, and Mostafa A El-Sayed. Cancer cell imaging and photothermal therapy in the near-infrared region by using gold nanorods. *J. Am. Chem. Soc.*, 128(6):2115–2120, 2006.
- [5] Emilie Ringe, Jeffrey M McMahon, Kwonnam Sohn, Claire Cobley, Younan Xia, Jiaying Huang, George C Schatz, Laurence D Marks, and Richard P Van Duyne. Unraveling the effects of size, composition, and substrate on the localized surface plasmon resonance frequencies of gold and silver nanocubes:

- a systematic single-particle approach. *J. Phys. Chem. C*, 114(29):12511–12516, 2010.
- [6] Mark J Bloemer, MC Buncick, RJ Warmack, and TL Ferrell. Surface electromagnetic modes in prolate spheroids of gold, aluminum, and copper. *J. Opt. Soc. Am. B*, 5(12):2552–2559, 1988.
- [7] VI Klimov, AA Mikhailovsky, Su Xu, A Malko, JA Hollingsworth, CA Leatherdale, H-J Eisler, and MG Bawendi. Optical gain and stimulated emission in nanocrystal quantum dots. *Science*, 290(5490):314–317, 2000.
- [8] DJ Norris, A Sacra, CB Murray, and MG Bawendi. Measurement of the size dependent hole spectrum in cdse quantum dots. *Phys. Rev. Lett.*, 72(16):2612, 1994.
- [9] Xavier Michalet, Fabien F Pinaud, Laurent A Bentolila, James M Tsay, SJJL Doose, Jack J Li, Gobalakrishnan Sundaresan, Anna M Wu, Sanjiv S Gambhir, and Shimon Weiss. Quantum dots for live cells, in vivo imaging, and diagnostics. *Science*, 307(5709):538–544, 2005.
- [10] Wenjin Zhang, Guanjiao Chen, Jian Wang, Bang-Ce Ye, and Xinhua Zhong. Design and synthesis of highly luminescent near-infrared-emitting water-soluble cdte/cdse/zns core/shell/shell quantum dots. *Inorganic Chemistry*, 48(20):9723–9731, 2009.
- [11] AA Guzelian, U Banin, AV Kadavanich, X Peng, and AP Alivisatos. Colloidal chemical synthesis and characterization of inas nanocrystal quantum dots. *App. Phys. Lett.*, 69(10):1432–1434, 1996.
- [12] Juergen Fabian, Hiroyuki Nakazumi, and Masaru Matsuoka. Near-infrared absorbing dyes. *Chem. Rev.*, 92(6):1197–1226, 1992.

- [13] Fluorophores.org. Database of fluorescent dyes, properties, and applications. <http://www.fluorophores.org>. [Online; accessed 10-July-2015].
- [14] William F Krupke. Optical absorption and fluorescence intensities in several rare-earth-doped  $\text{Y}_2\text{O}_3$  and  $\text{LaF}_3$  single crystals. *Phys. Rev.*, 145(1):325, 1966.
- [15] Yu-Chun Li, Yen-Hwei Chang, Yu-Feng Lin, Yee-Shin Chang, and Yi-Jing Lin. Synthesis and luminescent properties of  $\text{Ln}^{3+}$  ( $\text{Eu}^{3+}$ ,  $\text{Sm}^{3+}$ ,  $\text{Dy}^{3+}$ )-doped lanthanum aluminum germanate  $\text{LaAlGe}_2\text{O}_7$  phosphors. *Journal of alloys and compounds*, 439(1):367–375, 2007.
- [16] Mark I Stockman. Spasers explained. *Nature Photonics*, 2(6):327–329, 2008.
- [17] Mark I. Stockman. Nanoplasmonics: Past, present, and glimpse into future. *Opt. Express*, 19(22):22029–22106, Oct 2011.
- [18] M. A. Noginov, G. Zhu, A. M. Belgrave, R. Bakker, V. M. Shalaev, E. E Narimanov, S. Stout, E. Herz, T. Suteewong, and U. Wiesner. Demonstration of a spaser-based nanolaser. *Nature*, 460(7259):1110–1112, 2009.
- [19] Mark L Brongersma and Vladimir M Shalaev. The case for plasmonics. *Science*, 328(5977):440–441, 2010.
- [20] Ekmel Ozbay. Plasmonics: Merging photonics and electronics at nanoscale dimensions. *Science*, 311(5758):189–193, 2006.
- [21] Mo Li, W. H. P. Pernice, C. Xiong, T. Baehr-Jones, M. Hochberg, and H. X. Tang. Harnessing optical forces in integrated photonic circuits. *Nature*, 456(7221):480–484, 2008.
- [22] R. Soref. The past, present, and future of silicon photonics. *IEEE J. Sel. Top. Quantum Electron.*, 12(6):1678–1687, nov.-dec. 2006.

- [23] A.V. Krishnamoorthy and K.W. Goossen. Optoelectronic-vlsi: photonics integrated with vlsi circuits. *IEEE J. Sel. Top. Quantum Electron.*, 4(6):899–912, nov/dec 1998.
- [24] Malin Premaratne and Govind P. Agrawal. *Light Propagation in Gain Media: Optical Amplifiers*. Cambridge University Press, 2011.
- [25] S.A. Maier. *Plasmonics: Fundamentals and Applications*. Springer, 2007.
- [26] Anatoly V Zayats and Igor I Smolyaninov. Near-field photonics: surface plasmon polaritons and localized surface plasmons. *J. Opt. A: Pure Appl. Opt.*, 5(4):S16, 2003.
- [27] William L. Barnes, Alain Dereux, and Thomas W. Ebbesen. Surface plasmon subwavelength optics. *Nature*, 424(6950):824–830, 2003.
- [28] David J. Bergman and Mark I. Stockman. Surface plasmon amplification by stimulated emission of radiation: Quantum generation of coherent surface plasmons in nanosystems. *Phys. Rev. Lett.*, 90:027402, Jan 2003.
- [29] AA Lisyansky, IA Nechepurenko, AV Dorofeenko, AP Vinogradov, and AA Pukhov. Channel spaser: Coherent excitation of one-dimensional plasmons from quantum dots located along a linear channel. *Phys. Rev. B*, 84(15):153409, 2011.
- [30] N.I. Zheludev, SL Prosvirnin, N. Papasimakis, and VA Fedotov. Lasing spaser. *Nat. Photonics*, 2(6):351–354, 2008.
- [31] Shu-Wei Chang, Chi-Yu Adrian Ni, and Shun-Lien Chuang. Theory for bowtie plasmonic nanolasers. *Opt. Express*, 16(14):10580–10595, Jul 2008.
- [32] Mark I Stockman. The spaser as a nanoscale quantum generator and ultrafast amplifier. *J. Opt.*, 12(2):024004, 2010.

- [33] Jacob B. Khurgin and Greg Sun. Injection pumped single mode surface plasmon generators: threshold, linewidth, and coherence. *Opt. Express*, 20(14):15309–15325, Jul 2012.
- [34] ES Andrianov, AA Pukhov, AV Dorofeenko, AP Vinogradov, and AA Lisyan-sky. Dipole response of spaser on an external optical wave. *Opt. Lett.*, 36(21):4302–4304, 2011.
- [35] ES Andrianov, AA Pukhov, AV Dorofeenko, AP Vinogradov, and AA Lisyan-sky. Forced synchronization of spaser by an external optical wave. *Opt. Express*, 19(25):24849–24857, 2011.
- [36] Igor E Protsenko, Alexander V Uskov, OA Zaimidoroga, VN Samoilov, and EP Oreilly. Dipole nanolaser. *Phys. Rev. A*, 71(6):063812, 2005.
- [37] A Ridolfo, O Di Stefano, N Fina, R Saija, and S Savasta. Quantum plas-monics with quantum dot-metal nanoparticle molecules: influence of the fano effect on photon statistics. *Phys. Rev. Lett.*, 105(26):263601, 2010.
- [38] AS Rosenthal and Talal Ghannam. Dipole nanolasers: A study of their quantum properties. *Phys. Rev. A*, 79(4):043824, 2009.
- [39] R. A. Flynn, C. S. Kim, I. Vurgaftman, M. Kim, J. R. Meyer, A. J. Mäkinen, K. Bussmann, L. Cheng, F. S. Choa, and J. P. Long. A room-temperature semiconductor spaser operating near 1.5  $\mu\text{m}$ . *Opt. Express*, 19(9):8954–8961, Apr 2011.
- [40] E Plum, VA Fedotov, P Kuo, DP Tsai, and NI Zheludev. Towards the lasing spaser: controlling metamaterial optical response with semiconductor quantum dots. *Optics Express*, 17(10):8548–8551, 2009.
- [41] J. Seidel, S. Grafström, and L. Eng. Stimulated emission of surface plasmons at the interface between a silver film and an optically pumped dye solution. *Phys. Rev. Lett.*, 94:177401, May 2005.

- [42] Mark I. Stockman. Nanoplasmonics: The physics behind the applications. *Phys. Today*, 64(2):39–44, 2011.
- [43] Amit Agrawal, Ceren Susut, Gery Stafford, Ugo Bertocci, Benjamin McMorran, Henri J Lezec, and A Alec Talin. An integrated electrochromic nanoplasmonic optical switch. *Nano Lett.*, 11(7):2774–2778, 2011.
- [44] Hua Lu, Xueming Liu, Yongkang Gong, Dong Mao, and Leiran Wang. Enhancement of transmission efficiency of nanoplasmonic wavelength demultiplexer based on channel drop filters and reflection nanocavities. *Opt. Express*, 19(14):12885–12890, 2011.
- [45] AV Krasavin and AV Zayats. Photonic signal processing on electronic scales: electro-optical field-effect nanoplasmonic modulator. *Phys. Rev. Lett.*, 109(5):053901, 2012.
- [46] P.W. Milonni and J.H. Eberly. *Laser Physics*. Wiley, 2010.
- [47] Albert Einstein. Strahlungs-emission und absorption nach der quantentheorie. *Deutsche Physikalische Gesellschaft*, 18:318–323, 1916.
- [48] James P Gordon, Herbert J Zeiger, and Charles H Townes. The maser new type of microwave amplifier, frequency standard, and spectrometer. *Phys. Rev.*, 99(4):1264, 1955.
- [49] R Gordon Gould. The laser, light amplification by stimulated emission of radiation. In *The Ann Arbor conference on optical pumping, the University of Michigan*, volume 15, page 128, 1959.
- [50] S.E. Lyshevski. *Nano- and Micro-Electromechanical Systems: Fundamentals of Nano- and Microengineering, Second Edition*. CRC Press, 2005.
- [51] JL Jewell, YH Lee, S Walker, A Scherer, JP Harbison, LT Florez, and SL McCall. Low-threshold electrically pumped vertical-cavity surface-emitting microlasers. *Electron. Lett.*, 25(17):1123–1124, 1989.

- [52] Kyungwon An, James J Childs, Ramachandra R Dasari, and Michael S Feld. Microlaser: A laser with one atom in an optical resonator. *Phys. Rev. Lett.*, 73(25):3375, 1994.
- [53] Chang-Ling Zou, Yun-Feng Xiao, Zheng-Fu Han, Chun-Hua Dong, Xiang-Dong Chen, Jin-Ming Cui, Guang-Can Guo, and Fang-Wen Sun. High-q nanoring surface plasmon microresonator. *J. Opt. Soc. Am. B*, 27(12):2495–2498, Dec 2010.
- [54] Jitao Li, Chunxiang Xu, Haiyan Nan, Mingming Jiang, Guangyu Gao, Yi Lin, Jun Dai, Gangyi Zhu, Zhenhua Ni, Shufeng Wang, et al. Graphene surface plasmon induced optical field confinement and lasing enhancement in zno whispering-gallery microcavity. *ACS Appl. Mater. Interfaces*, 6(13):10469–10475, 2014.
- [55] Dabing Li and Mark I Stockman. Electric spaser in the extreme quantum limit. *Phys. Rev. Lett.*, 110(10):106803, 2013.
- [56] Thamani Wijesinghe and Malin Premaratne. Dispersion relation for surface plasmon polaritons on a schottky junction. *Opt. Express*, 20(7):7151–7164, 2012.
- [57] D. Bimberg, N. Kirstaedter, N.N. Ledentsov, Zh.I. Alferov, P.S. Kop’ev, and V.M. Ustinov. Ingaas-gaas quantum-dot lasers. *IEEE J. Sel. Top. Quantum Electron.*, 3(2):196–205, apr 1997.
- [58] D. L. Huffaker, G. Park, Z. Zou, O. B. Shchekin, and D. G. Deppe. 1.3  $\mu\text{m}$  room-temperature gaas-based quantum-dot laser. *Appl. Phys. Lett.*, 73(18):2564–2566, 1998.
- [59] Anatolii N Oraevsky, M O Scully, and Vladimir L Velichansky. Quantum dot laser. *Quantum Electron.*, 28(3):203, 1998.

- [60] A. Markus, J. X. Chen, C. Paranthoën, A. Fiore, C. Platz, and O. Gauthier-Lafaye. Simultaneous two-state lasing in quantum-dot lasers. *Appl. Phys. Lett.*, 82(12):1818–1820, 2003.
- [61] M Sugawara, N Hatori, M Ishida, H Ebe, Y Arakawa, T Akiyama, K Otsubo, T Yamamoto, and Y Nakata. Recent progress in self-assembled quantum-dot optical devices for optical telecommunication: temperature-insensitive 10?gb?s -1 directly modulated lasers and 40?gb?s -1 signal-regenerative amplifiers. *J. Phys. D: Appl. Phys.*, 38(13):2126, 2005.
- [62] M. Grundmann, J. Christen, N. N. Ledentsov, J. Böhrer, D. Bimberg, S. S. Ruvimov, P. Werner, U. Richter, U. Gösele, J. Heydenreich, V. M. Ustinov, A. Yu. Egorov, A. E. Zhukov, P. S. Kop’ev, and Zh. I. Alferov. Ultranarrow luminescence lines from single quantum dots. *Phys. Rev. Lett.*, 74:4043–4046, May 1995.
- [63] S. Strauf, K. Hennessy, M. T. Rakher, Y.-S. Choi, A. Badolato, L. C. Andreani, E. L. Hu, P. M. Petroff, and D. Bouwmeester. Self-tuned quantum dot gain in photonic crystal lasers. *Phys. Rev. Lett.*, 96:127404, Mar 2006.
- [64] Jacob B. Khurgin and Greg Sun. How small can nano be in a nanolaser? *Nanophotonics*, 1(1):3–8, 2012.
- [65] E. S. Andrianov, A. A. Pukhov, A. V. Dorofeenko, A. P. Vinogradov, and A. A. Lisyansky. Rabi oscillations in spasers during nonradiative plasmon excitation. *Phys. Rev. B*, 85:035405, Jan 2012.
- [66] Andrey K Sarychev and Gennady Tartakovsky. Magnetic plasmonic metamaterials in actively pumped host medium and plasmonic nanolaser. *Phys. Rev. B*, 75(8):085436, 2007.
- [67] Martin Wegener, Juan Luis García-Pomar, Costas M Soukoulis, Nina Meinzer, Matthias Ruther, and Stefan Linden. Toy model for plasmonic

- metamaterial resonances coupled to two-level system gain. *Opt. Express*, 16(24):19785–19798, 2008.
- [68] Sebastian Wuestner, Andreas Pusch, Kosmas L Tsakmakidis, Joachim M Hamm, and Ortwin Hess. Overcoming losses with gain in a negative refractive index metamaterial. *Phys. Rev. Lett.*, 105(12):127401, 2010.
- [69] Anan Fang, Thomas Koschny, and Costas M Soukoulis. Lasing in metamaterial nanostructures. *J. Opt.*, 12(2):024013, 2010.
- [70] Chanaka Rupasinghe, Ivan D Rukhlenko, and Malin Premaratne. Design optimization of spasers considering the degeneracy of excited plasmon modes. *Opt. Express*, 21(13):15335–15349, 2013.
- [71] M.S. Dresselhaus, G. Dresselhaus, and P. Avouris. *Carbon Nanotubes: Synthesis, Structure, Properties, and Applications*. Topics in applied physics, v. 80. Springer-Verlag GmbH, 2001.
- [72] AN Grigorenko, Marco Polini, and KS Novoselov. Graphene plasmonics. *Nat. Photon.*, 6(11):749–758, 2012.
- [73] Frank HL Koppens, Darrick E Chang, and F Javier Garcia de Abajo. Graphene plasmonics: a platform for strong light–matter interactions. *Nano lett.*, 11(8):3370–3377, 2011.
- [74] Juan G Duque, Matteo Pasquali, Laurent Cognet, and Brahim Lounis. Environmental and synthesis-dependent luminescence properties of individual single-walled carbon nanotubes. *ACS Nano*, 3(8):2153–2156, 2009.
- [75] Phaedon Avouris, Marcus Freitag, and Vasili Perebeinos. Carbon-nanotube photonics and optoelectronics. *Nature photon.*, 2(6):341–350, 2008.
- [76] Etienne Gaufres, Nicolas Izard, Adrien Noury, Xavier Le Roux, Gilles Rasi-gade, Alexandre Beck, and Laurent Vivien. Light emission in silicon from carbon nanotubes. *ACS Nano*, 6(5):3813–3819, 2012.

- [77] F. Leonard. *Physics of Carbon Nanotube Devices*. Micro and Nano Technologies. Elsevier Science, 2008.
- [78] Yin Zhang, Tapas R Nayak, Hao Hong, and Weibo Cai. Graphene: a versatile nanoplatform for biomedical applications. *Nanoscale*, 4(13):3833–3842, 2012.
- [79] Kai Yang, Shuai Zhang, Guoxin Zhang, Xiaoming Sun, Shuit-Tong Lee, and Zhuang Liu. Graphene in mice: ultrahigh in vivo tumor uptake and efficient photothermal therapy. *Nano lett.*, 10(9):3318–3323, 2010.
- [80] Pavitra Chakravarty, Radu Marches, Neil S Zimmerman, Austin D-E Swafford, Pooja Bajaj, Inga H Musselman, Paul Pantano, Rockford K Draper, and Ellen S Vitetta. Thermal ablation of tumor cells with antibody-functionalized single-walled carbon nanotubes. *Proc. Natl. Acad. Sci.*, 105(25):8697–8702, 2008.
- [81] FA Berazin. *The method of second quantization*, volume 24. Elsevier, 2012.
- [82] L.D. Landau, E. M. Lifshitz, and L. P. Pitaevskii. *Course of Theoretical Physics Vol 8: Electrodynamics of Continuous Media*. Elsevier, 2004.
- [83] Nahid Talebi, Wilfried Sigle, Ralf Vogelgesang, Christoph T Koch, Cristina Fernández-López, Luis M Liz-Marzan, Burcu Ogut, Melanie Rohm, and Peter A van Aken. Breaking the mode degeneracy of surface plasmon resonances in a triangular system. *Langmuir*, 28(24):8867–8873, 2012.
- [84] C.F. Bohren and D.R. Huffman. *Absorption and scattering of light by small particles*. Wiley, 1983.
- [85] P.W. Milonni and J.H. Eberly. *Laser Physics*. Wiley, 2010.
- [86] J.M. Jauch. *Foundations of quantum mechanics*. Addison-Wesley series in advanced physics. Addison-Wesley Pub. Co., 1968.

- [87] AV Fedorov, AV Baranov, and Y. Masumoto. Coherent control of optical-phonon-assisted resonance secondary emission in semiconductor quantum dots. *Opt. Spectrosc.*, 93(1):52–60, 2002.
- [88] I.D. Rukhlenko, A.V. Fedorov, A.S. Baymuratov, and M. Premaratne. Theory of quasi-elastic secondary emission from a quantum dot in the regime of vibrational resonance. *Opt. Express*, 19(16):15459–15482, 2011.
- [89] A.V. Fedorov and I.D. Rukhlenko. Study of electronic dynamics of quantum dots using resonant photoluminescence technique. *Optics and Spectroscopy*, 100:716–723, 2006.
- [90] A. V. Fedorov, A. V. Baranov, I. D. Rukhlenko, T. S. Perova, and K. Berwick. Quantum dot energy relaxation mediated by plasmon emission in doped covalent semiconductor heterostructures. *Phys. Rev. B*, 76:045332, Jul 2007.
- [91] A.I. Ansel'm. *Introduction to Semiconductor Theory*. Mir, 1981.
- [92] D. Bimberg, R. Blachnik, P.J. Dean, T. Grave, G. Harbeke, K. Hübner, U. Kaufmann, W. Kress, O. Madelung, et al. *Physics of Group IV Elements and III-V Compounds / Physik der Elemente der IV. Gruppe und der III-V Verbindungen*. Number v. 17. Springer, 1981.
- [93] U. Fano. Description of states in quantum mechanics by density matrix and operator techniques. *Rev. Mod. Phys.*, 29:74–93, Jan 1957.
- [94] K. Blum. *Density Matrix Theory and Applications*. Springer, 2010.
- [95] D. Sarid and W. Challener. *Modern Introduction to Surface Plasmons: Theory, Mathematica Modeling, and Applications*. Cambridge University Press, 2010.
- [96] K. Lance Kelly, Eduardo Coronado, Lin Lin Zhao, and George C. Schatz. The optical properties of metal nanoparticles: the influence of size, shape, and dielectric environment. *J. Phys. Chem. B*, 107(3):668–677, 2003.

- [97] Arthur L. Aden and Milton Kerker. Scattering of electromagnetic waves from two concentric spheres. *J. Appl. Phys.*, 22(10):1242–1246, oct 1951.
- [98] E.H. Sondheimer. The mean free path of electrons in metals. *Adv. Phys.*, 1(1):1–42, 1952.
- [99] B Hecht, H Bielefeldt, L Novotny, Y Inouye, and DW Pohl. Local excitation, scattering, and interference of surface plasmons. *Physical review letters*, 77(9):1889, 1996.
- [100] M. Ventra, S. Evoy, and J.R. Heflin. *Introduction to Nanoscale Science and Technology*. Nanostructure Science and Technology. Springer, 2004.
- [101] BV Enustun and John Turkevich. Coagulation of colloidal gold. *J. Am. Chem. Soc.*, 85(21):3317–3328, 1963.
- [102] P Mulvaney, LM Liz-Marzan, M Giersig, and T Ung. Silica encapsulation of quantum dots and metal clusters. *J. Mat. Chem.*, 10(6):1259–1270, 2000.
- [103] Luis M Liz-Marzán, Michael Giersig, and Paul Mulvaney. Synthesis of nano-sized gold-silica core-shell particles. *Langmuir*, 12(18):4329–4335, 1996.
- [104] Marek Grzelczak, Jorge Pérez-Juste, Paul Mulvaney, and Luis M Liz-Marzán. Shape control in gold nanoparticle synthesis. *Chem. Soc. Rev.*, 37(9):1783–1791, 2008.
- [105] JitKang Lim, Alexander Eggeman, Frederick Lanni, Robert D. Tilton, and Sara A. Majetich. Synthesis and single-particle optical detection of low-polydispersity plasmonic-superparamagnetic nanoparticles. *Adv. Mater.*, 20(9):1721–1726, 2008.
- [106] R.D. Averitt, S.L. Westcott, and N.J. Halas. Linear optical properties of gold nanoshells. *JOSA B*, 16(10):1824–1832, 1999.

- [107] P. B. Johnson and R. W. Christy. Optical constants of the noble metals. *Phys. Rev. B*, 6:4370–4379, Dec 1972.
- [108] K. Kolwas, A. Derkachova, and M. Shopa. Size characteristics of surface plasmons and their manifestation in scattering properties of metal particles. *J. Quant. Spectrosc. Radiat. Transfer*, 110(14):1490–1501, 2009.
- [109] Liping Liu, Qing Peng, and Yadong Li. An effective oxidation route to blue emission cdse quantum dots. *Inorg. Chem.*, 47(8):3182–3187, 2008.
- [110] W.C. Kwak, T.G. Kim, W.S. Chae, and Y.M. Sung. Tuning the energy bandgap of cdse nanocrystals via mg doping. *Nanotechnology*, 18(20):205702, 2007.
- [111] Y Arakawa and Hiroyuki Sakaki. Multidimensional quantum well laser and temperature dependence of its threshold current. *Appl. Phys. Lett.*, 40(11):939–941, 1982.
- [112] R. Saito, Gene Dresselhaus, and M.S. Dresselhaus. *Physical Properties of Carbon Nanotube*. Imperial College Press, 1998.
- [113] Mildred S Dresselhaus, Gene Dresselhaus, Riichiro Saito, and Ado Jorio. Exciton photophysics of carbon nanotubes. *Annu. Rev. Phys. Chem.*, 58:719–747, 2007.
- [114] Vadym Apalkov and Mark I Stockman. Graphene spaser. *arXiv preprint arXiv:1303.0220*, 2013.
- [115] EH Hwang and S Das Sarma. Dielectric function, screening, and plasmons in two-dimensional graphene. *Phys. Rev. B*, 75(20):205418, 2007.
- [116] Ashkan Vakil and Nader Engheta. Transformation optics using graphene. *Science*, 332(6035):1291–1294, 2011.

- [117] Jianing Chen, Michela Badioli, Pablo Alonso Gonzalez, Sukosin Thongrattanasiri, Florian Huth, Johann Osmond, Marko Spasenovic, Alba Centeno, Amaia Pesquera, and Philippe Godignon. Optical nano-imaging of gate-tunable graphene plasmons. *Nature*, 487(7405):77–81, 2012.
- [118] Long Ju, Baisong Geng, Jason Horng, Caglar Girit, Michael Martin, Zhao Hao, Hans A Bechtel, Xiaogan Liang, Alex Zettl, and Y Ron Shen. Graphene plasmonics for tunable terahertz metamaterials. *Nature Nanotechnology*, 6(10):630–634, 2011.
- [119] Zhe Fei, Gregory O Andreev, Wenzhong Bao, Lingfeng M Zhang, Alexander S. McLeod, Chen Wang, Margaret K Stewart, Zeng Zhao, Gerardo Dominguez, and Mark Thiemens. Infrared nanoscopy of dirac plasmons at the graphene–sio<sub>2</sub> interface. *Nano Lett.*, 11(11):4701–4705, 2011.
- [120] Weilu Gao, Jie Shu, Ciyuan Qiu, and Qianfan Xu. Excitation of plasmonic waves in graphene by guided-mode resonances. *ACS Nano*, 6(9):7806–7813, 2012.
- [121] LA Falkovsky. Optical properties of graphene. In *J. Phys.: Conf. Ser.*, volume 129, page 012004. IOP Publishing, 2008.
- [122] Qiaoliang Bao and Kian Ping Loh. Graphene photonics, plasmonics, and broadband optoelectronic devices. *ACS Nano*, 6(5):3677–3694, 2012.
- [123] Keun Soo Kim, Yue Zhao, Houk Jang, Sang Yoon Lee, Jong Min Kim, Kwang S Kim, Jong-Hyun Ahn, Philip Kim, Jae-Young Choi, and Byung Hee Hong. Large-scale pattern growth of graphene films for stretchable transparent electrodes. *Nature*, 457(7230):706–710, 2009.
- [124] Sasha Stankovich, Dmitriy A Dikin, Richard D Piner, Kevin A Kohlhaas, Alfred Kleinhammes, Yuanyuan Jia, Yue Wu, SonBinh T Nguyen, and Rod-

- ney S Ruoff. Synthesis of graphene-based nanosheets *via* chemical reduction of exfoliated graphite oxide. *Carbon*, 45(7):1558–1565, 2007.
- [125] M Born and E Wolf. *Principles of Optics*. Cambridge University Press, 7 edition, 1999.
- [126] Gilbert Strang and George J Fix. *An Analysis of the Finite Element Method*, volume 212. Prentice-Hall Englewood Cliffs, 1973.
- [127] Vasili Perebeinos, J Tersoff, and Phaedon Avouris. Radiative lifetime of excitons in carbon nanotubes. *Nano Lett.*, 5(12):2495–2499, 2005.
- [128] Seung-Hoon Jhi, Steven G Louie, and Marvin L Cohen. Electronic properties of oxidized carbon nanotubes. *Phys. Rev. Lett.*, 85(8):1710, 2000.
- [129] Jian Chen, Mark A Hamon, Hui Hu, Yongsheng Chen, Apparao M Rao, Peter C Eklund, and Robert C Haddon. Solution properties of single-walled carbon nanotubes. *Science*, 282(5386):95–98, 1998.
- [130] Fabien Vialla, Cyrielle Roquelet, Benjamin Langlois, Géraud Delpont, Silvia Morim Santos, Emmanuelle Deleporte, Philippe Roussignol, Claude Delalande, Christophe Voisin, and Jean-Sébastien Lauret. Chirality dependence of the absorption cross section of carbon nanotubes. *Phys. Rev. Lett.*, 111(13):137402, 2013.
- [131] Yong Zhou and Kian Ping Loh. Making patterns on graphene. *Adv. Mater.*, 22(32):3615–3620, 2010.
- [132] Qiang Zhang, Jia-Qi Huang, Wei-Zhong Qian, Ying-Ying Zhang, and Fei Wei. The road for nanomaterials industry: A review of carbon nanotube production, post-treatment, and bulk applications for composites and energy storage. *Small*, 9(8):1237–1265, 2013.

- [133] Debabrata Sikdar, Ivan D Rukhlenko, Wenlong Cheng, and Malin Premaratne. Tunable broadband optical responses of substrate-supported metal/dielectric/metal nanospheres. *Plasmonics*, pages <http://dx.doi.org/10.1007/s11468-014-9681-8>, 2014.
- [134] Xiangfeng Duan, Yu Huang, Ritesh Agarwal, and Charles M Lieber. Single-nanowire electrically driven lasers. *Nature*, 421(6920):241–245, 2003.
- [135] Thaddeus D Ladd, Fedor Jelezko, Raymond Laflamme, Yasunobu Nakamura, Christopher Monroe, and Jeremy L OBrien. Quantum computers. *Nature*, 464(7285):45–53, 2010.
- [136] John Preskill. Reliable quantum computers. In *Proceedings of the Royal Society of London A: Mathematical, Physical and Engineering Sciences*, volume 454, pages 385–410. The Royal Society, 1998.
- [137] Philip Walther, Kevin J Resch, Terry Rudolph, Emmanuel Schenck, Harald Weinfurter, Vlatko Vedral, Markus Aspelmeyer, and Anton Zeilinger. Experimental one-way quantum computing. *Nature*, 434(7030):169–176, 2005.
- [138] Emanuel Knill, Raymond Laflamme, and Gerald J Milburn. A scheme for efficient quantum computation with linear optics. *Nature*, 409(6816):46–52, 2001.
- [139] T Pellizzari, SA Gardiner, JI Cirac, and P Zoller. Decoherence, continuous observation, and quantum computing: A cavity qed model. *Phys. Rev. Lett.*, 75(21):3788, 1995.
- [140] Alexandre Blais, Ren-Shou Huang, Andreas Wallraff, SM Girvin, and R Jun Schoelkopf. Cavity quantum electrodynamics for superconducting electrical circuits: An architecture for quantum computation. *Phys. Rev. A*, 69(6):062320, 2004.

- [141] D Patrick O'Neal, Leon R Hirsch, Naomi J Halas, J Donald Payne, and Jennifer L West. Photo-thermal tumor ablation in mice using near infrared-absorbing nanoparticles. *Cancer Lett.*, 209(2):171–176, 2004.
- [142] Harold J Burstein. Side effects of chemotherapy. *J. Clin. Oncol.*, 18(3):693–693, 2000.
- [143] Babu Zachariah, Lodovico Balducci, GV Venkattaramanabalaji, Linda Casey, Harvey M Greenberg, and Juan A DelRegato. Radiotherapy for cancer patients aged 80 and older: a study of effectiveness and side effects. *Int. J. Radiat. Oncol.*, 39(5):1125–1129, 1997.
- [144] Wei R Chen, Robert L Adams, Raoul Carubelli, and Robert E Nordquist. Laser-photosensitizer assisted immunotherapy: a novel modality for cancer treatment. *Cancer Lett.*, 115(1):25–30, 1997.
- [145] G Scott Gazelle, S Nahum Goldberg, Luigi Solbiati, and Tito Livraghi. Tumor ablation with radio-frequency energy. *Radiology*, 217(3):633–646, 2000.
- [146] Joshua T Robinson, Scott M Tabakman, Yongye Liang, Hailiang Wang, Hernan Sanchez Casalongue, Daniel Vinh, and Hongjie Dai. Ultrasmall reduced graphene oxide with high near-infrared absorbance for photothermal therapy. *Journal of the American Chemical Society*, 133(17):6825–6831, 2011.
- [147] Christopher Loo, Amanda Lowery, Naomi Halas, Jennifer West, and Rebekah Drezek. Immunotargeted nanoshells for integrated cancer imaging and therapy. *Nano letters*, 5(4):709–711, 2005.
- [148] Kai Yang, Jianmei Wan, Shuai Zhang, Bo Tian, Youjiu Zhang, and Zhuang Liu. The influence of surface chemistry and size of nanoscale graphene oxide on photothermal therapy of cancer using ultra-low laser power. *Biomaterials*, 33(7):2206–2214, 2012.

- [149] Chanaka Rupasinghe, Ivan D Rukhlenko, and Malin Premaratne. Spaser made of graphene and carbon nanotubes. *ACS Nano*, 8(3):2431–2438, 2014.
- [150] M Pavel, G Gradinariu, and A Stancu. Study of the optimum dose of ferromagnetic nanoparticles suitable for cancer therapy using mfh. *Magnetics, IEEE Transactions on*, 44(11):3205–3208, 2008.
- [151] Geoffrey von Maltzahn, Ji-Ho Park, Amit Agrawal, Nanda Kishor Bandaru, Sarit K Das, Michael J Sailor, and Sangeeta N Bhatia. Computationally guided photothermal tumor therapy using long-circulating gold nanorod antennas. *Cancer research*, 69(9):3892–3900, 2009.
- [152] Pornthip Keangin, Phadungsak Rattanadecho, and Teerapot Wessapan. An analysis of heat transfer in liver tissue during microwave ablation using single and double slot antenna. *Int. Commun. Heat. Massr.*, 38(6):757–766, 2011.
- [153] Lidia S Szczepaniak, Pamela Nurenberg, David Leonard, Jeffrey D Browning, Jason S Reingold, Scott Grundy, Helen H Hobbs, and Robert L Dobbins. Magnetic resonance spectroscopy to measure hepatic triglyceride content: prevalence of hepatic steatosis in the general population. *Am. J. Physiol. Endocrinol. Metab.*, 288(2):E462–E468, 2005.
- [154] Anita Andreano and Christopher L Brace. A comparison of direct heating during radiofrequency and microwave ablation in ex vivo liver. *J. Vasc. Interv. Radiol.*, 36(2):505–511, 2013.
- [155] Zoran D Popovic and E Roland Menzel. Electric field-induced fluorescence quenching in organic photoconductors. *The Journal of Chemical Physics*, 71(12):5090–5096, 1979.
- [156] E Dulkeith, AC Morteani, T Niedereichholz, TA Klar, J Feldmann, SA Levi, FCJM Van Veggel, DN Reinhoudt, M Möller, and DI Gittins. Fluorescence

quenching of dye molecules near gold nanoparticles: radiative and nonradiative effects. *Phys. Rev. Lett.*, 89(20):203002, 2002.

[157] H.C. van de Hulst. *Light Scattering by Small Particles*. Dover Publications, 1981.

# Appendix: Numerical Methods

## A.1. Deriving SP Modes

### A.1.1 Spherical geometry

As the first step towards obtaining the electric field and the SP mode energies numerically the Helmholtz equation [84, 125]:

$$\nabla^2 \mathbf{E} + k^2 \mathbf{E} = 0 \quad (\text{A.1})$$

where  $k = \omega\sqrt{\epsilon}/c$  is analytically solved.

For spherical symmetry, this can be solved using Debye potentials  $\varphi = u, v$  which satisfies the equation,

$$\nabla^2 \varphi + k^2 \varphi = 0 \quad (\text{A.2})$$

$u$  and  $v$  can be derived as,

$$u_{l_p m_p} = \cos \phi P_{l_p}^{m_p}(\cos \theta) z_{l_p}(kr)$$

$$v_{l_p m_p} = \sin \phi P_{l_p}^{m_p}(\cos \theta) z_{l_p}(kr)$$

where,  $P_{l_p}^{m_p}$  are associated Legendre polynomials and  $z_{l_p}(kr)$  is the radial dependence of the electric field which equals to spherical Bessel functions,  $j_{l_p}(kr), y_{l_p}(kr)$  and  $h_{l_p}(kr)$  in different zones.

It can be shown that, the vectors  $\mathbf{M}_{l_p m_p}$  and  $\mathbf{N}_{l_p m_p}$ :

$$\mathbf{M}_{l_p m_p} = \nabla \times (v_{l_p} \mathbf{r}) \quad \text{and} \quad \mathbf{N}_{l_p m_p} = (1/k) \nabla \times \nabla \times (u_{l_p} \mathbf{r}) \quad (\text{A.3})$$

satisfy Eq.(A.1) when  $u_{l_p m_p}$  and  $v_{l_p m_p}$  satisfy Eq.(A.2) [84, 157].

However the localized surface plasmon modes of the spherical shell can be considered as only Transverse Magnetic (TM) where the electric field is radial. Hence we do not consider the TE modes and only the  $\mathbf{N}_{l_p m_p}$  component for the electric field is taken into the account. In the TM mode, respective magnetic field is in the form of  $\mathbf{M}_{l_p m_p}$ .

Here we have the notation  $\mathbf{N}_{l_p m_p} = \mathbf{N}_{l_p m_p}^{(1)}, \mathbf{N}_{l_p m_p}^{(2)}, \mathbf{N}_{l_p m_p}^{(3)}$  when the radial dependence in  $u_{l_p m_p}, z_{l_p}(kr) = j_{l_p}(kr), y_{l_p}(kr), h_{l_p}(kr)$  respectively.

Therefore, the solution for the electric field has the form,

$$\mathbf{E}(\mathbf{r}, t) = \sum_{l_p=1}^{\infty} \sum_{m_p=-l_p}^{l_p} \mathbf{E}_{l_p m_p}(\mathbf{r}) e^{j\omega t}$$

where  $\mathbf{E}_{l_p m_p}$  is proportional to  $\mathbf{N}_{l_p m_p}$ . Hence, field in the metal core (region 1), dielectric shell (region 2) and outer space (region 3),  $\mathbf{E}_{l_p m_p(1)}, \mathbf{E}_{l_p m_p(2)}$  and  $\mathbf{E}_{l_p m_p(3)}$  can be given as,

$$\mathbf{E}_{l_p m_p(1)} = d_{l_p m_p} \mathbf{N}_{l_p m_p}^{(1)} \quad (\text{A.4})$$

$$\mathbf{E}_{l_p m_p(2)} = g_{l_p m_p} \mathbf{N}_{l_p m_p}^{(1)} + w_{l_p} \mathbf{N}_{l_p m_p}^{(2)} \quad (\text{A.5})$$

$$\mathbf{E}_{l_p m_p(3)} = a_{l_p m_p} \mathbf{N}_{l_p m_p}^{(3)} \quad (\text{A.6})$$

$a_{l_p}, d_{l_p}, g_{l_p}, w_{l_p}$  are coefficients derived from the boundary conditions,

$$\begin{pmatrix} 0 & q_1 & q_2 & q_3 \\ 0 & s_1 & s_2 & s_3 \\ k_1 & 0 & k_2 & k_3 \\ m_1 & 0 & m_2 & m_3 \end{pmatrix} \begin{pmatrix} a_{l_p} \\ d_{l_p} \\ g_{l_p} \\ w_{l_p} \end{pmatrix} = \begin{pmatrix} 0 \\ 0 \\ 0 \\ 0 \end{pmatrix}$$

$$A\mathbf{x} = 0 \quad (\text{A.7})$$

Here,

$$q_1 = \sqrt{\epsilon_2} \psi'_{l_p}(k_m R_1), q_2 = -\sqrt{\epsilon_1} \psi'_{l_p}(k_d R_1), q_3 = \sqrt{\epsilon_1} \chi'_{l_p}(k_d R_1),$$

$$s_1 = -\psi_{l_p}(k_m R_1), s_2 = \psi_{l_p}(k_d R_1), s_3 = -\chi_{l_p}(k_d R_1),$$

$$k_1 = \sqrt{\epsilon_2} \xi'_{l_p}(k_0 R_2), k_2 = -\psi'_{l_p}(k_d R_2), k_3 = \chi'_{l_p}(k_d R_2),$$

$$m_1 = \xi_{l_p}(k_0 R_2), m_2 = -\psi_{l_p}(k_d R_2), m_3 = \chi_{l_p}(k_d R_2)$$

where we use the notation of Reccati-Bessel functions  $\psi_{l_p}(x) = x j_{l_p}(x)$ ,  $\xi_{l_p}(x) = x h_{l_p}^{(1)}(x)$  and  $\chi_{l_p}(x) = -x y_{l_p}(x)$  and  $k_m, k_d$  and  $k_0$  are wavenumbers in metal, dielectric and free space respectively.

To have a non-trivial solution for Eq. (A.7), the condition is

$$|A| = 0. \quad (\text{A.8})$$

The expanded determinant becomes,

$$\begin{aligned} m_1 [s_1(k_3q_2 - k_2q_3) - q_1(k_3s_2 - k_2s_3)] \\ = k_1 [s_1(m_3q_2 - m_2q_3) - q_1(m_3s_2 - m_2s_3)]. \end{aligned} \quad (\text{8.1})$$

This is the condition for the  $l_p$ th mode surface plasmon resonance. This relation is solved numerically in order to find the SP energies. This is done using MATLAB software by finding the roots of

$$\begin{aligned} F(\omega_{l_p}) = & m_1 [s_1(k_3q_2 - k_2q_3) - q_1(k_3s_2 - k_2s_3)] \\ & - k_1 [s_1(m_3q_2 - m_2q_3) - q_1(m_3s_2 - m_2s_3)] = 0 \end{aligned}$$

when  $R_1, R_2$  are given.

### A.1.2 GNF square geometry

GNF is assumed to have a finite thickness of  $t = 0.5$  nm for finite element analysis, which is standard approach to numerical modeling of graphene.[73, 116, 120]. Then the three dimensional conductivity of the GNF (Graphene nanoflake) is given by,[120]

$$\sigma_{3D}(\omega) = \frac{e^2 E_F}{\pi \hbar^2} \frac{i 2 k_B T}{t(\omega + i\tau^{-1})} \ln \left[ 2 \cosh \left( \frac{E_F}{2 k_B T} \right) \right]$$

The SP mode energies are found by eigenfrequency analysis of the Helmholtz equation using the COMSOL Multiphysics software.

## A.2. SP Quantization

The SPs are quantized according to:

$$\int_V \frac{1}{2} \frac{\partial}{\partial \omega} (\omega \epsilon(\omega)) |\mathbf{E}_{lm}(\mathbf{r})|^2 d\mathbf{r} = \hbar \omega_l, \quad (\text{A.9})$$

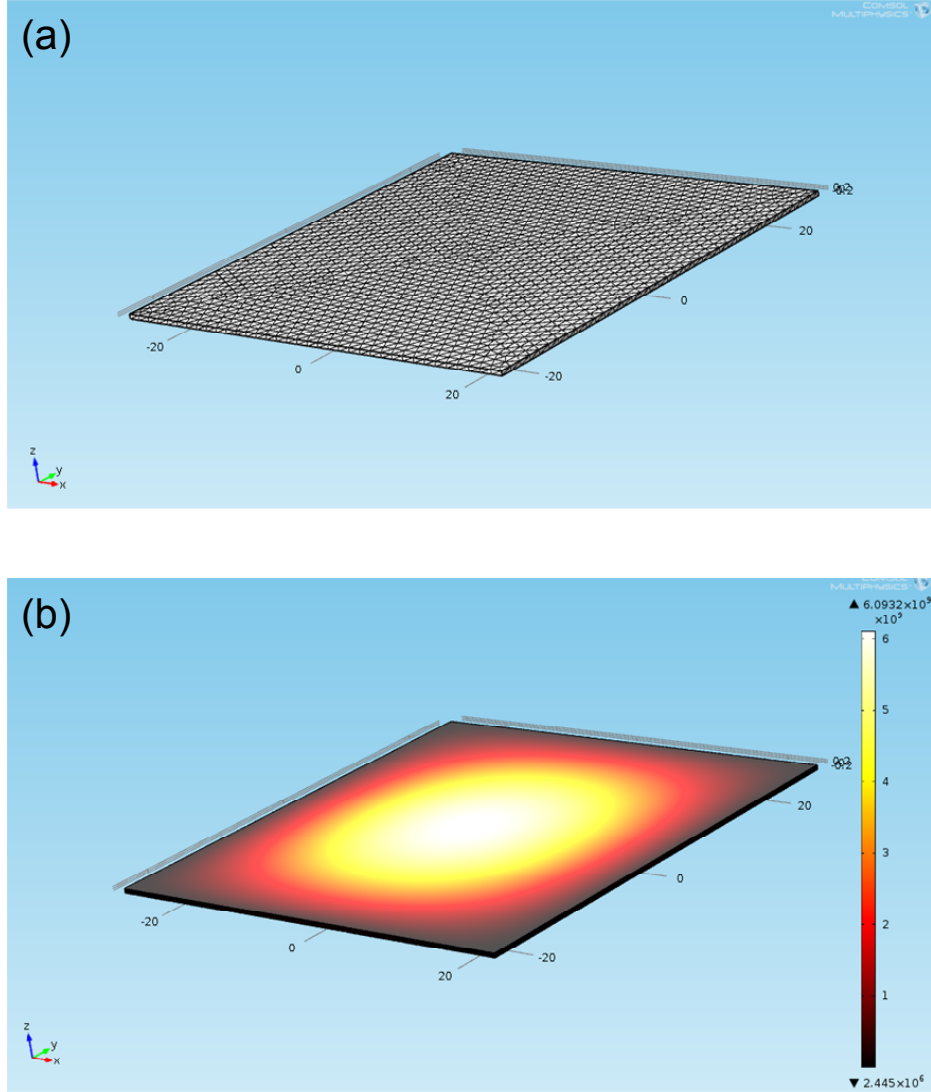


**Figure A.1:** (a) The mesh degenerated for the finite element analysis of a 50 nm wide GNF and (b) the generated electric field plot

where  $\mathbf{E}_{lm}(\mathbf{r})$  is the field generated by one SP. In both the cases of spherical and square geometries, the solution of the Helmholtz equation gives this in the form:

$$\mathbf{E}_{lm}(\mathbf{r}) = A_{lm} \mathbf{N}_{lm}(\mathbf{r})$$

where  $\mathbf{N}_{lm}(\mathbf{r})$  is a known function and  $A_{lm}$  is a normalization constant found by

$$A_{lm} = \frac{\hbar\omega_l}{\int_V \frac{1}{2} \frac{\partial}{\partial \omega} (\omega \varepsilon(\omega)) |\mathbf{E}_{lm}(\mathbf{r})|^2 d\mathbf{r}}, \quad (\text{A.10})$$

### A.3. Interaction Matrix Elements

According to Eqs.(2.13) and (2.11), the interaction matrix elements are given by,

$$V_{f,i}^{l,m} = \frac{\sqrt{2}P}{E_g} \int_V \psi_f^*(\mathbf{r}) E_{lm}(\mathbf{r}) \psi_i(\mathbf{r}) \, d\mathbf{r}. \quad (\text{A.11})$$

This integral is numerically calculated using MATLAB software for all the cases.

### A.4. SP Generation Rate

According to Eq. (2.16), the SP generation rate of a spaser can be given by,

$$\mathcal{R}_l = \frac{\xi_{23}\omega_l^2}{2\varepsilon_2\hbar\gamma_{13}\gamma_{22}\gamma_{33}\gamma_p} \frac{\gamma_{2p}}{\gamma_{2p}^2 + \Delta_{2p}^2} |V_{2e,0e}|^2 \sum_{j=4}^n |V_{1e,0e}^{l,j-3}|^2. \quad (\text{A.12})$$

Since the interaction matrix elements are evaluated from Eq. (A.11), this quantity is a direct calculation with the relevant decay constants assumed in different sections.

### A.5. Calculation of temperature rise of cancer cells

The resultant electric field build up on GNF due to total SP generation is substituted as a heat source:

$$Q_{SP} = \frac{1}{2} \sigma_{3D}(\omega) |\mathbf{E}_{lm}(\mathbf{r})|^2$$

for tissue in COMSOL bioheat transfer module to numerically solve the Pennes bioheat equation:

$$\rho_p C_p \frac{\partial T}{\partial t} + \nabla \cdot (-k_p \nabla T) = \rho_b C_b \omega_b (T_b - T) + Q_{met} + Q_{SP}.$$

In this case also graphene is assumed to have a finite thickness of 0.5 nm within the finite element analysis.